

BEAM DYNAMICS IN AN ULTRALOW ENERGY  
STORAGE RINGS (REVIEW OF EXISTING FACILITIES  
AND FEASIBILITY STUDIES  
FOR FUTURE EXPERIMENTS)

*A. I. Papash*<sup>1,2,3,\*</sup>, *A. V. Smirnov*<sup>1,2</sup>, *C. P. Welsch*<sup>4,5</sup>

<sup>1</sup> Joint Institute for Nuclear Research, Dubna

<sup>2</sup> Max Planck Institute for Nuclear Physics, Heidelberg, Germany

<sup>3</sup> Karlsruhe Institute of Technology, Karlsruhe, Germany

<sup>4</sup> University of Liverpool, Liverpool, UK

<sup>5</sup> The Cockcroft Institute for Accelerator Science and Technology, Daresbury, UK

INTRODUCTION	696
NONLINEAR EFFECTS IN ELECTROSTATIC STORAGE RINGS	697
Equations of Motion in Electrostatic Deflectors	699
Acceptance and Betatron Tune Shift in the ELISA Ring	702
ION KINETICS AND LONG-TERM BEAM DYNAMICS	706
Kinetic Equations	707
Multiple Scattering of Ions	709
Particle Loss Probability	713
Intrabeam Scattering	714
BENCHMARKING OF ELISA EXPERIMENTS	717
Ion Losses on Ring Aperture	718
Equilibrium Beam Profile	719
Momentum Spread Growth	720
OPERATION WITH INTERNAL TARGET	723
Layout of Recycler Ring	724
Growth of Beam Emittance in the Presence of the Target	725
Energy Losses due to Interaction of Ions with Gas Jet Atoms	729
Rate of Ionization Events in the Recycler Ring	732

---

\*E-mail: alexander.papash@kit.edu

SIMULATIONS OF BEAM SHRINKING IN THE TSR	
EXPERIMENT WITH SLOW IONS	734
Application of Photocathode Gun for the Electron	
Cooling of Low Energy Ions	735
The Ion Kinetics with Electron Cooling	736
Collapse of Beam Emittance at Low Beam Intensities	738
COMPENSATION OF IBS AND INTERNAL TARGET EFFECTS	
BY ELECTRON COOLING IN THE USR RING	744
The USR Lattice	744
Electron Cooling of 300 keV Antiprotons	747
Merit of the Photocathode Gun for the USR Electron	
Cooling System	749
Optimization of Lattice Parameters in the Cooler Section	753
Requirements to the Target Section of the Ring	755
Ionization Events and Adiabatic Dump of Equilibrium	
Parameters	760
SUMMARY AND OUTLOOK	763
REFERENCES	764

# BEAM DYNAMICS IN AN ULTRALOW ENERGY STORAGE RINGS (REVIEW OF EXISTING FACILITIES AND FEASIBILITY STUDIES FOR FUTURE EXPERIMENTS)

*A. I. Papash*<sup>1,2,3,\*</sup>, *A. V. Smirnov*<sup>1,2</sup>, *C. P. Welsch*<sup>4,5</sup>

<sup>1</sup> Joint Institute for Nuclear Research, Dubna

<sup>2</sup> Max Planck Institute for Nuclear Physics, Heidelberg, Germany

<sup>3</sup> Karlsruhe Institute of Technology, Karlsruhe, Germany

<sup>4</sup> University of Liverpool, Liverpool, UK

<sup>5</sup> The Cockcroft Institute for Accelerator Science and Technology, Daresbury, UK

Storage rings operating at ultralow energies and, in particular, electrostatic storage rings have proven to be invaluable tools for atomic and molecular physics. Due to the mass independence of the electrostatic rigidity, these machines are able to store a wide range of different particles, from light ions to heavy singly charged biomolecules. However, earlier measurements showed strong limitations on beam intensity, fast decay of ion current, reduced lifetime, etc. The nature of these effects was not fully understood. Also a large variety of experiments in future generation ultralow energy storage and decelerator facilities including in-ring collision studies with a reaction microscope require a comprehensive investigation of the physical processes involved into the operation of such rings. In this paper, we present review of nonlinear and long-term beam-dynamics studies on example of the ELISA, AD Recycler, TSR and USR rings using the computer codes BETACOOOL, OPERA-3D and MAD-X. The results from simulations were benchmarked against experimental data of beam losses in the ELISA storage ring. We showed that decay of beam intensity in ultralow energy rings is mainly caused by ion losses on ring aperture due to multiple scattering on residual gas. Beam is lost on ring aperture due to small ring acceptance. Rate of beam losses increases at high intensities because the intrabeam scattering effect adds to vacuum losses. Detailed investigations into the ion kinetics under consideration of the effects from electron cooling and multiple scattering of the beam on a supersonic gas jet target have been carried out as well. The lifetime, equilibrium momentum spread and equilibrium lateral spread during collisions with this internal gas jet target were estimated. In addition, the results from experiments at the TSR ring, where low-intensity beam of  $CF^+$  ions at 93 keV/nucl. has been shrunk to extremely small dimensions have been reproduced. Based on these simulations, conditions for stable ring operation with extremely low-emittance beam are presented. Finally, results from studies into the interaction of ions with a gas jet target at 3–30 keV energy range are summarized.

Применение накопительных колец в области ультранизких энергий и, в частности, электростатических накопительных колец оказалось неоценимым инструментальным средством для молекулярной и атомной физики. Вследствие независимости электростатической жесткости от

---

\*E-mail: alexander.papash@kit.edu

массы ионов такие машины способны накапливать широкий спектр различных частиц от легких ионов до тяжелых однозарядных молекул. Однако ранние эксперименты показали сильное ограничение интенсивности пучка, быстрое уменьшение тока пучка и снижение времени жизни. Природа этих эффектов не была полностью описана. Ряд экспериментов в будущих проектах накопителей ультранизкой энергии и устройств торможения пучка, включая изучение столкновения пучков с внутренними мишенями, требуют также исчерпывающих исследований физических процессов, присутствующих в работе таких колец. В данной статье представлен обзор исследований нелинейной и долговременной динамики на примере накопителей ELISA, AD Recycler, TSR и USR, проведенных с использованием компьютерных программ BETACOOOL, OPERA-3D и MAD-X. Результаты моделирования протестированы на основе экспериментальных данных потерь пучка в накопителе ELISA. Показано, что снижение интенсивности пучка в накопителях ультранизкой энергии, в основном, определяется потерями ионов на апертуре вакуумной камеры из-за многократного рассеяния на остаточном газе. Пучок теряется на апертуре камеры благодаря малому размеру аксептанса накопителя. Скорость потерь частиц увеличивается с ростом интенсивности, потому что эффект внутривидового рассеяния добавляется к потерям на остаточном газе. Также выполнено детальное исследование кинетики ионов под воздействием эффектов электронного охлаждения и многократного рассеяния пучка на атомах газовой мишени. Сделаны оценки времени жизни пучка, равновесного продольного и поперечного разброса по импульсам вследствие взаимодействия с внутренней газовой мишенью. Кроме того, воспроизведены эксперименты на накопителе TSR, где низкоинтенсивный пучок ионов  $CF^+$  на энергии 93 кэВ/нукл. был сжат до экстремально малого поперечного эмиттанса. На основе этих расчетов сформулированы условия для получения устойчивой работы накопителя с предельно малым поперечным эмиттансом. В конце статьи представлены результаты исследований взаимодействия ионов с газовой мишенью в области энергий 3–30 кэВ.

PACS: 29.20.db; 29.27.Bd

## INTRODUCTION

Electrostatic Storage Rings (ESR) operate at ultralow energies and have proven to be invaluable tools for atomic and molecular physics, in particular, at  $\sim 1$  to 100 keV/nucl. energy range.

Storage devices like ion traps and ESR have been developed in response to the needs of the astro-, atomic and molecular physics communities [1, 2]. The electrostatic bending and focusing elements are used in electrostatic storage rings rather than bending magnets and focusing magnetic quadrupoles like in magnetic storage rings.

The main difference from magnetic storage rings is that the electrostatic rings are mass-independent and have no upper mass limit on the ion mass that can be stored [1]. While in the magnetic storage rings the magnetic rigidity depends on ion charge to the ion mass ratio  $Q/A$ , the electric rigidity and voltage applied to the electrostatic bending elements in ESR are proportional to the ion kinetic energy  $T$  and ion charge  $Q$  but do not depend on atomic number  $A$ . Due to the mass independence of the electrostatic rigidity, these machines are able to store a wide range of different particles, from light ions to heavy singly charged biomolecules.

As opposed to magnetic storage rings, ESR have essentially lower limit on the beam energy because of the absence of eddy currents and hysteresis in bending

elements. In addition, the new kind of experiments in atomic and molecular physics research — the so-called reaction microscope incorporated into a ring lattice — is considered to be a new powerful tool to study high precision effects by multiple crossing of incident beam of ions with ultrasonic gas jet [3].

Despite their distinct advantages for fundamental research in the low-energy regime, only few electrostatic ion storage rings are in operation around the world, all of them having a comparable, compact racetrack-shape layout and working at a fixed energy of 20 [4, 5] or 30 keV [6] with a continuous (CW) beam. A double electrostatic ring, operating in a merged beam configuration and at temperatures below 20 K, is presently being built at the Manne Siegbahn Laboratory in Stockholm [7]. In addition, a fixed-energy storage ring for energies up to 50 keV was designed and assembled at the University of Frankfurt [8], a Cryogenic Storage Ring (CSR) is being built up at the Max Planck Institute for Nuclear Physics [9], and a fixed-energy machine for beam energies of up to 30 keV is presently being constructed at KACST in Saudi Arabia [10].

Beam parameters were measured in operating electrostatic rings, namely: the emittance, the beam profile, the beam current loss rate, the energy spread, etc. [4–6]. Strong limitations on beam intensity, reduced lifetime were indicated. The ion losses strongly depend on a ring optical structure and beam current. The nature of these effects was not fully understood.

Some possible effects that may limit the beam current and lifetime have been proposed so far [11], including nonlinear fields in the electrostatic elements, parametric resonances due to modulations of the space charge tune shift, as well as coupling between the longitudinal and transverse particle motion [12]. It has been noted that excessive beam losses occurred already at beam intensities that were too low to be explained by a negative shift of the betatron tune due to space charge or by parametric resonances.

The understanding of beam behavior, especially nonlinear effects, long term beam dynamics, ion kinetics and ion equilibrium conditions in an ultralow energy storage rings, will pave way for a successful operation of these machines. Therefore, additional studies were initiated to improve the knowledge of the nature of beam losses and physics of processes in an ultralow energy storage rings.

## 1. NONLINEAR EFFECTS IN ELECTROSTATIC STORAGE RINGS

We have simulated beam behaviour including nonlinear terms of equations of motion derived from Fourier harmonic analysis of electric field distribution in the electrostatic deflectors. Also we have tracked ions in the computer model of the ring using the relaxation electric field maps of bending and focusing elements. Finally, we investigate transition processes, equilibrium conditions and long term beam dynamics based on kinetic equations and propose consistent explanation of some effects observed so far in the ultralow energy storage rings.

To verify our computer studies, we choose an example of the ELISA — the first electrostatic ring dedicated to atomic physics experiments [13]. ELISA is successfully operating in Aarhus University since the 1990s (Fig. 1 was kindly presented by S. P. Moller) [14]. In ELISA ring two  $160^\circ$  electrostatic deflectors and two  $10^\circ$  parallel plate deflectors together with four sets of electrostatic quads form simple racetrack structure (Fig. 2 is taken from [15]). Splitted deflectors allow one to detect neutrals at the end of straight sections. Rings with similar lattices have been built in KEK [5] and Tokyo University [6]. Deflectors of spherical shape have been used in the original design of the ELISA ring in order to provide equal focusing in both horizontal and vertical planes [14], but later on, have been substituted by electrostatic deflectors of cylindrical shape.



Fig. 1. Photo of compact electrostatic storage ring ELISA kindly presented by S. P. Moller [13]

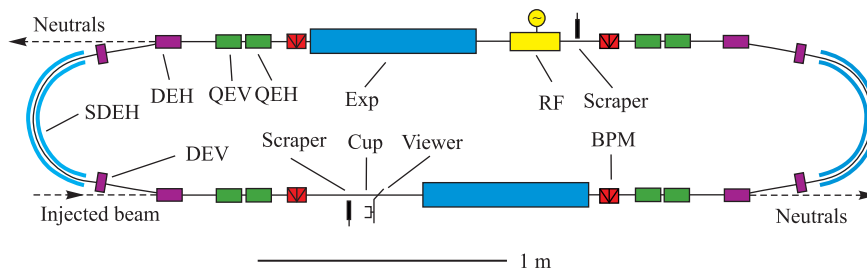


Fig. 2. Layout of ELISA storage ring taken from [14]. Ions are bent in  $10^\circ$  parallel plate deflectors (DEH) and  $160^\circ$  spherical deflectors (SDEH) and focused by electrostatic quads QEH and QEV. Neutrals might be detected after passing  $10^\circ$  parallel plate deflectors — DEH

Systematic studies of beam parameters in ELISA showed essential limitations on beam current, reduced lifetime. Strong decay of the beam of negative oxygen ions stored at 22 keV has been measured in ELISA ring, and experimental results are presented in Fig. 3, *a* taken from [15]. The ion losses in this ultralow energy

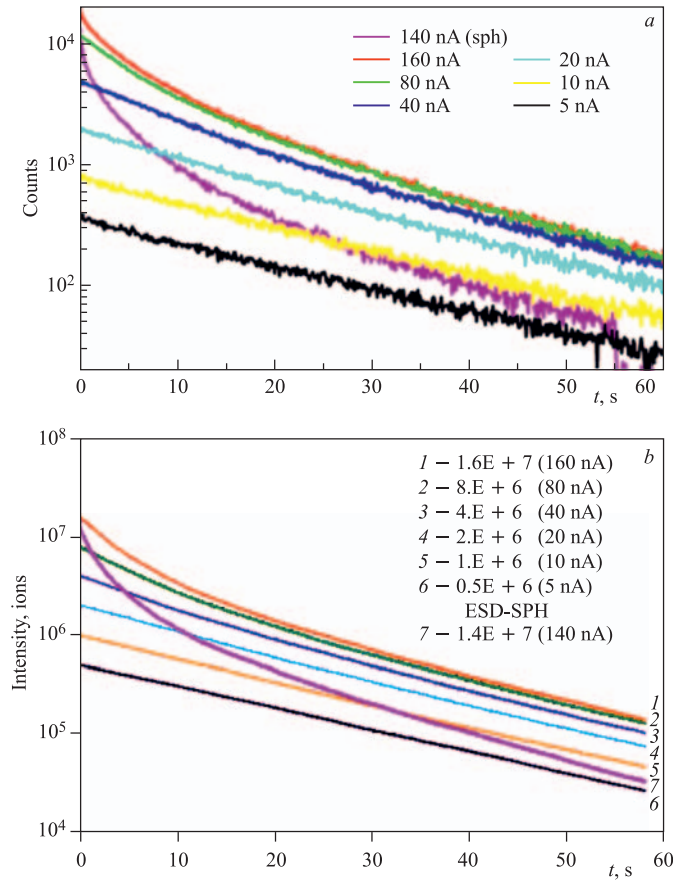


Fig. 3 (color online). Decays of stored negative oxygen  $O^-$  ions in ELISA ring at 22 keV beam energy: *a*) experimental data taken from [15], beam lifetime  $\tau = 12$  s; *b*) BETACOOOL simulations [34, 35]. Pink curve shows the drop of the beam current in ELISA ring with electrodes of spherical shape. The rest of the data related to ELISA ring are equipped with cylindrical electrodes

electrostatic storage ring hardly depend on the beam intensity especially for the ring optical structure with spherical deflectors.

**1.1. Equations of Motion in Electrostatic Deflectors.** The theory of ion motion in electrostatic bending and focusing elements is well developed [16–18], and here we will mention only some basic formulae. In accordance with the Gauss law for two spheres

$$E_R \cdot 4\pi R^2 = \frac{q}{\varepsilon}, \quad (1)$$

the potential between internal sphere of radius  $R_1$  and external sphere of radius  $R_2$  is changed as

$$\varphi(R) = -\frac{2U_0}{R_2 - R_1} R_2 R_1 \frac{1}{R} + \frac{U_0}{R_2 - R_1} (R_2 + R_1), \quad (2)$$

where the boundary conditions are  $\varphi(R_1) = -U_0$  and  $\varphi(R_2) = U_0$ .

A deflector of cylindrical shape might be considered as a spherical one with infinite radius in vertical plane  $\rho \rightarrow \infty$ . The distribution of potential between electrodes of cylindrical shape, providing the voltage  $\pm U_0$  is applied to external/internal electrodes, is

$$\varphi(R) = -U_0 + \frac{2U_0}{\ln R_2/R_1} \ln \frac{R}{R_1}. \quad (3)$$

The theory obeys paraxial law in ion optics, i.e., the deviation of ions from the equilibrium orbit of radius  $R_{\text{eq}}$  is small in both planes  $x/R_{\text{eq}} \ll 1$  and  $y/R_{\text{eq}} \ll 1$ . Cutting the Taylor expansion to the second power, the expressions for particle oscillations in the spherical deflector might be written as

$$x'' + \frac{1}{R_{\text{eq}}^2} x - \frac{1}{R_{\text{eq}}^3} x^2 - \frac{3}{2R_{\text{eq}}^3} y^2 = 0, \quad y'' + \frac{1}{R_{\text{eq}}^2} y - \frac{3}{R_{\text{eq}}^3} xy = 0. \quad (4)$$

Second order equations of motion for spherical deflector include sextupole components as well as coupling between radial and vertical planes. In linear approximation the spherical deflector provides equal focusing in both horizontal and vertical planes

$$x'' + \frac{1}{R_{\text{eq}}^2} x = 0, \quad y'' + \frac{1}{R_{\text{eq}}^2} y = 0. \quad (5)$$

The second order motion in the cylindrical deflector is described by the formulae:

$$x'' + \frac{2}{R_{\text{eq}}^2} x - \frac{1}{R_{\text{eq}}^3} x^2 = 0, \quad y'' = 0. \quad (6)$$

The sextupole component for the deflector of cylindrical shape is smaller than for spherical deflector and affects only the horizontal plane. Also there is no coupling between horizontal and vertical motion in cylindrical deflector at least up to the second order.

The focusing strength of cylindrical deflector in horizontal (bending) direction is twice as much as of spherical one. In vertical direction cylindrical deflector might be considered as a drift:

$$x'' + \frac{2}{R_{\text{eq}}^2} x = 0, \quad y'' = 0. \quad (7)$$

At low energies ( $\beta \ll 1$ ) the linear transfer matrix  $\mathfrak{R}$  of electrostatic deflector with bending angle  $\theta$ , bending radius  $R$  and effective length  $L = \theta R$  might be written in the nonrelativistic form [26], where the electric field index  $n = 1$  for cylindrical deflector and  $n = 2$  for deflector of spherical shape



**1.2. Acceptance and Betatron Tune Shift in the ELISA Ring.** In order to study the ion motion and nonlinear effects, we have created geometrical model of the storage ring similar to ELISA which is composed of main bending and focusing elements and put it into the commercial 3D field simulation code OPERA [19]. This code package includes a number of different modules, amongst which the electrostatic 3D field solver TOSCA and program SCALA that allows for beam tracking under the influence of space charge effects. The ring model consists of two main electrostatic deflectors that bend the beam by an effective angle of  $160^\circ$ , two pairs of  $10^\circ$  parallel plate deflectors and four pairs of electrostatic quadrupoles (Fig. 4). In order to benchmark earlier experimental data, two maps were created with both spherical and cylindrical deflectors implemented for the main bending elements. First, a closed orbit was searched for in the OPERA ring model to track ions for many turns in the full 3D electric fields, see Fig. 4.

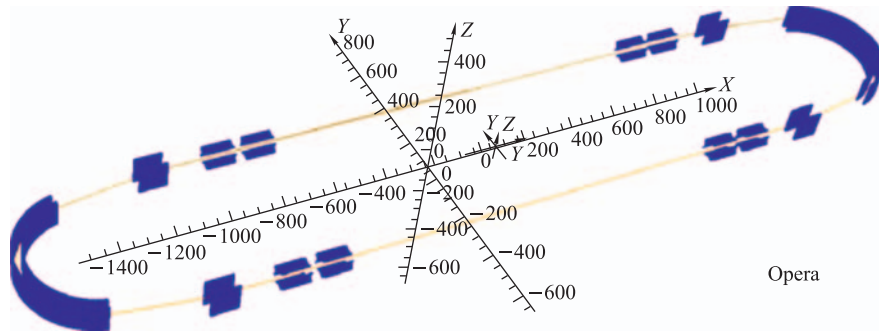


Fig. 4. Model of the ELISA ring in OPERA-3D. The dimensions and distances were taken from [4, 13]. Particles were tracked over many turns in order to find stable solution for closed equilibrium orbit

Linear ion optics parameters of ELISA ring, such as the beta-functions, betatron tunes, dispersion function, etc., were first verified by implementing the ring lattice geometry in the computer codes TRACE-3D [20] and MAD-X [21]. We have incorporated linear transfer matrixes for electrostatic elements, see Eq. (8), into the MAD-X because the program does not support electrostatic deflectors [22]. The periodicity of ELISA ring is 2 and example of one cell of ELISA ring lattice starting in the middle of the  $160^\circ$  deflector is shown in Fig. 5. Strong waist in horizontal plane  $\beta_X = 0.14$  m is required in the middle of electrostatic deflector of spherical shape in order to match linear lattice functions (Fig. 5, *a*). Also there are two sharp minimum of vertical beta-function  $\beta_Y = 0.1$  m inside the  $160^\circ$  deflector due to the strong focusing of spherical shape electrodes in the vertical plane. When spherical deflector is replaced by cylindrical electrodes acting as a drift in vertical direction, the vertical beta-function

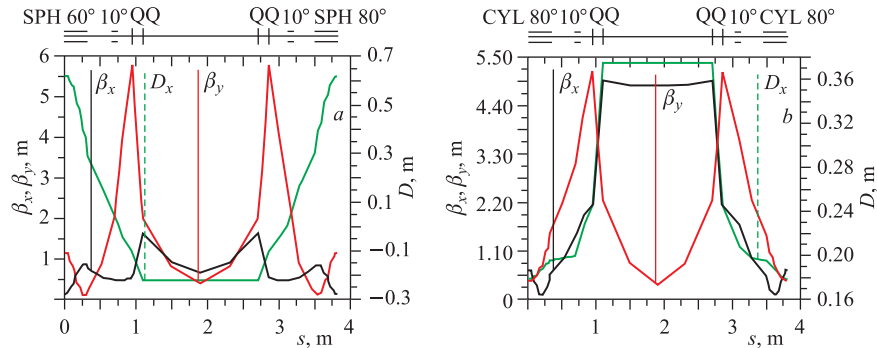


Fig. 5. Example of ELISA cell lattice starting at the middle of  $160^\circ$  deflector: *a*) ESD of spherical shape; *b*) ESD of cylindrical shape. The ring superperiodicity is 2. MAD-X simulations with electrostatic deflector matrixes [22]

inside the deflector can be varied between 0.2 and 2 m but the higher value of the beta-function is accompanied by a reduction of the vertical betatron tune to  $\nu_z < 1$ . Early ELISA tests [13] indicated that regimes with a vertical tune of less than one are unstable, and ring operation with  $160^\circ$  cylindrical deflectors was performed with vertical waist  $\beta_y = 0.4$  m in the middle of deflector and two strong focal minimums in radial plane  $\beta_x = 0.1$  m inside of the deflector as shown in Fig. 5, *b*.

For further analysis we use the MAD-X code with electrostatic matrixes and implement field nonlinearities as aberration factors for a stable analytical solution [23]. Field integrals were calculated along trajectories inside deflectors at a distance of 14 mm from equilibrium orbit (gap between electrodes inside the  $160^\circ$  deflector is 30 mm), and Fourier analysis of field integrals has been performed using OPERA-3D/TOSCA code. The resulting amplitudes of electric field harmonics normalized to the main dipole component ( $n = 1$ ) are listed in Table 1. The sextupole component of electric field distribution in the deflector of spherical shape is more than three times larger than for the cylindrical deflector. Strong sextupole component leads to reduced region of stable betatron motion in storage rings.

Table 1. Integral electric field harmonics of the cylindrical and spherical deflector. Data are normalized to the main dipole component  $n = 1$  [23]

No.	1	2	3	4	5	6
Harmonic	Dipole	Quadrupole	Sextupole	Octupole	Decapole	Hexapole
ESD-CYL	1	$5.6 \cdot 10^{-2}$	$1.7 \cdot 10^{-3}$	$4.3 \cdot 10^{-5}$	$2.7 \cdot 10^{-5}$	$1.9 \cdot 10^{-5}$
ESD-SPH	1	$1.1 \cdot 10^{-1}$	$6.1 \cdot 10^{-3}$	$1.3 \cdot 10^{-3}$	$3.4 \cdot 10^{-4}$	$1.0 \cdot 10^{-4}$

We have tracked particles using MAD-X code with nonlinear terms of electric field distribution and found dynamic aperture of the ELISA ring. High order Fourier components of electric field distribution were considered as field errors and implemented over the total length of each deflector as a set of thin multipole elements spaced at equal azimuth steps. We found that all nonlinear terms of electric field distribution reduce ring acceptance, and most important is sextuple one. The dynamic aperture of the ring with deflectors of spherical shape is essentially smaller than region of stable motion of the ring with cylindrical deflectors, especially in the vertical direction (Fig. 6).

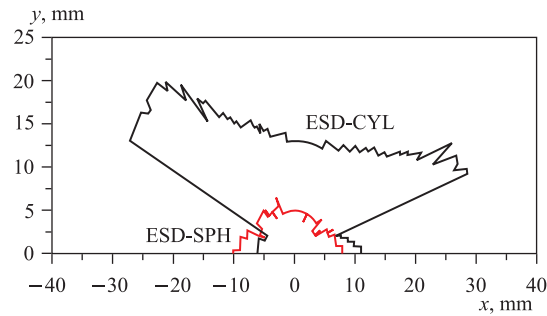


Fig. 6. Dynamic aperture of the ELISA storage ring with deflectors of cylindrical shape and ring with spherical deflectors. MAD-X nonlinear simulations [23]

Also the amplitude dependence of betatron tunes in the model of ELISA ring has been studied. We use Fast Fourier Transformation analysis (FFT) of phase space profile of tracked beam and derive the fractional part of the betatron tune [23]. For a span of radial oscillations  $\pm 10$  mm the horizontal betatron tune spread is  $3 \cdot 10^{-3}$  in the case of ring with cylindrical deflectors and tune spread is  $3.5 \cdot 10^{-2}$  for ring with spherical deflectors. The betatron tune spread in the vertical direction is  $3.5 \cdot 10^{-3}$  for cylindrical deflector and  $4 \cdot 10^{-2}$  (i.e., 10 times more) for spherical one. At the tune diagram of the ring model where fractional part of betatron tunes is shown, one can see that the tune spread of ring with spherical deflectors is much more wide than of the ring with cylindrical deflectors (Fig. 7). Betatron tune of ring with spherical deflector is close to third order resonance and crosses higher order resonances which is in agreement with estimations provided in [12].

Finally, the ring acceptances in the radial and axial phase spaces were estimated by tracking the beam orbits over many turns in relaxation electric field grid generated by the OPERA-3D computer code (Fig. 4). Initial position and momentum of ions with respect to the reference orbit have been varied over a wide range to find max amplitude of stable betatron oscillations [22]. As can be seen from the phase space diagram of ELISA ring model shown in Fig. 8, the nonlinearities, i.e., distortions of radial and vertical phase spaces became clearly

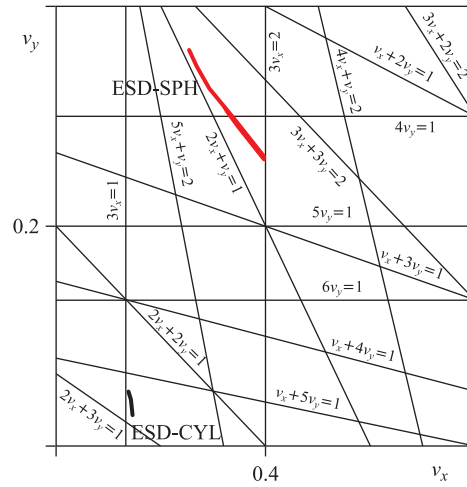


Fig. 7. Amplitude-dependent tune shift in the ring with deflectors of spherical and cylindrical shape [23]

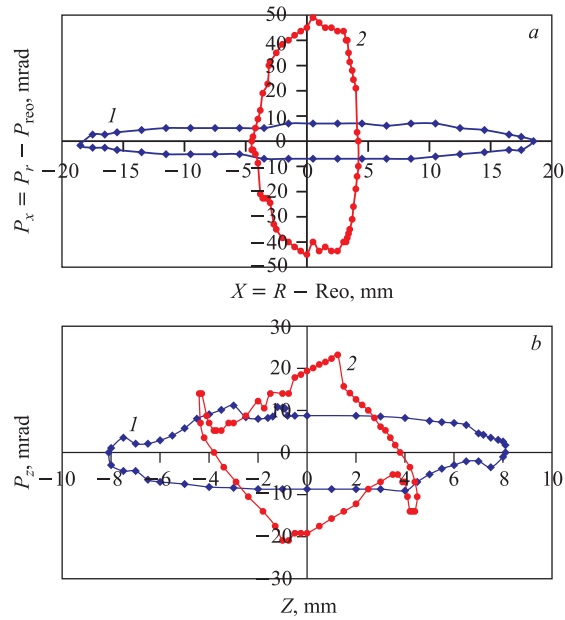


Fig. 8. Acceptance of ELISA ring [22]. Stable orbits have been tracked in relaxation electric field mesh generated by OPERA-3D/TOSCA software: *a*) radial phase space; *b*) vertical phase space. The middle of long straight section is marked as 1 and the middle of  $160^\circ$  deflector of cylindrical shape – as 2. Ring acceptance in vertical plane is less than  $30 \pi \text{ mm} \cdot \text{mrad}$

visible in both planes especially in the vertical direction. Estimated acceptance in radial plane is less than the ring acceptance determined by available space between focusing elements (Fig. 8, *a*). Also the ring acceptance in the vertical plane is less than in horizontal direction and should not exceed  $A_z < 30\pi$  mm · mrad, i.e., few times smaller than would be expected from geometric considerations of available free space between electrodes and from large vertical extensions of deflectors (Fig. 8, *b*). For spherical deflectors, the acceptances in both planes were even more limited and thus the effects more pronounced.

The next step in our studies was to find the main force(s) that drive low energy ions to the periphery of the reduced ring acceptance.

## 2. ION KINETICS AND LONG-TERM BEAM DYNAMICS

In order to find the driving forces responsible for pushing ions out of the aperture of ELISA ring as well as for the reduced beam lifetime, for the ion intensity losses and the beam degradation, we have studied transition processes and equilibrium conditions in an ultralow energy storage rings. We derived growth rates of root-mean-square (r.m.s.) beam emittance and r.m.s. momentum spread, by simulating the evolution of the ion distribution function with time. The BETACOOOL code was employed to study the long-term beam dynamics in low energy storage rings [24]. The program was initially developed by JINR scientists (Dubna, Russia) in collaboration with leading scientific centers worldwide in order to estimate heating and cooling effects in high-energy storage rings with electron cooling [25]. The BETACOOOL code was successfully benchmarked at BNL RHIC (USA) [26–28], RIKEN (Japan) [29, 30], COSY synchrotron (KFZ, Juelich, Germany) [31, 32], ESR and HESR storage rings (GSI, Darmstadt, Germany) [33, 34], CELSIUS storage ring (Uppsala, Sweden) [35], S-LSR ring of Kyoto University (Japan) [36], etc.

The program is under development and new physics models in different energy regimes are implemented as well. At present the code might be applied to study electron, stochastic, gated stochastic and laser cooling methods as well as interaction of circulating ions with residual gas, interaction with different kinds of internal targets, intrabeam scattering, beam–beam collisions, external heating of ion beam, different kinds of particle losses, barrier RF bucket regime, etc.

General goal of the BETACOOOL program is to simulate long-term beam dynamics (in comparison with the ion revolution period in a ring) leading to variation of the ion distribution function in 6-dimensional phase space. The betatron motion inside a storage ring is supposed to be stable and it is treated in linear approximation. Nonlinear effects strongly restrict amplitude of stable betatron oscillations in storage rings. In our studies we take into account nonlinear effects by variation of ring acceptance as input parameters in the BETACOOOL code [37, 38].

**2.1. Kinetic Equations.** Studies of ion kinetics in storage rings are based on the applying of stochastic (kinetic) differential equations to the periodic motion with an assumption that diffusion, i.e., heating processes as well as friction, i.e., cooling processes leading to the growth, reducing or equilibrium of beam phase space, are small with respect to electromagnetic forces from external bending and focusing elements. Evolution of the ion distribution function is described by the Fokker–Planck equation [39]

$$\frac{\partial f}{\partial t} = - \sum_{i=1}^N \frac{\partial}{\partial x_i} [D_i^1(x_1, \dots, x_N) f] + \sum_{i=1}^N \sum_{j=1}^N \frac{\partial^2}{\partial x_i \partial x_j} [D_{ij}^2(x_1, \dots, x_N) f], \quad (9)$$

where  $f$  is a probability density of distribution function of ions in the ring;  $D^1$  is the drift vector and  $D^2$  is the diffusion tensor — the latter results from the presence of the stochastic forces. Friction and diffusion terms in the general case depend on the distribution function. The main methods of the solving of the stochastic differential equations are based on the transformation of initial kinetic equation to the form of Fokker–Planck equation and on the finding of the solution for density distribution probability function. In some cases, when the effects acting on the distribution function do not lead to the change of its shape, the Fokker–Planck equation can be reduced to equation for the second-order moments of the distribution function or Langevin equation in invariant or momentum space.

Few numerical algorithms are realized in BETACOOOL in order to simulate evolution of the ion distribution function: the RMS (root mean square) dynamics, the Model Beam (MB) algorithm and the MultiParticle Tracking (MPT) algorithm. Three different numerical methods verify each other and also help to validate the action from different physical effects. If initially the Gaussian distribution is chosen, then the evolution of r.m.s. parameters should be the same while the shape of the distribution function does not change.

RMS dynamics calculates evolution in time of the r.m.s. parameters of the ion distribution function during motion in the storage ring under a common action of a few heating and cooling effects. Each effect might be artificially included or excluded from the consideration in order to distinguish effects from different processes. RMS algorithm is based on solution of system of four differential equations for the second-order momentum in all degrees of freedom including equation for the beam intensity change

$$\frac{d\epsilon_x}{dt} = \frac{\epsilon_x}{\tau_{\text{hor}}}, \quad \frac{d\epsilon_y}{dt} = \frac{\epsilon_y}{\tau_{\text{vert}}}, \quad \frac{d\epsilon_{\text{long}}}{dt} = \frac{\epsilon_{\text{long}}}{\tau_{\text{long}}}, \quad \frac{dN}{dt} = \frac{N}{\tau_{\text{life}}}, \quad (10)$$

where  $\epsilon_x$  and  $\epsilon_y$  are r.m.s. emittances in  $x$  and  $y$  transverse planes. The longitudinal r.m.s. emittance  $\epsilon_{\text{rms}}^{\text{long}}$  for the coasting beam is determined as a square of

r.m.s. relative momentum spread  $\sigma_{\text{long}}$

$$\varepsilon_{\text{long}}^{\text{rms}} = \sigma_{\text{long}}^2 = \left( \frac{\Delta p^{\text{rms}}}{p} \right)^2. \quad (11)$$

Characteristic times  $\tau_i$  of evolution of the beam parameters are estimated under assumption of Gaussian shape of the distribution function

$$\frac{1}{\tau_i} = \frac{\varepsilon_{\text{fin}} - \varepsilon_{\text{in}}}{\varepsilon_{\text{in}} T_{\text{rev}}}, \quad (12)$$

where  $T_{\text{rev}}$  is the revolution time. Rates  $1/\tau_i$  are positive for heating processes and negative during cooling. The beam lifetime is inversely proportional to the average value of ion loss probability  $\langle P_{\text{loss}} \rangle$

$$\frac{1}{\tau_{\text{life}}} = -\frac{\langle P_{\text{loss}} \rangle}{T_{\text{rev}}}. \quad (13)$$

The negative sign of the lifetime  $\tau_{\text{life}}$  corresponds to the particle loss and positive sign corresponds to particle number increase during injection. No particle tracking is done in the frame of the RMS algorithm.

Investigation of the ion beam dynamics at arbitrary shape of the distribution function is performed using multiparticle simulation in the frame of the Model Beam algorithm. In this algorithm, the ion beam is presented by array of few thousands modelling particles. MB algorithm realizes solution of Langevin equation in invariant or momentum space. The heating and cooling processes lead to change of the particle momentum components and particle number, what is calculated in accordance with step of dynamics simulation over time. Each effect is located in some position characterized by the ring lattice functions. Action of each heating or cooling effect is simulated as variation of a particle momentum (kick) at certain point of the ring

$$\left( \frac{p_{x,y,s}}{p} \right)_{\text{fin}} = \left( \frac{p_{x,y,s}}{p} \right)_{\text{in}} + \Lambda_{x,y,s} \Delta T + \sqrt{D_{x,y,s} \Delta T} \xi_{x,y,s}, \quad (14)$$

where  $p_{x,y,s}$  are particle momentum deviations before (in) and after (fin) action of effect.  $\Lambda$  and  $D$  are the drift and diffusion terms,  $\Delta T$  is the time integration step,  $\xi$  is the Gaussian random number at unit dispersion. The beam motion inside the ring is simulated by applying linear transfer matrixes at random phase advance between the effect locations. The betatron coordinates are transformed in accordance with the coefficients of the ring matrix in the point of the array generation

$$\begin{aligned} \begin{pmatrix} x \\ x' \end{pmatrix}_{i+1} &= \begin{pmatrix} R_{11} & R_{12} \\ R_{21} & R_{22} \end{pmatrix} \begin{pmatrix} x \\ x' \end{pmatrix}_i, \dots, \begin{pmatrix} y \\ y' \end{pmatrix}_{i+1} = \\ &= \begin{pmatrix} R_{33} & R_{34} \\ R_{43} & R_{44} \end{pmatrix} \begin{pmatrix} y \\ y' \end{pmatrix}_i, \end{aligned} \quad (15)$$

where  $R_{ij}$  are elements of the ring linear transfer matrix  $\{R\}$  in 2D phase space. The beam motion in the longitudinal plane is provided with the rotation matrix:

$$\begin{pmatrix} s - s_0 \\ \frac{\Delta p}{p} \end{pmatrix}_{i+1} = \begin{pmatrix} \cos \mu & B_s \sin \mu \\ -\frac{1}{B_s} \sin \mu & \cos \mu \end{pmatrix} \begin{pmatrix} s - s_0 \\ \frac{\Delta p}{p} \end{pmatrix}_i, \quad (16)$$

where value of phase advance  $\mu$  can be arbitrary nonzero.

Multiparticle Tracking algorithm (MPT) uses real particles with arbitrary distribution and modeling of optical elements including Hamiltonian with nonlinear and space charge terms. The Molecular Dynamic (MD) technique [40] is applied in the BETACOOOL code as a part of the MPT procedure with the assumption that particles in the coasting beam have periodic distribution along the ring. For bunched beam one can simulate the beam dynamics using the so-called «macro» particles. MD is used for simulation of IntraBeam Scattering (IBS) as well as to study crystalline beams. For the detailed description of the MPT procedure we refer to [25].

**2.2. Multiple Scattering of Ions.** In low energy storage rings, the growth of beam emittance is caused mainly by small angle multiple Coulomb scattering of circulating ions on atoms and molecule of residual gas (vacuum losses) as well as due to the IntraBeam Scattering (IBS) when beam intensity is high. If internal target is installed in the ring, the circulating ions are lost because the projectile beam is scattered on atoms of target when particles cross gas jet many times. The transverse beam emittance also might grow due to energy straggling (fluctuations of energy losses) if dispersion is not zero in the ring.

*2.2.1. Rate of R.M.S. Emittance Growth.* We briefly outline here effects of internal thin target based on formalism proposed in [41] and applied in BETA-COOOL to simulate interaction of beam with target as well as vacuum losses [25]. Influence of internal target on the beam is studied in the frame of all three numerical algorithms. For Multiparticle Tracking, the target is approximated by a thin lens associated with some optic element of the storage ring, and the target action on the ion is presented in the form of transformation map, see Eqs. (13) and (14). The variations of r.m.s. emittance and particle number, see Eqs. (10) and (11), are described by few models of characteristic time which are based on the transformation maps. For investigation of long term processes in the frame of the Model Beam algorithm, the internal target is presented in the form related to the kick of the ion momentum and the loss of probability calculation.

Assuming a Gaussian distribution in both position  $y$  and angle ( $y'$ ) coordinates, where  $yy'$  are referred either horizontal or vertical position and angular displacement of particle with respect to the reference orbit, the two-dimensional probability distribution function  $\rho(y, y')$  describing projection of 6D phase space

on the 2D phase plane  $(yy')$ , can be written as

$$\rho(y, y') = \frac{1}{2\pi\varepsilon_{\text{rms}}} \exp\left(-\frac{\varepsilon}{2\varepsilon_{\text{rms}}}\right). \quad (17)$$

The r.m.s. beam distribution can be approximated by an equivalent ellipse described by Twiss parameters  $\alpha$ ,  $\beta$ ,  $\gamma$ . The equivalent ellipse with an area  $\pi\varepsilon$  as defined by the equation

$$\varepsilon = \gamma y^2 + 2\alpha yy' + \beta y'^2 \quad (18)$$

is a curve of constant density  $\rho$  in the phase space enclosing certain percentage of ions in the beam. The r.m.s. emittance  $\varepsilon_{\text{rms}}$  is given by mean square values (second moments) of normal (Gaussian) beam distribution

$$\varepsilon_{\text{rms}} = \sqrt{\langle y^2 \rangle \langle y'^2 \rangle - \langle yy' \rangle^2} = \sigma_y \sigma_{y'} \sqrt{1 - r^2}, \quad (19)$$

where  $\sigma_y = \sqrt{\langle y^2 \rangle}$  is the r.m.s. beam width and  $\sigma_{y'} = \sqrt{\langle y'^2 \rangle}$  is the r.m.s. beam angular width. The correlation term  $r = \sigma_{yy'} = \langle yy' \rangle$  vanishes in focal plane where phase space ellipse is «upright» and tilt angle is zero. The r.m.s. emittance might be estimated by the formulae

$$\varepsilon_{\text{rms}} = \frac{\sigma_y^2}{\beta} = \frac{\sigma_{y'}^2}{\gamma}. \quad (20)$$

The normalized emittance  $\varepsilon_y^{\text{norm}}$  is proportional to the percentage of the beam enclosed into the phase space ellipse and is estimated by the expression

$$\varepsilon_y^{\text{norm}} = \beta\gamma n_\sigma \varepsilon_y^{\text{rms}}, \quad (21)$$

where  $\beta\gamma$  are relativistic factors and  $n_\sigma = -2 \ln(1 - \alpha/100)$  — number of sigma  $\sigma$  calculated via percentage of the beam intensity  $\alpha[\%]$  for the Gaussian distribution. Values of coefficients  $n_\sigma = 1$ ,  $n_\sigma = 4$ , and  $n_\sigma = 5.991$  correspond to 39.3, 86, and 95% of total beam intensity, respectively.

Gas jet target in the BETACOOOL is treated as an equivalent of a thin lens in ion optics [41]. Ion after crossing the target does not change the coordinate but experience angular scattering, i.e., all three components of particle momentum are changed and particle might be lost with some probability. Change of transverse momentum is related mainly to a multiple Coulomb scattering of ions on the nuclei of target atoms. Longitudinal momentum of ion is reduced because of the ionization and excitation energy losses occurring during interaction of ion with electron shell of target atom. Fluctuation of ionization energy losses leads to the growth of the beam momentum spread.

A collision of incident ion with thin target atom produces a small angle kick  $\Delta y'$  which is of stochastic nature. Introducing the mean square scattering angle

per target traversal,  $\theta_{\text{rms}}^2$ , one can describe the scattering heating rate in horizontal or vertical transverse plane by the formula

$$\frac{1}{\tau_{h,v}} = \frac{1}{2} \frac{\beta_{h,v}}{\varepsilon_{h,v}} \frac{\theta_{\text{rms}}^2}{T_{\text{rev}}}. \quad (22)$$

In presence of dispersion  $D$  and derivative of dispersion  $D'$ , the emittance growth after  $N$  target traversals depends not only on r.m.s. scattering angle but also on momentum spread  $\delta_{\text{rms}}^2$  introduced by fluctuations of the ionization and excitation energy losses

$$\begin{aligned} \Delta\varepsilon_{h,v} = \varepsilon - \varepsilon_0 = N \frac{\beta_{h,v} \theta_{\text{rms}}^2}{2} + \\ + \frac{N}{2} \left( \frac{(1 + \alpha_{h,v})^2}{\beta_{h,v}} D_{h,v}^2 + 2\alpha_{h,v} D_{h,v} D'_{h,v} + \beta_{h,v} D_{h,v}'^2 \right) \delta_{\text{rms}}^2, \end{aligned} \quad (23)$$

where  $\alpha$ ,  $\beta$ ,  $\gamma$  are Twiss parameters. The mean square relative momentum deviation per target traversal  $\delta_{\text{rms}}^2$  is defined for the coasting beam by the expression

$$\delta_{\text{rms}}^2 = \left( \frac{\delta p}{p} \right)^2. \quad (24)$$

The providing of the achromatic conditions is realized at target location, the growth of mean square beam size and growth of mean square angle after  $N$  turns might be estimated by the expressions

$$\Delta \bar{x}^2 = N \beta_x^2 \theta_{\text{rms}}^2, \quad \Delta \bar{x}'^2 = N \theta_{\text{rms}}^2. \quad (25)$$

In order to reduce growth rate of beam emittance, maximize luminosity of experiment and improve lifetime of ions, one should provide achromatic conditions and low beta mode at target location.

*2.2.2. Mean Square Scattering Angle.* Small-angle Coulomb scattering is well studied at intermediate and high energies and can be obtained from the Rutherford cross section [42]. There are no specific expressions for ion scattering at ultralow energy range which is of interest of our studies as well as of future experiments. Thus we apply expression for mean square scattering angle per one scattering event based on Moliere's formula for screened ion-atom potential [43] of the Thomas-Fermi type [44] with Fano's contribution of ion inelastic collision with atomic electrons [45]

$$\theta_{\text{str}}^2 = 2\pi\rho x \left( \frac{Z_T Z_i r_p}{A_i \beta^2 \gamma} \right)^2 \left[ \ln \left( \frac{\alpha_2^2}{\chi^2} \right) - 1 + \Delta b \right]. \quad (26)$$

Here  $\rho$  and  $x$  are the target density and thickness, and  $\rho x$  is a linear target thickness, i.e., the number of target atoms per unit area. Also  $A_T$ ,  $A_i$ ,  $Z_T$ , and  $Z_i$  are the mass number and charge of target and projectile ion,  $\beta$ ,  $\gamma$  are

relativistic factors, and  $r_p$  is the classical proton radius. The parameter  $\alpha_2$  is the upper integration constant of r.m.s. scattering angle and is proportional to the ratio of the De Broglie wavelength to the sum of the target and projectile nuclei radii. The screening angle  $\chi$  takes into account the deviation from the Born approximation [46]. The inelastic collision factor with atomic electrons  $\Delta b$  was introduced by Fano [47] and includes the constant determined by the electron configuration of the target atom and estimated from the Thomas–Fermi model.

Assuming Gaussian law of the processes, one can calculate particle longitudinal and transverse momentum variations after single crossing the target by random generation of the scattering angle:

$$x'_f = x'_0 + \sqrt{\frac{\theta_{\text{str}}^2}{2}} \xi_1, \quad y'_f = y'_0 + \sqrt{\frac{\theta_{\text{str}}^2}{2}} \xi_2, \quad (27)$$

where  $\xi_1, \xi_2$  are independent random values with Gaussian distribution at unit standard deviation.

*2.2.3. Ionization Energy Losses.* When beam crosses the target, the ion energy is lost due to excitation and ionization of atomic electrons. The expectation of the mean energy loss  $\Delta E_{\text{BB}}$  for one target traversal is calculated in BETACool in accordance with the simplified Bethe–Bloch equation [48]

$$\Delta E_{\text{BB}} = 2\xi \left[ \ln \frac{E_{\text{max}}}{I} - \beta^2 \right]. \quad (28)$$

Parameter  $\xi$  is proportional to the linear target thickness  $\rho x$  and inversely proportional to the beam energy  $\beta^{-2}$ :

$$\xi = 0.1535 \left[ \frac{\text{MeV} \cdot \text{cm}^2}{g} \right] \frac{Z_p^2 Z_T}{\beta^2 A_T} \rho x, \quad (29)$$

$Z_P$  and  $Z_T$  are the charge number of projectile and target atoms,  $A_T$  is the target atomic number. Mean ionization energy  $I$  is 13.6 eV for hydrogen and  $I \sim 16Z_T^{0.9}$  for heavier atoms. The maximum transferable energy during impact  $E_{\text{max}}$  is determined by kinematic parameters

$$E_{\text{max}} = \frac{2m_e c^2 \beta^2 \gamma^2}{1 + 2\gamma \frac{m_e}{M_i} + \left( \frac{m_e}{M_i} \right)^2}, \quad (30)$$

where  $m_e, M_i$  are electron and projectile ion mass, respectively, and  $\beta, \gamma$  are relativistic factors.

Fluctuations of the energy loss might be estimated by a square of the standard deviation of the ion distribution function in the energy space by the expression

$$E_{\text{str}}^2 = \xi E_{\text{max}} \left( 1 - \frac{\beta^2}{2} \right). \quad (31)$$

The mean energy loss, see Eq. (28), leads to deceleration of the beam while the fluctuation of the energy loss, see Eq. (31), causes growth of the ion momentum spread.

The model of plural scattering is applied in BETACOOOL for the thick targets of pellet type [25].

*2.2.4. Multiple Scattering on Residual Gas.* Growth rates due to the scattering of ions on residual gas are calculated by the same methods as were applied for thin internal target of gas jet type. The residual gas model is composed of gas cell targets which are distributed along the whole circumference of the ring. The rest gas heating rates are integrated over the whole lattice structure and lattice functions are used from each optic element, see Eq. (22). The effective partial densities of residual gas components are calculated from input vacuum value and percentage of gas composition. Energy losses are estimated with the Bethe–Bloch formulae, see Eqs. (34) and (35). The r.m.s. scattering angles of ions after scattering on atoms of residual gas as well as r.m.s. emittance and momentum spread are calculated using Eqs. (22), (26), (29), and (31). Finally, the characteristic growth rates  $1/\tau_i$  are derived in accordance with percentage of gas components.

**2.3. Particle Loss Probability.** The ion loss probability after crossing the target is proportional to a linear target density  $\rho x$ :

$$P_{\text{loss}} = \sigma_{\text{tot}} \rho x. \quad (32)$$

The total cross section of ion losses is a sum of cross sections of different processes leading to the particle losses. Among them more important are the single scattering on large angles  $\sigma_{\text{ss}}$ , capture of an electron or, in general case, the charge-exchange  $\sigma_{\text{ec}}$ , and nuclear reactions in the target at high energies  $\sigma_{\text{nr}}$

$$\sigma_{\text{tot}} = \sigma_{\text{ss}} + \sigma_{\text{ec}} + \sigma_{\text{nr}}. \quad (33)$$

The cross section of single scattering at the angle larger than the acceptance angle  $\theta_{\text{acc}}$  might be estimated by the formula

$$\sigma_{\text{ss}} = 4\pi \left( \frac{Z_T Z_p r_p}{A\gamma\beta^2} \right)^2 \frac{1}{\theta_{\text{acc}}^2}, \quad (34)$$

where  $r_p$  is the proton classic radius. The acceptance angle is estimated by the expression

$$\theta_{\text{acc}}^2 = \frac{A_{x,y}}{\pi\beta_{x,y}} \left( 1 - \frac{\varepsilon_{x,y}^2}{A_{x,y}^2} \right), \quad (35)$$

where  $A_{x,y}$  is the ring acceptance at  $x$  or  $y$  plane, and  $\beta_{x,y}$  is the corresponding value of betatron function at target position. Similar expressions are used to estimate the beam losses due to the multiple scattering of ions on residual gas.

**2.4. Intrabeam Scattering.** The IntraBeam Scattering (IBS) refers to the small-angle Coulomb scattering of ions in the beam. We are particularly interested in the IBS effects in circular accelerators. The IBS is essentially a diffusion process and leads to the relaxation of ions at thermal equilibrium and to the diffusion growth of beam volume in 6D phase space due to the variation of lattice parameters along ring circumference as well as the presence of dispersion in the ring and coupling between longitudinal and transverse motion.

The analytical calculations of IBS growth rate are based on estimation of particle momentum variation caused by Coulomb interaction with other ions of the beam. Also the molecular dynamics technique is applied for coasting beam [25]. For both techniques each optic element of the ring is presented as a map for the IBS process. IBS growth rate is averaged over all elements of a ring. Few approaches of the IBS scattering — the so-called Piwinski [49], Martini [50], Bjorken–Mtingwa [51], Jie–Wei [52], and other models might be chosen in the BETACOOOL [25]. Piwinski IBS model with smooth focusing approximation neglects the derivative of the betatron function  $\beta'$  and the derivative of dispersion function  $D'$  and does not require lattice structure but rather mean values of lattice functions. Bjorken–Mtingwa model is based on quantum-mechanical approach. Martini model as well as Bjorken–Mtingwa model takes into account ring structure, i.e., variation of beta-functions in a ring lattice, but does not include vertical dispersion.

Numerical algorithm to calculate the IBS growth rates is based on the analytical model of the collisions proposed by A. Piwinski [53]. The relative change of particle momentum after a collision between two ions leads to corresponding change of the Courant–Snyder invariant  $I = 2\epsilon$ , see Eq. (18). The variation of invariant  $\delta I$  is calculated under assumption that the position of ion is not changed during the interaction. Also the variation of the longitudinal component of particle momentum  $\delta p_{\parallel}/p$  leads to a change of transverse motion invariant  $\delta I_x$  in the horizontal plane where the dispersion and/or derivative of dispersion are not equal to zero.

The variation of the beam phase space volume can be calculated by averaging of the particle invariant change  $\delta I$  over the collisions in accordance with particle density distribution function  $\bar{P}$  which is a product of independent probability functions of particle 1 and particle 2 and is written according to independent probability density law. The bar indicates the values in the centre-of-mass (CM) reference frame. The time derivative of the average radial emittance for all particles denoted by  $\langle \epsilon \rangle$  is expressed in the CM system by the formula

$$\left\langle \frac{d \langle \epsilon \rangle}{dt \beta_x} \right\rangle = \int 2c\bar{\beta}\bar{P} \int_{\Psi_m}^{\pi} d\bar{\Psi} \int_0^{2\pi} d\bar{\phi} \frac{d\bar{\sigma}}{d\bar{\Omega}} \frac{\delta I_1}{\beta_x} \sin \bar{\Psi} d\bar{\tau}, \quad (36)$$

where the outer brackets  $\langle \dots \rangle$  indicate the average value around the ring. The first integral extends over all phase space betatron coordinates, momentum spread values, and azimuth location of two interacting particles. The  $d\bar{\sigma}/d\bar{\Omega}$  is the Rutherford cross section in the CM reference frame for the scattering into the element of solid angle at given axial  $\bar{\Psi}$  and azimuth  $\bar{\phi}$  scattering angles. The variable  $d\bar{t}$  in CM coordinate system is related to the laboratory time as  $dt = \gamma d\bar{t}$ . The  $\bar{\beta}c$  is the particle velocity in the CM coordinate system and by the assumption  $\bar{\beta} \ll 1$ . Integration variable  $d\bar{\tau}$  is the infinitesimal element of the phase space volume. The  $\bar{\Psi}_m$  is the smallest scattering angle determined by the impact parameter  $\bar{b}$

$$\tan \bar{\Psi}_m = \frac{r_i}{2\bar{\beta}^2 \bar{b}}, \quad (37)$$

where  $r_i$  is the ion classic radius. Taking into account that probability function  $\bar{P}$  is symmetric with respect to relative change of the momentum components  $\xi$ ,  $\theta$ ,  $\zeta$ :

$$\xi = \frac{p_1 - p_2}{\gamma p}, \quad \theta = \frac{p_{x1} - p_{x2}}{p}, \quad \zeta = \frac{p_{z1} - p_{z2}}{p}, \quad (38)$$

where  $p$  is the mean particle momentum and  $\gamma$  is relativistic factor, one will arrive after some transformations to the expression for the emittance change due to the IBS

$$\begin{aligned} \frac{d \langle \varepsilon \rangle}{dt \beta_x} = \frac{\pi}{4} cr_0^2 \gamma \int \bar{P} \left\{ \xi^2 + \zeta^2 - 2\theta^2 + \frac{(D^2 + \tilde{D}^2)}{\beta_x^2} \gamma^2 (\zeta^2 + \theta^2 - 2\xi^2) + \right. \\ \left. + \frac{6\gamma \tilde{D} \xi \theta}{\beta_x} \right\} \ln \left( 1 + \frac{4\bar{\beta}^4 \bar{b}^2}{r_0^2} \right) \frac{d\bar{\tau}}{\beta^3}, \quad (39) \end{aligned}$$

where  $\tilde{D} = \alpha_x D + \beta_x D'$ . Formula (39) describing the rate of emittance growth due to that intrabeam scattering is derived without any assumption about particle distribution and might be applied for arbitrary shape of particle distribution function. Analytical models of the IBS scattering in the BETACOOOL code are based on assumption that all betatron amplitudes, betatron angles, and momentum deviations obey Gaussian law distribution. Particle distribution in longitudinal direction is uniform for a coasting beam and of Gaussian shape for bunched beam.

Growth rates of the r.m.s. parameter are defined in the form of characteristic times in all analytical approaches and for Martini model might be presented as follows:

$$\frac{1}{\tau_p} = \left\langle \frac{nA}{2} (1 - d^2) f_1 \right\rangle, \quad \frac{1}{\tau_{x'}} = \left\langle \frac{A}{2} [f_2 + (d^2 + \tilde{d}^2) f_1] \right\rangle, \quad \frac{1}{\tau_{z'}} = \left\langle \frac{A}{2} f_3 \right\rangle. \quad (40)$$

Here angular brackets mean averaging over ring circumference,  $n = 2$  for coasting beam and  $n = 1$  for bunched beam. Parameter  $A$  is proportional to linear ion

density  $\lambda = N/L$  for coasting beam

$$A = \frac{\sqrt{1 + \alpha_x^2} \sqrt{1 + \alpha_z^2} c r_i^2 \lambda}{16\pi^{3/2} \sigma_{x\beta} \sigma_{x'\beta} \sigma_z \sigma_{z'} \sigma_p |\beta^3 \gamma^4|.} \quad (41)$$

Functions  $f_i$  are integrals over radial  $\nu$ , azimuth  $\mu$  and vertical angular  $z$  coordinates:

$$f_i = k_i \int_0^\infty \int_0^\pi \int_0^{2\pi} \sin \mu g_i(\mu, \nu) \ln(1 + z^2) e^{-D(\mu, \nu)z} d\nu d\mu dz. \quad (42)$$

With normalized parameters coefficients  $k_1 = 1/c^2$ ,  $k_2 = a^2/c^2$ , and  $k_3 = b^2/c^2$ . Functions  $D(\mu, \nu)$ ,  $g_i(\mu, \nu)$  are presented by the formulae

$$D(\mu, \nu) = \frac{\left[ \sin^2 \mu \cos^2 \nu + \sin^2 \mu (a \sin \nu - \tilde{d} \cos \nu)^2 + b^2 \cos^2 \mu \right]}{c^2},$$

$$g_1(\mu, \nu) = 1 - 3 \sin^2 \mu \cos^2 \nu, \quad (43)$$

$$g_2(\mu, \nu) = 1 - 3 \sin^2 \mu \sin^2 \nu + 6 \tilde{d} \sin \mu \sin \nu \cos \nu / a,$$

$$g_3(\mu, \nu) = 1 - 3 \cos^2 \mu.$$

Normalized parameters are calculated from the following expressions:

$$a = \frac{\sigma_y}{\sigma_{x'\beta}} \sqrt{1 + \alpha_x^2}, \quad b = \frac{\sigma_y}{\sigma_{z'}}, \quad c = q \sigma_y, \quad d = \frac{\sigma_p}{\sigma_x} D, \quad \tilde{d} = \frac{\sigma_p}{\sigma_x} \tilde{D}, \quad (44)$$

where

$$\sigma_x^2 = \sigma_{x\beta}^2 + D^2 \sigma_p^2, \quad \sigma_y = \frac{\sigma_p \sigma_{x\beta}}{\gamma \sigma_x}, \quad q = 2\beta\gamma \sqrt{\frac{\sigma_z}{r_i}}. \quad (45)$$

Martini model produces similar results with Bjorken–Mtingwa theory [51] if the integration over  $z$  variable is approximated by the expression

$$\int_0^\infty \ln(1 + z^2) e^{-D(\mu, \nu)z} dz \approx \frac{2L_c}{D(\mu, \nu)}. \quad (46)$$

In the most cases the Coulomb logarithm  $L_c \approx 20$ .

When the growth rates are known, one can calculate mean square scattering angle taking into account multiplication factor. The square of the scattering angle is equal to the sum of the square angles at each revolution and after  $N$  turns in the ring, the mean square angle is equal to

$$\langle \theta^2 \rangle = \frac{\varepsilon}{\beta_{x,z} \tau_{x,y}} \frac{T_{\text{rev}}}{N}, \quad (47)$$

where  $\beta_{x,z}$  is the beta function in the point of the particle array generation;  $\tau_{x,z}$  is characteristic growth time in corresponding degree of freedom. The variation of the angular deviation of the particle trajectory is calculated in accordance with Gaussian law:

$$\Delta\theta = \sqrt{\langle\theta^2\rangle}\xi, \quad (48)$$

where  $\xi$  is the random value with Gaussian distribution at unit dispersion.

Also kinetic model of IBS on the base of Bjorken–Mtingwa theory is realized in the frame of Model Beam algorithm when Langevin equation is solved for each model particle.

### 3. BENCHMARKING OF ELISA EXPERIMENTS

Long-term beam dynamics during beam circulation in the ELISA storage ring has been investigated using BETACOOOL code. We studied transition processes such as growth rates of beam emittance and momentum spread, beam intensity decay as well as equilibrium conditions by simulations of r.m.s. parameters of the evolution of the ion distribution function over the time.

To benchmark our simulations, we choose the same beam parameters as in the ELISA tests with coasting  $O^-$  and  $Mg^+$  ions (Table 2). The BETACOOOL program allows choosing and switching between different effects, and for ELISA case only heating processes were applied. Small-angle multiple scattering of the circulating ions on the residual gas atoms and molecules, IntraBeam Scattering (IBS), energy straggling and charge exchange were included in our simulations. We assume that ions in the ELISA ring are lost on the elements of ring aperture because of the high growth rate of beam r.m.s. emittance and low ring acceptance.

Table 2. BETACOOOL beam parameters of ELISA ring

Ion	$O^{16}$	$Mg^{24}$
Charge	-1	+1
Ion energy, keV	22	18.4
Initial beam intensities	$5 \cdot 10^5 - 1.6 \cdot 10^7$	$2.7 \cdot 10^7$
Ring circumference, m	7.616	7.616
Initial hor · vert · r.m.s. emittance ( $\sigma$ ), $\pi$ mm · mrad	1/1	0.7/0.35
Ring acceptance ESD-CYL, $\pi$ mm · mrad	10	10
Ring acceptance ESD-SPH, $\pi$ mm · mrad	6	6
Initial RMS momentum spread $\Delta P/P$	$10^{-3}$	$10^{-4}$
Equilibrium r.m.s. momentum spread $\Delta P/P$	$\sim 4 \cdot 10^{-3}$	$\sim 1.5 \cdot 10^{-3}$
Vacuum pressure (hydrogen), Torr	$2 \cdot 10^{-11}$	$10^{-11}$
Electron detachment lifetime of $O^-$ , s	26	—
Lifetime of $O^-$ at 22 keV, s	$\sim 12$	—

It was found that reducing of the beam intensity due to single scattering on large angles at a vacuum level of  $10^{-11}$  Torr is essentially less than from other effects, even at such a low beam energy, and we exclude the process of single scattering from further consideration.

**3.1. Ion Losses on Ring Aperture.** The lifetime of negative oxygen  $O^-$  ions due to the electron detachment in the process of ion collision with the residual gas has been measured by S. P. Moller [15] and value  $\tau_{\text{det}} = 26$  s was used in the program as an input parameter. In our studies we assume low ring acceptance even with deflectors of cylindrical shape  $A_{\text{cyl}} \approx 10\pi$  mm · mrad. As a result, the measured rates of beam intensity decay of a 22 keV beam of  $O^-$  ions (Fig. 3, *a*) have been reproduced with good accuracy, see Fig. 3, *b*. This gave rise to the conclusion that the main reasons for beam size growth in an ultralow energy storage rings are multiple scattering of ions on the atoms and molecule of the residual gas, i.e., vacuum losses as well as Coulomb repulsion of the ions from each other at high intensities, i.e., IntraBeam Scattering (IBS). As a consequence of fast beam growth, the ions are then lost on the ring aperture because of a rather small ring acceptance [37, 38]. The rate of beam losses increases at higher intensities because IBS adds to vacuum losses. The initial shape of the decay curve depends on the emittance, the momentum spread, and the intensity of the injected beam.

Kinetics of negative oxygen ions has been studied at different initial intensities — from  $5 \cdot 10^5$  up to  $1.6 \cdot 10^7$  particles in the beam. The IBS effect is clearly seen in Fig. 3, *a* and *b* as an excessive drop of beam current during the first few seconds when the beam intensity is still high (the green and red curves correspond to initially  $8 \cdot 10^6$  and  $1.6 \cdot 10^7$  ions, respectively). The long term slope of this loss curve is determined by the ring acceptance and by the rate of multiple scattering on residual gas, i.e., to the pressure level in the ring. The slope of the decay curve also depends on the lifetime due to electron detachment for negative ions or electron stripping for positive ions. At very low beam intensities, when IBS is negligible and only multiple scattering on the residual gas is present, the loss rate does not depend on the beam current or details of the ring lattice. That is why all lines in Fig. 3 are almost parallel towards the end of the cycle.

An exception is seen in the pink curve with more tilted slope, representing the decay of the beam intensity in ELISA with spherical deflectors (Fig. 3). In our assumption, significantly higher loss rates are caused in this case by the reduced ring acceptance. Also effect of IBS is stronger when the beam density is high and thus in particular in the regions where the beam is strongly focused. The IBS rates for ELISA with spherical deflectors are higher than with cylindrical electrodes because of the double focusing effect of the first and the resulting small beam size in both planes. As was shown in our studies into nonlinear effects [22] as well as in the previous section of this paper, the ELISA ring acceptance in vertical plane is mainly restricted by the sextupole component of the electric field of electrostatic

deflectors and should be less than  $30\pi$  mm · mrad. Any misalignments of beam equilibrium orbit out of the central curve in the middle between deflector plates will further reduce area of stable motion. Thus, the real value of ring acceptance will be even less than follows from our idealized OPERA-3D model studies.

Since the long range slope of the decay curve depends on the ring acceptance and is in full agreement with the fact that the ring acceptance with spherical electrodes is smaller than with cylindrical electrodes, the fast decay in ELISA with spherical deflectors can be explained by small acceptance  $A_{\text{sph}} \approx 6\pi$  mm · mrad, see Fig. 3, *b*.

**3.2. Equilibrium Beam Profile.** We compare measured equilibrium profile of an 18.4 keV  $\text{Mg}^+$  beam in ELISA ring with deflectors of spherical shape to BETACOOOL simulations made under the assumption that the transverse beam size is mainly defined by losses on elements of the ring structure, see Fig. 9. The simulated r.m.s. width  $\sigma = 1.5$  mm corresponds to a ring acceptance of  $A \sim 6\pi$  mm · mrad (Fig. 9, *a*). These results well agreed with ELISA experiments where beam profile with Full Width on Half Maximum (FWHM) = 3.43 mm was measured at location where the horizontal beta-function is equal to  $\beta_x = 3.5$  m (Fig. 9, *b*). The ring acceptance was then varied as an input parameter in BETACOOOL. Assuming a ring acceptance of  $\approx 50\pi$  mm · mrad, the r.m.s. beam size of  $\sigma \approx 3$  mm would result, i.e., twice as large as what was measured in the experiment (Fig. 9, *c*).

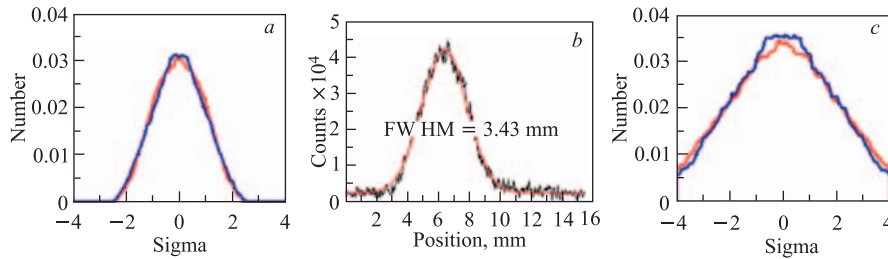


Fig. 9. Beam profile of 18.4 keV  $\text{Mg}^+$  ions in ELISA ring with spherical deflectors: *a*) BETACOOOL simulations correspond to the ring acceptance of  $A \sim 6\pi$  mm · mrad ( $\sigma = 1.5$  mm); *b*) experiment curve taken from [15] corresponds to the ring acceptance  $\sim 5\pi$  mm · mrad ( $\beta_x = 3.5$  m); *c*) expected beam profile assuming the ring acceptance would be  $\sim 50\pi$  mm · mrad

Beam size of  $\text{Mg}^+$  ions was measured as a function of time, and no increase in the width was seen over first  $\sim 0.3$  s of circulation [15]. We explain steady beam size in ELISA experiments by the fact that the initially high intensity  $\text{Mg}^+$  beam ( $N_0 = 2.7 \cdot 10^7$  ions) spreads out to the ring aperture due to small ring acceptance in  $\approx 200$  ms after injection (Fig. 10, *a*), and no further increase of beam emittance occurs but only beam losses on ring elements. In contrary, if the

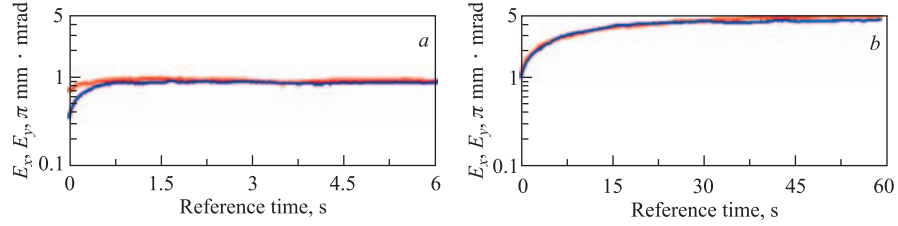


Fig. 10. Evolution of r.m.s. emittance in ELISA ring: *a*)  $\text{Mg}^+$  beam grows to the ring acceptance of  $A = 6 \pi \text{ mm} \cdot \text{mrad}$  in the first 0.5 s after injection; fast growth was measured in ELISA; *b*) assuming that the ring acceptance would be as large as  $A \sim 50 \pi \text{ mm} \cdot \text{mrad}$ , the emittance of  $\text{O}^-$  beam should grow steadily which contradicts to ELISA tests results

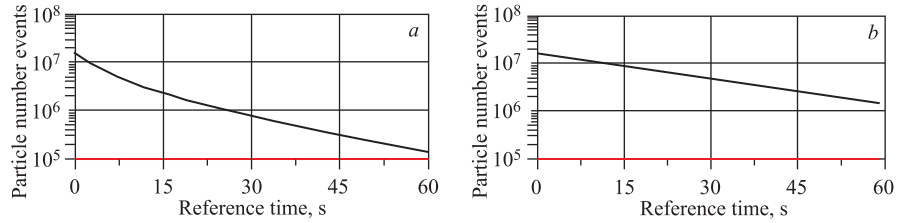


Fig. 11. BETACOOOL simulations of beam losses rate in ELISA ring: *a*) rate of intensity decay in the ring with acceptance  $A \sim 10 \pi \text{ mm} \cdot \text{mrad}$  corresponds to lifetime  $\tau = 12 \text{ s}$ ; *b*) assuming the ring acceptance is  $50 \pi \text{ mm} \cdot \text{mrad}$ , the lifetime would be  $\tau = 24 \text{ s}$ , which is twice as measured in experiment, see Fig. 3, *a*

ring acceptance would be as large as  $\sim 50 \pi \text{ mm} \cdot \text{mrad}$ , the beam emittance in ELISA should grow steadily at least 15 s during circulation of  $\text{O}^-$  ions in the ring (Fig. 10, *b*) which is not in agreement with experimental results.

We include all mentioned heating processes as well as experimentally defined lifetime of negative oxygen due to electron detachment into the BETACOOOL model. The lifetime of circulating in ELISA ring  $\text{O}^-$  beam estimated by counting the beam intensity decay rate is  $\tau_{1/2} \approx 12 \text{ s}$  (Fig. 11, *a*). If the acceptance would be as large as  $A \sim 50 \pi \text{ mm} \cdot \text{mrad}$ , the lifetime of the  $\text{O}^-$  beam should be at least 24 s (Fig. 11, *b*) which contradicts to a measured value of  $\tau_{1/2} \approx 12 \text{ s}$  (Fig. 3, *a*).

**3.3. Momentum Spread Growth.** Due to the fluctuations of ion energy loss on molecule of residual gas, i.e., energy straggling, the initial momentum spread of oxygen beam will increase few times until the equilibrium conditions will be reached. At initial low beam intensity ( $N_0 = 10^6$  ions) the r.m.s. momentum spread grows two times from  $10^{-3}$  to  $\sim 2 \cdot 10^{-3}$  (Fig. 12, *a*), while at high intensities ( $N_0 = 1.6 \cdot 10^7$  ions) the effect of intrabeam scattering in longitudinal phase space is more pronouncing and momentum spread grows four times to  $\sim 4 \cdot 10^{-3}$  (Fig. 12, *b*).

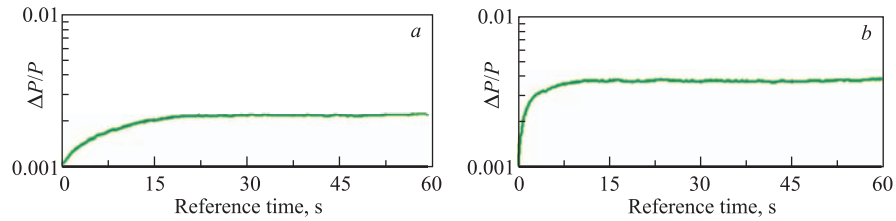


Fig. 12. Evolution of r.m.s. momentum spread of 22 keV  $O^-$  beam: *a*)  $10^6$  ions injected in the ring, equilibrium  $\Delta P/P \approx 2.2 \cdot 10^{-3}$  (r.m.s.); *b*)  $1.6 \cdot 10^7$  ions injected in the ring, equilibrium momentum spread is  $\approx 4 \cdot 10^{-3}$  (r.m.s.). Growth rates are higher in the last case

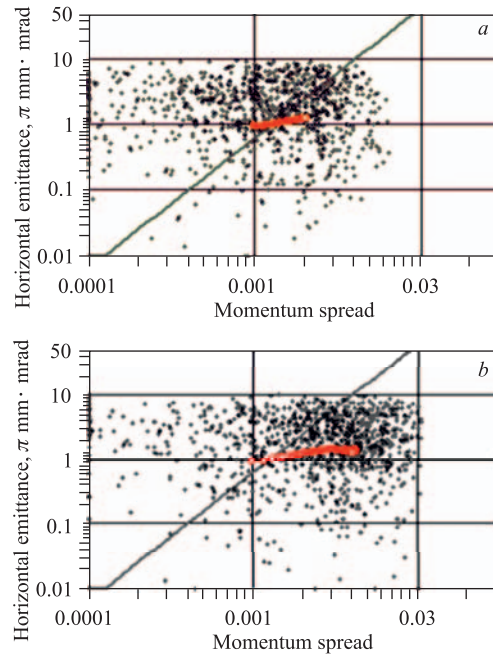


Fig. 13 (color online). ELISA ring. Distribution of 22 keV  $O^-$  beam in 3D phase space ( $\Delta P/P$ ,  $\epsilon_x$ ). Scattered points are particle invariants simulated in the frame of the Model Beam algorithm. Evolution of r.m.s. emittance and momentum spread in time is outlined by a red curve: *a*) low intensity beam ( $N_0 = 10^6$  ions), the beam distribution in energy is of Gaussian shape; *b*) high intensity beam ( $N_0 = 1.6 \cdot 10^7$  ions), the ions with high momentum spread are cut off by longitudinal ring acceptance

Distribution of 22 keV  $O^-$  ions beam in 3D phase space ( $\Delta P/P$ ,  $\epsilon_x$ ) is shown in Fig.13, where the beam emittance is plotted against the beam momentum spread. Scattered points are particle invariants simulated in the frame of the

Model Beam algorithm. Evolution of r.m.s. emittance and momentum spread in time is outlined by red curve. Ions are injected in the ring with initial emittance of  $\epsilon_x = 1 \pi \text{ mm} \cdot \text{mrad}$  (r.m.s.) and initial momentum spread of  $\Delta P/P = 10^{-3}$  (r.m.s.). We compare 3D phase space evolution at low and high initial beam intensities. Due to the high growth rate of transverse emittance, the beam reaches ring aperture in first few seconds even at low injected beam current. That is why the beam distribution in transverse direction is sharply cut off by the ring acceptance at  $A_x = 10 \pi \text{ mm} \cdot \text{mrad}$ .

Growth rate of momentum spread due to the fluctuation of energy losses depends on initial beam intensity. We determine special conditions which allow one to couple transverse motion invariant with longitudinal momentum spread of a coasting beam in the frame of the BETACOOOL Model Beam algorithm. The ion is considered to be lost as soon as the momentum spread will grow over the limit defined by the following expression:

$$\text{Inv}_{\text{long}} \langle D_x \rangle^2 > \text{Accept}_x \langle \beta_x \rangle. \quad (49)$$

Here  $\langle D_x \rangle$  and  $\langle \beta_x \rangle$  are average values of dispersion and horizontal betatron function over the ring circumference and  $\text{Accept}_x$  is a predefined value of the ring acceptance. The current value of the longitudinal motion invariant of coasting beam calculated for each model particle is a two times r.m.s. longitudinal emittance  $\epsilon_{\text{long}}^{\text{rms}}$ :

$$\text{Inv}_{\text{long}} = 2\epsilon_{\text{long}}^{\text{rms}} = 2 \left( \frac{\Delta p^{\text{rms}}}{p} \right)^2. \quad (50)$$

We applied these conditions to the circulating beam of  $\text{O}^-$  ions in the ELISA ring and found that the momentum spread distribution of low intensity ( $N_0 = 10^6$  ions) beam is less than the longitudinal ring acceptance. Thus, the beam distribution in momentum of small current beam is of Gaussian shape (Fig. 13, a).

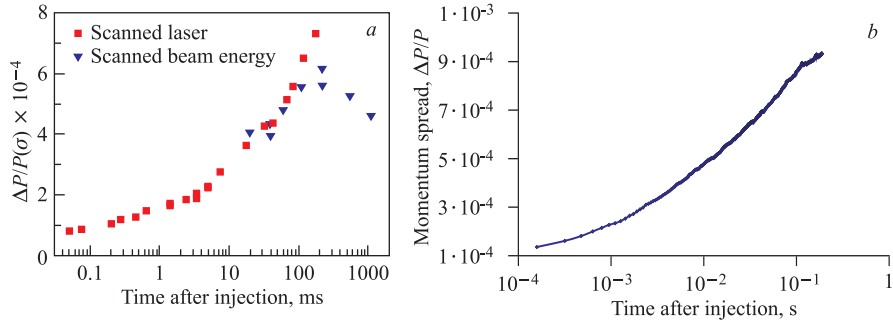


Fig. 14. Momentum spread of 18.4 keV/A  $\text{Mg}^+$  beam as a function of time. The initial beam intensity is  $2.7 \cdot 10^{+7}$  ions: a) experimental data taken from [15]; b) BETACOOOL simulations [37]. Due to intrabeam scattering, the r.m.s. momentum spread increases from around  $10^{-4}$  at injection up to  $7 \cdot 10^{-4}$  in about 150 ms

At high initial beam intensities, the IBS adds to the energy spread growth rate and momentum spread increases to the limit where the distribution is sharply cut off at  $\Delta P/P = 1\%$  (Fig. 13, *b*). Thus, we conclude that the acceptance of ELISA ring is about  $\Delta E/E = 2\%$  in energy spread units.

In addition, the fast growth of the momentum spread of a high intensity ( $2.7 \cdot 10^7$  ions), low energy (18.3 keV)  $\text{Mg}^+$  beam was reproduced. Blow up of r.m.s. momentum spread from around  $10^{-4}$  at injection up to  $7 \cdot 10^{-4}$  in about 150 ms after the beam injection has been measured in ELISA ring, see Fig. 14, *a* [15]. An excellent agreement of simulations with experimental results was achieved, see Fig. 14, *b* [37, 38]. It was shown that fast increase in momentum spread during first moment after beam injection is mainly caused by intrabeam scattering in longitudinal phase space. High intensity beam with a small initial momentum spread,  $\Delta P/P = 10^{-4}$  blows up immediately to  $\Delta P/P = 10^{-3}$ .

#### 4. OPERATION WITH INTERNAL TARGET

We studied kinetics of an ultralow energy antiprotons circulating in a small recycler storage ring and beam interaction with internal supersonic gas jet target [37]. Recycler ring made of electrostatic elements has been designed by the QUASAR Group [54] in close collaboration with the ASACUSA-MUSASHI collaboration (CERN) and experts from the Max Planck Institute for Nuclear Physics in Heidelberg [55].

The measurements of ionization cross sections in collisions between low-energy beams of antiprotons and different target gases, such as, for example, helium, directly address the few-body Coulomb problem and provide experimental data to aid in understanding of many-body interactions. Studying ionization by antiproton impact has advantage over electron and proton impact because competing processes, such as exchange and/or capture of bound electrons, are excluded during antiproton impact, while multiple scattering of antiprotons on nuclei of target atoms might be distinguished from ionization measurements by coincidence scheme of experimental setup of the reaction microscope [56].

In order to understand the ionization interaction processes, it is necessary to obtain fully differential cross sections in experiment where the momentum vectors of He ions and electrons from the ionization events by antiproton impact will be measured. So far, experimental studies of low-energy antiproton have been limited to the level of total cross sections due to the single-pass setup of the experiments and the very limited availability of high quality low-energy antiproton beams. The advantage of incorporating the reaction microscope into the ring over the single-pass experiment is that the antiproton beam can be recirculated and cross through the helium supersonic gas jet target for thousands if not millions times, thus increasing the count rate to enable low energy partial differential cross section measurements.

**4.1. Layout of Recycler Ring.** The energy range of ion circulating in the recycler ring was chosen between 3 and 30 keV but there are no technical constraints to operate recycler at lower energies down to  $\sim 1$  keV as well as at higher energies up to 100 keV. Ring lattice was specifically designed to provide sharp focus of beam in the centre of the reaction chamber marked as (R) in Fig. 15 [57]. The beam size at gas jet location should be reduced to a spot of 1–2 mm diameter and divergence angle less than 20 mrad.

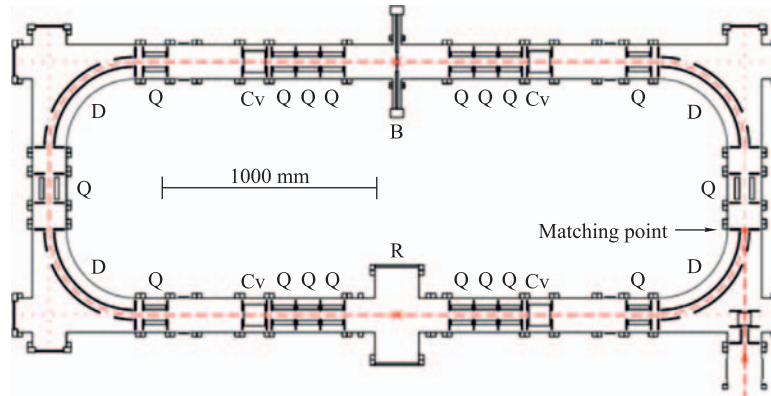


Fig. 15 (color online). Cross-sectional scale drawing of the recycler ring; horizontal cut including the mean path of the ion beam (dashed red line). Four  $90^\circ$  bending ES deflectors (D), four ESQ triplets (QQQ) and six ES single quads (Q) form ring lattice. Beam crosses gas jet in the reaction chamber (R)

Ring has periodicity of 2 and is composed of four  $90^\circ$  electrostatic bends with 400 mm radius of central orbit and 40 mm gap between electrodes, few sets of electrostatic quads and two 1.3 m long straight sections with  $\sim 0.5$  m available for an experiment. The simple racetrack lattice has been optimized for the conditions of multiple interactions between ions of circulating beam and atoms of He gas jet target at crossing point marked in Fig. 15 with a red  $\times$  [58]. The example of one cell lattice starting in the middle of long straight section is shown in Fig. 16. Across the top of the figure are shown the locations of the quadrupoles (blue vertical lines) and deflectors (red horizontal lines).

Two low- $\beta$  inserts located in the straight sections should reduce the beta-functions in the interaction region to  $b_{x,y} \leq 10$  cm. Each focusing unit is comprised of two sets of electrostatic quadrupole triplets. These are located as close as possible to each other in order to provide a sharp focus in the middle of the straight section where the reaction microscope will be installed. The two quadrupoles between the  $90^\circ$  deflectors are used to adjust the dispersion function at target location to achromatic conditions  $D = D' = 0$ . Combination of low-beta mode and achromatic conditions allows one to minimize emittance growth rate due to interaction with target, see Eq. (23), as well as to focus the beam to a small

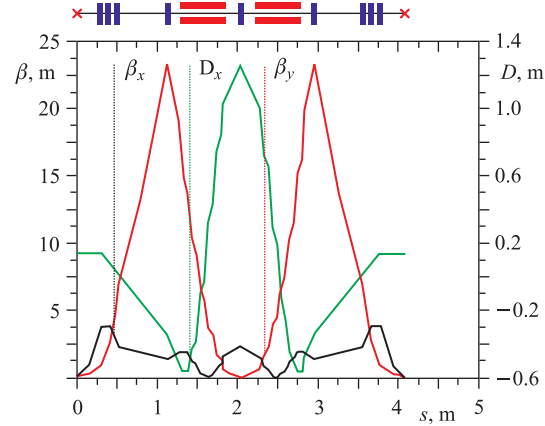


Fig. 16 (color online). Example of beta-functions and dispersion for the recycler ring (MAD-X simulations). One cell starting in the middle of long straight section is shown. In the interaction points the low-beta mode is realized ( $\beta_{x,y} \lesssim 10$  cm), also dispersion is varied to the achromatic conditions ( $D = D' = 0$ )

beam spot and to increase count rate of ionizations events by operation with high density, up to  $n_{\text{targ}} = 10^{12} \text{ cm}^{-3}$ , gas jet target.

**4.2. Growth of Beam Emittance in the Presence of the Target.** The long term beam dynamics in the recycler ring in the presence of He gas jet internal target was studied with the BETACOOOL code [25]. In addition to the multiple scattering of circulating antiproton ions on the nuclei of residual gas atoms, to the IBS and beam losses on the ring aperture, the small-angle multiple scattering of ions on the nuclei of the helium gas jet target was added. Also effects of mean energy losses and fluctuations of energy loss due to excitation and ionization of electron shell of He atoms by incident beam were included [41].

The feasibility of combined ring + target operation has been checked at 3 and 30 keV beam energies. We compare ring performance at different initial conditions: low ( $N_0 = 5 \cdot 10^5$ ) and high ( $N_0 = 10^7$ ) beam intensities, different r.m.s. emittance ( $1\pi$  and  $2\pi$  mm · mrad) and different r.m.s. momentum spread ( $10^{-3}$  and  $10^{-4}$ ) of injected ions. Table 3 gives a summary of the ring, beam and target parameters as well as results of numerical experiments.

As in the ELISA studies, we assume that due to the multiple scattering of ions on nuclei of residual gas and internal target as well as due to the intrabeam scattering at high beam intensities, the beam of ultralow energy antiprotons is spread out and lost on the ring aperture because of limited recycler ring acceptance estimated as  $A_{x,z} = 15\pi$  mm · mrad [55]. We compare contribution of gas jet to the multiple scattering, an ionization losses of beam to those from the IBS and residual gas.

Table 3. Summary of recycler ring parameters

Ring circumference, m	8.165			
Betatron tunes $\nu_x/\nu_y$	3.315/1.76			
Length of straight section/available for experiments, mm	1300/466			
Ring acceptance, $\pi$ mm · mrad	$15 \pi$			
Vacuum pressure (hydrogen), Torr	$10^{-11}$			
Horizontal/vertical beta functions at target $\beta_x/\beta_y$ , m	0.1/0.1			
Dispersion and derivative of dispersion at target, m	$D = D' = 0$			
Full size of beam spot at target location, $X \times Y$ , mm	$2 \times 2$			
Processes included in simulations	Rest gas + gas jet target + IBS + acceptance			
IBS models	Martini and Bjorken–Mtingwa Gaussian			
Helium target diameter, mm	1			
Helium target density $n_{\text{targ}}$ , $\text{cm}^{-3}$	$5 \cdot 10^{11}$			
Equilibrium momentum spread	$\sim 8 \cdot 10^{-3}$			
Antiproton energy, keV	3	30		
Initial r.m.s. emittance, $\pi$ mm · mrad ( $1\sigma$ emittance)	2	1		
Initial r.m.s. momentum spread, $\Delta P/P$	$10^{-3}$	$10^{-4}$		
Rotation period of antiprotons in the ring, $\mu\text{s}$	10.7	3.4		
Ionization cross section of He atoms by antiprotons, $\text{cm}^2$ [59]	$2 \cdot 10^{-17}$	$5 \cdot 10^{-17}$		
Beam lifetime $\tau$ , s ( $N = N_0 \exp(-t/\tau)$ , target OFF)	1.5	15		
Beam lifetime $\tau$ , s ( $N = N_0 \exp(-t/\tau)$ , target ON)	0.15	1.8		
Initial intensity of injected ions $N_0$	$5 \cdot 10^5$	$10^7$	$5 \cdot 10^5$	$10^7$
Time to achieve 90% of all ionization events, s	0.3	0.2	3	2
Integral of ionization events	$3.9 \cdot 10^3$	$2.5 \cdot 10^4$	$3.8 \cdot 10^5$	$3.6 \cdot 10^6$
Average rate of events per one turn in the ring	$\sim 0.12$	$\sim 1$	$\sim 0.4$	$\sim 5$
Growth rate of r.m.s. emittance $\frac{1}{\tau_{h,v}} = \frac{\delta\epsilon_{h,v}}{\epsilon_{h,v} T_{\text{rev}}}$ , $\text{s}^{-1}$ (target OFF/ON)	5/11	94/100	18/0.47 $\epsilon_{\text{in}}^{\text{rms}} = 2\pi$	3/3.3 $\epsilon_{\text{in}}^{\text{rms}} = 2\pi$
Growth rate of momentum spread $\frac{1}{\tau_l} = \frac{2\delta(\Delta p/p)}{(\delta p/p) T_{\text{rev}}}$ , $\text{s}^{-1}$ (target OFF/ON)	26/56	525/555	0.83/1.8 $\left(\frac{\Delta p}{p}\right)_{\text{in}}^{\text{rms}} = 10^{-3}$	17/17.6 $\left(\frac{\Delta p}{p}\right)_{\text{in}}^{\text{rms}} = 10^{-3}$

Evolution of beam emittance (r.m.s.) at the lowest beam energy of 3 keV is shown in Fig. 17, *a*, at upper energy of 30 keV — in Fig. 17, *b*. Here curves marked by label 1 are related to the ring operation at low initial beam intensity ( $N_0 = 5 \cdot 10^5$  ions) when target is switched OFF, by label 2 — at high initial intensity ( $N_0 = 1 \cdot 10^7$  ions) when target is switched OFF, by label 3 — at low

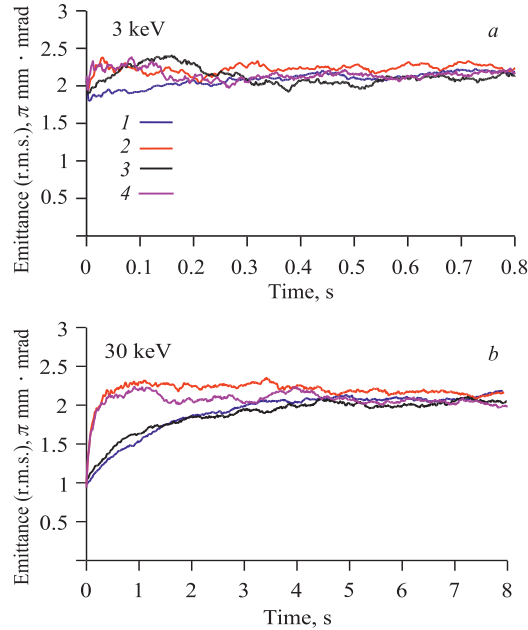


Fig. 17. Evolution of r.m.s. emittance of ions circulating in recycler ring. Target density is  $n_{\text{targ}} = 5 \cdot 10^{11} \text{ cm}^{-3}$ : *a*) ion energy is 3 keV; *b*) ion energy is 30 keV. Curves correspond to 1 — low beam intensity, target is OFF; 2 — high beam intensity, target is OFF; 3 — low beam intensity, target is ON; 4 — high beam intensity, target is ON

initial intensity when target is switched ON and by label 4 — at high initial intensity when target is switched ON.

It is expected that initial emittance of 3 keV beam might be of the order of  $\epsilon_{x,y} = 2 \pi \text{ mm} \cdot \text{mrad}$  (r.m.s.), see Fig. 17, *a*. Rates of emittance growth, see formula (12), are proportional to the square of speed of beam size increase and quite different at low and high beam intensities, at lowest and upper energies (Table 3). Beam emittance is growing at high beam intensity almost 20 times faster than at low ion current. Nevertheless, in the considered energy range the beam size is limited by the recycler ring acceptance regardless of ions energy, initial emittance or intensity of injected beam. At the lowest ion energy, the initial beam emittance already closes to the limit of the recycler ring acceptance and ions reach ring aperture in  $\sim 10$  to  $50$  ms depending in initial beam intensity. Then beam r.m.s. emittance only fluctuates slightly around fixed value defined by the ring acceptance. That is why all curves in Fig. 17, *a* are almost overlapped with each other. The average value of r.m.s. emittance  $\epsilon_x \approx 2.2 \pi \text{ mm} \cdot \text{mrad}$  in this figure corresponds to the recycler ring acceptance of  $A_{x,z} = 15 \pi \text{ mm} \cdot \text{mrad}$ .

At 30 keV ion energy the initial beam emittance is less than at 3 keV, and we choose in our studies the value of  $\epsilon_{x,y} = 1 \pi \text{ mm} \cdot \text{mrad}$  (r.m.s.), see Fig. 17, *b*. The r.m.s. emittance of 30 keV high intensity beam ( $N_0 = 10^7$  ions) grows to the ring acceptance in  $\sim 0.2$  s because of high IBS growth rate, see curves 2 and 4 in Fig. 17, *b*. At low beam intensity, beam size of 30 keV ions will grow to the ring acceptance in  $\sim 3$  s, see curves 1 and 3 in Fig. 17, *b*. Beam emittance at upper ion energy is also limited by ring aperture. That is why in the considered ultralow energy range, the steady beam size at target location is the same regardless of initial beam energy, regardless of initial beam emittance, etc.

Despite essentially different growth rates at low and high ion currents, at the lowest (3 keV) and upper (30 keV) beam energies, the steady beam spot at target is defined by the ring acceptance and by the value of the betatron functions  $\beta_y^{\text{targ}}$  at reaction microscope location. Providing the achromatic conditions  $D = D' = 0$

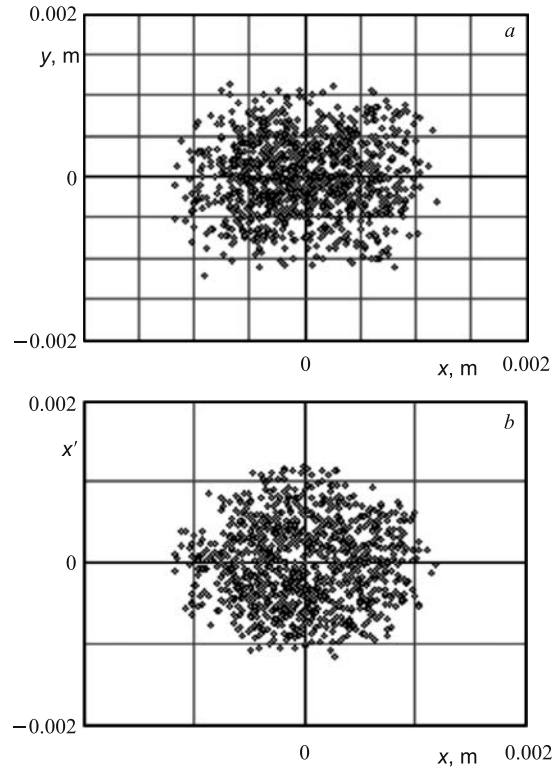


Fig. 18. Antiproton beam interaction with the helium target: *a*) diameter of beam spot at target location might be reduced to 2 mm; *b*) area in the phase space occupied by beam corresponds to recycler acceptance of  $A_x = 15 \pi \text{ mm} \cdot \text{mrad}$

are applied in long straight sections of the recycler ring, the beam half-size at target might be estimated by the following formula:

$$y = \sqrt{\beta_y^{\text{targ}} \cdot A_y}. \quad (51)$$

With low- $\beta$  achromatic lattice and rather small ring acceptance, the beam spot at target might be reduced to 2 mm diameter, see Fig. 18, *a*. In a focus point the angular divergence of ions is less than 10 mrad, i.e., two times less than upper limit imposed by conditions of experiment, see Fig. 18, *b*. Beam shape at target location might be adjusted by variation of horizontal and vertical betatron functions using different settings of low- $\beta$  inserts. Nevertheless, due to nonlinear astigmatic aberrations it would be difficult to reduce beam size further down. The detailed analysis of nonlinear aberrations requires additional studies and it is out of scope of this paper. Combination of decreased ring acceptance (beam collimation) and ultralow betatron functions  $\beta_y^{\text{targ}} < 5$  cm in reaction microscope location might help one to reduce beam spot at target to less than 2 mm but in expense of increased rate of ion losses and distorted beam spot. Growth of intrabeam scattering in the ring sections, where betatron functions are minimum and beam density is maximum, will lead to the reduced lifetime and decreased luminosity of experiment.

**4.3. Energy Losses due to Interaction of Ions with Gas Jet Atoms.** Growth of the beam momentum spread in the recycler ring is caused by fluctuations of ionization and/or excitation energy losses during interaction of ions with electron shells of residual gas atoms as well as with electron shells of internal gas jet target atoms. Evolution of r.m.s. momentum spread at the lowest beam energy of 3 keV is shown in Fig. 19, *a*, at upper energy of 30 keV — in Fig. 19, *b*. Here curves marked by label *1* are related to the ring operation at low initial beam intensity ( $N_0 = 5 \cdot 10^5$  ions) when target is switched OFF, by label 2 — at high

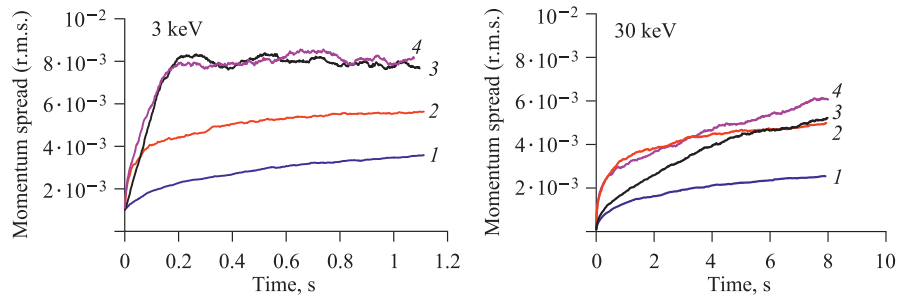


Fig. 19. Evolution of r.m.s. momentum spread of ions circulating in recycler ring. Target density is  $n_{\text{targ}} = 5 \cdot 10^{11} \text{ cm}^{-3}$ : *a*) ion energy is 3 keV; *b*) ion energy is 30 keV. Curves correspond to 1 — low beam intensity, target is OFF; 2 — high beam intensity, target is OFF; 3 — low beam intensity, target is ON; 4 — high beam intensity, target is ON

initial intensity ( $N_0 = 1 \cdot 10^7$  ions) when target is switched OFF, by label 3 — at low initial intensity when target is switched ON and by label 4 — at high initial intensity when target is switched ON.

When target is switched OFF, the momentum spread of 3 keV beam circulating in the ring will steadily grow from initial  $\Delta P/P = 10^{-3}$  (r.m.s.). Growth rates of high intensity beam almost 20 times exceed those of low intensity ions, see Table 3. After 1 s of ion circulation in the ring, the momentum spread will reach level of  $\Delta P/P = 3.5 \cdot 10^{-3}$  (r.m.s.) at low beam current (curve 1 in Fig. 19, *a*) and it is slightly more at high beam current (curve 2 in this figure). When target is switched ON, additional fluctuations of energy losses will increase momentum spread at high as well as at low initial beam intensities approximately to the level of ring acceptance in longitudinal phase-space, see curves 3 and 4 in Fig. 19, *a*. The limit of maximum allowable energy spread was defined by formulae (49) and (50) and it corresponds to a level of  $(\Delta P/P) \approx 8 \cdot 10^{-3}$  (r.m.s.). High speed of momentum spread growth in the beginning of cycle ( $1/\tau_{\text{long}} \sim 500 \text{ s}^{-1}$ ) should be explained by strong IBS growth rate.

At 30 keV energy range, the momentum spread will steadily grow during observation time of 8 seconds (Fig. 19, *b*). In presence of high density target ( $n_{\text{targ}} = 5 \cdot 10^{11} \text{ cm}^{-3}$ ) the r.m.s. momentum spread of high intensity beam will reach value of  $\Delta P/P = 6 \cdot 10^{-3}$  (curve 4 in Fig. 19, *b*) which is still less than longitudinal ring acceptance.

We compare beam evolution in 3D phase space of 3 keV low intensity beam ( $5 \cdot 10^5$  ions) with initial momentum spread of  $\Delta P/P = 10^{-3}$  (r.m.s.) (Fig. 20, *a*) to 3D evolution of 30 keV high intensity ( $N_0 = 10^7$  ions) beam with initial momentum spread of  $\Delta P/P = 10^{-4}$  (r.m.s.) (Fig. 20, *b*). Growth rates of momentum spread are quite different at 3 and 30 keV. The equilibrium parameters of 3 keV beam are restricted by ring acceptance and are almost the same regardless of initial conditions. Distribution of r.m.s. emittance as well as distribution of r.m.s. momentum spread (scattered points of particle invariants simulated in the frame of the model beam algorithm) are sharply cut off at large values, see Fig. 20, *a*.

At 30 keV energy, the r.m.s. emittance also reaches ring acceptance and distribution of ions in transverse space phase is cut off at large values of emittance. The maximum value of beam momentum spread at 30 keV energy is slightly less than ring acceptance in longitudinal phase space and beam distribution is symmetric around r.m.s. value. Providing 30 keV ions will circulate in the ring over 20 s, the r.m.s. momentum spread will grow to the ring acceptance, and ion distribution will be sharply cut off similar to 3 keV energy ions.

Thus, we came to the conclusion that due to the combined effect of IBS, residual gas scattering and scattering of ultralow energy ions on the high density gas jet target, the antiproton beam reaches the transverse ring acceptance  $A_{x,y} = 15 \pi \text{ mm} \cdot \text{mrad}$  as well as longitudinal ring acceptance  $\Delta P/P = \pm 1.5 \cdot 10^{-2}$ .

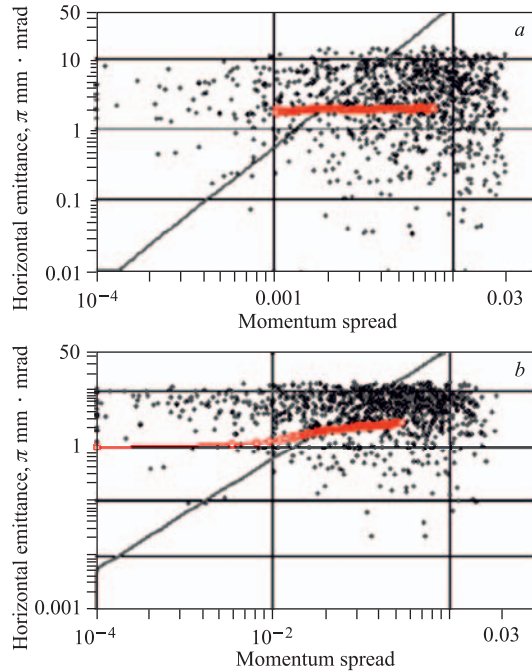


Fig. 20 (color online). Beam evolution in 3D phase space in the presence of target: *a*) 3 keV low intensity ( $N_0 = 5 \cdot 10^5$  ions) beam. Initial emittance and momentum spread are  $\epsilon_x = 2\pi$  mm · mrad (r.m.s.) and  $\Delta P/P = 10^{-3}$  (r.m.s.); *b*) 30 keV high intensity ( $N_0 = 10^7$  ions) beam. Initial emittance and momentum spread are  $\epsilon_x = 1\pi$  mm · mrad (r.m.s.) and  $\Delta P/P = 10^{-4}$  (r.m.s.). While growth rates are essentially different, the beam emittance is restricted by ring acceptance regardless of initial conditions

The lowest ion energy momentum spread of beam with initially low  $\Delta P/P = 10^{-4}$  will grow to the level of  $10^{-3}$  in less than 30 ms because of the high growth rate of intrabeam scattering at high intensities, see the first points of red curve in Fig. 20, *b*. Our simulations are in good agreement with experimental and computing results on fast momentum spread growth of 18.4 keV/A  $\text{Mg}^+$  beam in ELISA ring, see Fig. 14.

We simulated mean energy losses of antiproton beam due to the excitation and ionization of atomic electrons of gas jet target in accordance with Bethe–Bloch Eq. (28). Mean energy loss of high intensity ( $N_0 = 10^7$  ions) antiproton beam interacting with He target of  $n_{\text{targ}} = 5 \cdot 10^{11}$  cm $^{-3}$  density is shown in Fig. 21. Antiproton ions injected into the ring at 3 keV might loose almost 1.6% of initial beam energy in the first 200 ms of interaction with the internal target, see Fig. 21, *a*. At 30 keV, the rate of mean energy losses is few times

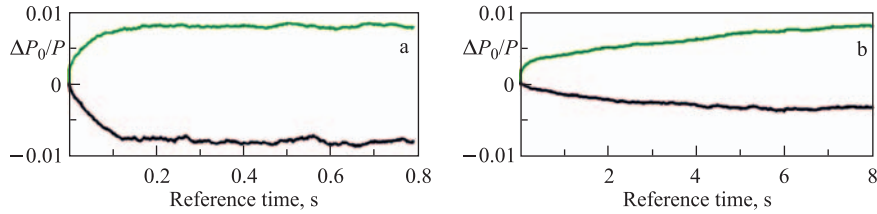


Fig. 21. *a)* Ion kinetic energy of 3 keV, energy shift  $\Delta T/T = -1.6 \cdot 10^{-2}$ ; *b)* ion kinetic energy of 30 keV, energy shift  $\Delta T/T = -6 \cdot 10^{-3}$

less and beam energy will be reduced to 0.6% of initial value in the first  $\sim 4$  s (Fig. 21, *b*). Due to the lack of experimental data at ultralow energies, more detailed studies of energy losses are required. In our simulations we assume the ratio between ionization and excitation events to be similar to the case of interaction between high energy ions and target atoms. Meanwhile, at 3 keV energy range more than 99.7% of ions will be lost, due to the multiple scattering on target nuclei, and only 0.2% of incident beam will ionize He atoms. Thus, in our model the mean energy losses at 3 keV should be counted by excitation of electron shell of He atoms rather than by ionization. So far, experimental data are more preferable. At 30 keV energy range, results of simulations are more consistent with experimental ionization cross-sections data.

Even though the position of reduced energy beam will not be shifted from the target because of application of the achromatic conditions in long straight sections of the recycler ring, the energy losses should be compensated by small drift tube RF system or by other means.

**4.4. Rate of Ionization Events in the Recycler Ring.** The beam intensity losses, lifetime, useful ionization events due to antiproton impact with He atoms have been calculated for different target densities, for low and high intensity beam, at the lowest and highest energy of experiment, see Table 3. Experimental data on ionization cross section of He atoms by antiproton impact at different projectile energies, kindly presented by H. Knudsen [59], were used for estimation of useful events amount in recirculator reaction microscope where the momentum vectors of the He ions and electrons are measured (Fig. 22). For the sake of experimental data, it was assumed that every ionization event will lead to the loss of an antiproton. This assumption is not evident since the maximum transferable energy, see Eq. (30), is less than  $2 \cdot 10^{-3}$  of beam kinetic energy and thus lower than the longitudinal ring acceptance. If circulating ions will not be kicked off during ionization of He atoms and may continue to circulate in the ring after the impact and can produce more than one ionization event, the count rate and integral of useful events will be higher than we are expecting.

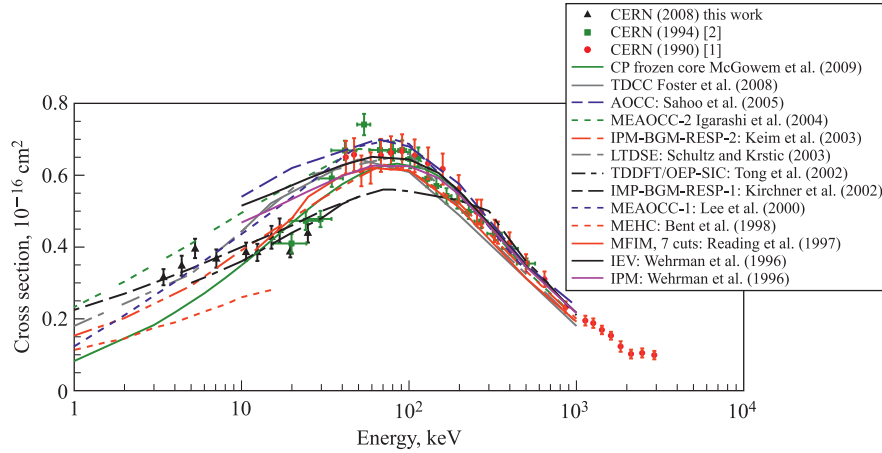


Fig. 22. Experimental data on ionization cross section of He atoms by antiproton impact taken from [59]

At low beam intensity ( $N_0 = 5 \cdot 10^5$  ions) the average count rate in the ring is essentially less than one event per ring revolution even at high target density of  $n_{\text{targ}} = 5 \cdot 10^{11} \text{ cm}^{-3}$ , see Table 3. Such a low rate might not be favorable for operation of reaction microscope.

Decay of high intensity beam and integral of ionization events during multiple crossing of antiprotons with helium gas jet are shown in Fig. 23. When internal target is switched off, the lifetime of 3 keV beam circulating in recycler ring is limited to 1.5 s because of the intrabeam scattering at the beginning of cycle and multiple scattering on residual gas, see curve 1 in Fig. 23, *a*.

High multiple scattering rate of ultralow energy ions on atoms of dense He gas jet target ( $n_{\text{targ}} = 5 \cdot 10^{11} \text{ cm}^{-3}$ ) will add to combined effect of multiple scattering of antiprotons on atoms of residual gas and of IBS. As a result, the lifetime will be further reduced to 150 ms, see curve 3 in Fig. 23, *a*.

In total, over  $2.5 \cdot 10^4$  ionization events can be detected during the first 200 ms of 3 keV beam circulation in the ring (curve 2 in Fig. 23, *a*). Thereby, more than 99.7% of ions will be lost on the ring aperture before to ionize He atoms. At 3 keV energy, ions will rotate in the ring a little bit more than 20,000 turns before to be lost and average count rate should be  $\sim 1.2$  ionization events per one revolution. This rate is reasonable for measurements of differential cross sections in experiments with reaction microscope.

The beam lifetime of 30 keV antiprotons circulating in the ring without target is about 15 s because of the multiple scattering on atoms of residual gas and high IBS growth rate at the beginning of cycle when initial beam intensity is high, see

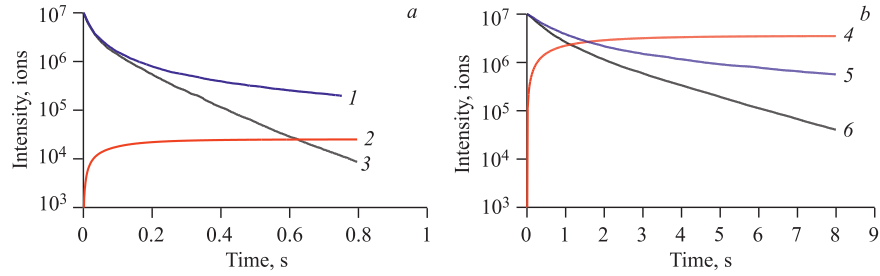


Fig. 23 (color online). Beam decay (blue and black curves) and integral of ionization events (red curve) in the recycler ring. Initial intensity is  $N_0 = 10^7$  ions, density of helium gas jet target is  $n_{\text{targ}} = 5 \cdot 10^{11} \text{ cm}^{-3}$ : a) energy of projectile ions is 3 keV. 1 — beam current versus time when target is switched OFF, lifetime is  $\tau_{1/2} \sim 1.5$  s; 2 — integral of ionization events; 3 — beam decay in the presence of target, the lifetime is reduced to  $\tau_{1/2} \sim 0.15$  s due to multiple scattering of ions on atoms of internal gas jet; b) energy of projectile ions is 30 keV. 4 — beam intensity as a function of time when target is switched OFF, lifetime is  $\tau_{1/2} \sim 15$  s; 5 — integral of ionization events; 6 — beam intensity in the presence of target, the lifetime is  $\tau_{1/2} \sim 1.8$  s providing each ionization event leads to the loss of incident ion

curve 2 in Fig. 23, b. In the case of multiple crossing of 30 keV high intensity antiproton beam with helium gas jet target ( $n_{\text{targ}} = 5 \cdot 10^{11} \text{ cm}^{-3}$ ), up to  $3.6 \cdot 10^6$  ionization events might be detected in the first 2 s of ion circulation in the ring, see curve 1 in Fig. 23, b. In our «experiment» we assume that each ionization event during interaction of projectile particles with atoms of internal gas jet target will lead to the ion loss. Thus, at 30 keV energy range, beam lifetime in the presence of target is reduced from  $\tau_{1/2} = 15$  s to  $\tau_{1/2} = 1.8$  s, i.e., almost 8 times, because of the multiple scattering on target and reducing of beam intensity due to ionization events, see curve 3 in Fig. 23, b.

Average count rate of such an experiment at 30 keV is about 5 ionization events per one turn. Thus, one may expect to accumulate the same integral of ionization events even at reduced gas jet density when count rate is less but gas load from the target is reduced and conditions for the experiment are more relaxing.

## 5. SIMULATIONS OF BEAM SHRINKING IN THE TSR EXPERIMENT WITH SLOW IONS

Experiments with electron cooling of slow ions provide important information on possible performance and limitations at ultralow energy range and are of crucial importance for future generation facilities like Cryogenic Storage Ring (CSR) at MPI [60], Facility for Low Energy Antiproton and Ion Research (FLAIR) at GSI [61, 62], etc.

Cold electron beams at the energy range of 150 eV down to 10 eV and possibly less are key elements of next generation electrostatic storage rings where electron cooling of ultralow energy ions and high resolution electron–ion [60] or positron–antihydrogen ions merged experiments will be performed [62]. Electron beams with low emission energy spread are required in order to reduce longitudinal temperature and thus increase the friction force of electron cooling.

**5.1. Application of Photocathode Gun for the Electron Cooling of Low Energy Ions.** Experiments with electron cooling of  $\text{CF}^+$  ions ( $A = 31$ ) at the Test Storage Ring (TSR) [63] of the Max Planck Institute for Nuclear Physics in Heidelberg (Germany) were reported [64]. Low intensity beam of 93 keV/A  $\text{CF}^+$  ions has been shrunk to ultrasmall beam size using a cold beam of 53 eV electrons produced by cryogenically cooled GaAs photocathode.

The few 100 pA current of  $\text{CF}^+$  ions has been injected into the TSR ring with initial emittance of  $\varepsilon_{x,y}^{\text{in}} \approx 1 \pi \text{ mm} \cdot \text{mrad}$  and initial momentum spread of  $(\Delta P/P)_{\text{in}} = 2 \cdot 10^{-4}$ . The TSR electron target setup was converted into the electron cooling device [65]. The cooling time less than  $\tau_{\text{cool}} < 2 \text{ s}$  and the equilibrium beam size of about  $0.2 \times 0.04 \text{ mm}$  (r.m.s.) after  $\sim 6 \text{ s}$  of cooler operation have been measured, see Fig. 24 taken from [64]. Assuming the upright orientation of phase space ellipse in the middle of the ring straight section where the e-target is located and subtracting 0.1 mm dispersion term from the total 0.2 mm radial width of the beam, one may estimate the equilibrium emittance of cooled ions as  $\varepsilon_{x,y}^{\text{eq}} \sim (1-2) \cdot 10^{-3} \pi \text{ mm} \cdot \text{mrad}$  (r.m.s.).

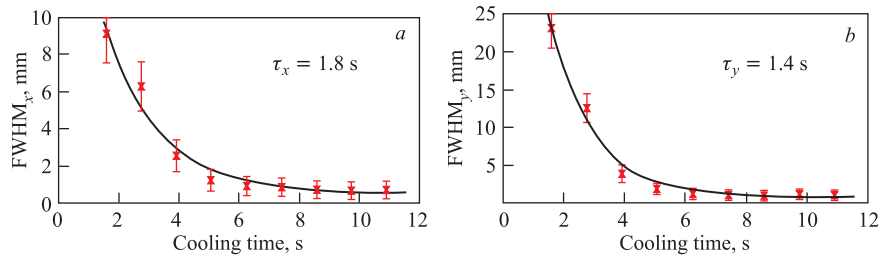


Fig. 24. Shrinking of the beam size in the TSR experiment on the transverse electron cooling of 93 keV/A  $\text{CF}^+$  ions: *a*) equilibrium r.m.s. beam width in horizontal plane is  $\sigma_x = 0.2 \text{ mm}$ ; *b*) equilibrium r.m.s beam width in vertical plane is  $\sigma_y = 0.04 \text{ mm}$

The so-called «hot» ions with injected beam diameter twice as much as diameter of the electron beam have been cooled in  $\sim 6 \text{ s}$ . The detector measurements have indicated extremely low divergence angle of cooled ions at about  $3 \cdot 10^{-2} \text{ mrad}$  and small momentum spread  $(\Delta P/P)_{\text{eq}} = 5 \cdot 10^{-5}$ .

In the TSR electron target, the atomically clean  $p^+$ -GaAs photocathode with a thin layer of cesium and oxygen is cryogenically cooled down to 90 K and emits up to 1 mA of electrons with reduced energy spread of about 7 meV [65]

which is 15 times less with respect to the energy spread of the thermocathode used in standard electron guns of cooler systems [66].

The ultracold electron beam has been obtained in the TSR experiment by adiabatic expansion of cold photoelectrons in guiding magnetic field of the cooler. The transverse and longitudinal temperatures of photoelectrons in the gun were estimated as  $kT_{\perp} = 0.5$  meV and  $kT_{\parallel} = 0.03$  meV, respectively.

The main limitations of photocathode such as degradation of emission efficiency with time have been overcome in the TSR electron target and lifetime of the electron gun exceeds 24 h. Also photocathodes emit small electron beam current with respect to commonly used thermocathodes. But at ultralow energy range, the thermocathode performance is limited by the gun perveance and available electron current at 50 eV beam energy is of the order of  $I_e = 400\text{--}700$   $\mu\text{A}$ . Emitted current from thermoelectron gun at 10 eV might not exceed  $I_e = 30\text{--}60$   $\mu\text{A}$  [64]. Moreover, the space charge effects in electron beam limit optimum electron beam current to the level available at photo-guns. Thus, the photocathode performance itself and emitted electron current are satisfactory at low electron energies and should be close to thermoelectron guns operation conditions.

**5.2. The Ion Kinetics with Electron Cooling.** The BETACOOOL code has been benchmarked against TSR operation with ultralow energy  $\text{CF}^+$  ions, and results of TSR experiments have been reproduced. We studied long term beam dynamics and ion kinetics during beam circulation in the TSR storage ring. The electron cooling has been added to the heating processes such as small-angle multiple scattering of the circulating ions on the residual gas atoms and molecules, IntraBeam Scattering (IBS) and ionization energy losses. Recombination was taken into account by reducing the  $\text{CF}^+$  ions lifetime to 4 s as was reported by the authors [64]. Competing cooling and heating processes, ratio between cooling and growth rates of beam emittance and momentum spread, beam intensity change as well as equilibrium conditions have been investigated by simulations of r.m.s. parameters of the evolution of the ion distribution function over the time.

The theory of electron cooling is well developed and detailed information might be found at [67–69]. In our studies, the thin lens approximation of the electron cooler was chosen because the variation of the friction force as well as particle momentum change along 1.2 m long cooling section are small. The simplified model also presumes that the ion displacement from the ring axis does not change during motion inside the cooler. Thus, one may describe the action of e-cooler on the beam by changing the transverse component of ion momentum, i.e., angle variation  $\Delta\theta$  after traversal of cooling section

$$\Delta\theta = \frac{F}{Mc^2\beta^2\gamma}l_{\text{cool}}, \quad (52)$$

where  $l_{\text{cool}}$  is the length of the cooler;  $\beta$ ,  $\gamma$  are relativistic parameters, and  $F_{\text{fr}}$  is the friction force. The friction force is determined by Coulomb collisions of ions

with electrons and for extremely cold electron beam might be expressed by the formula [68]

$$F = -\frac{dE_i}{ds} = -\frac{4\pi Z^2 n_e e^4}{mV^2} \ln \frac{\rho_{\max}}{\rho_{\min}}. \quad (53)$$

Here  $n_e$  is the electron density and  $V$  is the ion speed relative to electrons in the moving coordinate system. Ion velocity  $V(\rho)$  is a function of the impact parameter  $\rho$ . The minimum impact parameter  $\rho_{\min}$  of collision approximately corresponds to the electron scattering by  $\pi/2$  angle. The maximum impact parameter  $\rho_{\max}$  is related to distance between particles when effective interaction is still possible.

Few models describe friction force when electrons are distributed over velocities, and numerical integration of product of natural logarithm of impact parameters ratio  $\ln(\rho_{\max}/\rho_{\min})$  over electron density distribution function  $f(n_e)$  should be taken. For the magnetized electron beam, the semiempirical formula of the friction force proposed by V. V. Parkhomchuk [69] provides the best fit to experimental data and we choose it for our studies

$$\mathbf{F} = -\mathbf{V} \frac{4Z^2 e^4 n_e L_p}{m} \frac{1}{\left(V^2 + \Delta_{e,\text{eff}}^2\right)^{3/2}}. \quad (54)$$

Here  $\Delta_{e,\text{eff}}$  is the effective velocity spread of electron beam which depends on cathode temperature as well as on homogeneity of guiding magnetic field lines. The Coulomb logarithm  $L_p$  as a function of maximum  $\rho_{\max}$  and minimum  $\rho_{\min}$  impact parameters indirectly depends on effective velocity spread  $\Delta_{e,\text{eff}}$ , on the time-of-flight of ions inside of cooler section, and on electron plasma frequency. The model of electron gun of uniform cylinder shape with radius  $r_e$  and constant beam density  $n_e$  was used in our simulations

$$n_e = \frac{I_e}{e\pi a^2 \beta c}. \quad (55)$$

Also electron beams of Gaussian, parabolic as well as of any arbitrary shape, might be chosen in the BETACOOOL programme.

The space charge effect in the electron beam leads to the dependence of the mean electron velocity as well as electron velocity spread on position inside the electron beam and can be calculated for electron beam of uniform density distribution by analytic formulae. There are two general effects related to the space charge of electron beam:

1. Electron longitudinal momentum shift due to potential distribution inside the beam.
2. Drift motion of the electrons in the crossed guiding longitudinal magnetic field of the cooler solenoid and radial electric field of the electron beam.

The electron drift motion leads to the electron beam rotation with the drift velocity around its axis. Also the electron drift motion increases the transverse velocity spread and in the worst case additional transverse velocity spread is equal to the drift velocity value.

**5.3. Collapse of Beam Emittance at Low Beam Intensities.** In order to compare electron cooling experiments with computer simulations and benchmark the BETACOOOL code at ultralow energy range we use the same parameters as were reported in the TSR experiment, see Table 4. In the standard mode of operation, particles are accelerated in the 13 MV tandem or in the high current injector and both pre-accelerators are combined with LINAC post-accelerator. Accelerated ions are injected into the 5 m long straight section of the ring where four bump magnets are located. Particles with small emittance of about  $\varepsilon_{x,y}^{\text{in}} \approx 1.5 \pi \text{ mm} \cdot \text{mrad}$  and low momentum spread of  $(\Delta P/P)_{\text{in}} = 2 \cdot 10^{-4}$  are accumulated in the ring using multiturn injection technique [70]. The large acceptance of TSR allows one to accumulate up to 40 turns of injected beam in one batch of ions with total emittance of about  $60 \pi \text{ mm} \cdot \text{mrad}$ . Then the RF cavity captures the beam into the RF bucket and frequency of RF cavity is reduced slightly. Stacked batch of beam with 2% reduced ion energy moves towards internal orbit because the dispersion equals  $D = 2 \text{ m}$  in the injection section. The space in the injection section is free for the next cycle. Up to 25 RF stacking cycles might be applied to accumulate single batches into stacked beam. Combined cycles of multiturn injection and RF stacking allow one to increase beam intensity almost 1000 times from  $10^7$  to  $10^{10}$  ions. The momentum spread of final stacked beam might be as large as  $(\Delta P/P)_{\text{fin}} = 2 \cdot 10^{-2}$ .

Then the stacked beam is cooled down to equilibrium conditions by using the standard electron cooling system with thermocathode [71]. In the process of electron cooling, the emittance of accumulated beam is reduced  $\sim 100$  times. Also momentum spread drops from  $\Delta P/P = 2 \cdot 10^{-2}$  to  $2 \cdot 10^{-4}$ . The  $10^6$  fold reduction of 3D phase space was achieved in the TSR experiments on the electron cooling of intense ion beams [63].

In the TSR experiment with photo-electron cooling of low energy  $\text{CF}^+$  ions, the single turn injection of low intensity beam has been employed rather than combination of multiturn injection with RF stacking. Thus, the initial parameters of injected  $\text{CF}^+$  beam, i.e., emittance  $\varepsilon_{x,y}^{\text{in}} = 1 \pi \text{ mm} \cdot \text{mrad}$  (r.m.s.), momentum spread  $(\Delta P/P)_{\text{in}} = 2 \cdot 10^{-4}$  (r.m.s.), and beam intensity of  $N_0 = 2 \cdot 10^4$  ions were chosen in our BETACOOOL studies on beam shrinking.

The parameters of standard TSR electron cooler are not optimized to reduce already small initial emittance of circulating beam of  $\text{CF}^+$  ions. In our simulations we use parameters of the TSR cryogenically cooled photocathode with transverse electron temperature of  $kT_{\perp} = 500 \mu\text{eV}$  and longitudinal electron temperature of  $kT_{\parallel} = 30 \mu\text{eV}$ , see Table 4.

**Table 4. Parameters of the TSR experiment and the USR operation mode with internal target**

Ring	TSR	USR
Ion	CF <sup>+</sup>	$\overline{P}$
$A/Z$	31 / 1	1 / -1
Ion energy, keV/A	97	300–20
Ring circumference, m	55.4	42.598
Horizontal/vertical betatron tunes	2.84/2.77	2.567/1.576
$\beta = v/c$	$1.4 \cdot 10^{-2}$	$2.5 \cdot 10^{-2}$ – $6.5 \cdot 10^{-3}$
Rotation period, $\mu$ s	13	5.6–21.8
Vacuum pressure (hydrogen), Torr	$10^{-11}$	$10^{-11}$
Injected beam intensity, ions	$\sim 2 \cdot 10^4$	$2 \cdot 10^7$
Ion lifetime, s	4	$> 10^6$
Initial/equilibrium emittance (r.m.s.), $\pi$ mm · mrad	$1/10^{-3}$	5/0.3
Equilibrium emittance low- $\beta$ mode (r.m.s.), $\pi$ mm · mrad	—	0.7–1
Initial/equilibrium	$2 \cdot 10^{-4}/5 \cdot 10^{-5}$	$10^{-3}/6 \cdot 10^{-4}$
Equilibrium momentum spread (r.m.s.) low- $\beta$ mode	—	$10^{-3}$
Ring acceptance, $\pi$ mm · mrad	120	100
Ring acceptance for low- $\beta$ mode, $\pi$ mm · mrad	40	30
Number of straight sections	4	4
Length of achromatic straight section, m	5.2	4
Periodicity: cooling mode	$2 \times 2$ (FP, -FP)	4 ( $D = D' = 0$ )
low- $\beta$ mode	—	2 ( $D = D' = 0$ )
Electron cooler		
Length of electron cooler, m	1.2 (e-target)	2
Electron beam energy, eV	53	162 –11
Magnetic field at cooler, kG	0.4	0.4 –0.1
Beta function at cooler (hor./vert.), m	4 / 1.5	7/7
Dispersion at cooler, m	2	$D = D' = 0$ achromat
Friction force model	Parkhomchuk	Parkhomchuk
Electron beam radius, mm	6.5	10
Electron beam current, mA	0.3	1–0.05
Adiabatic magnetic field expansion factor	20	20
Cryogenic photocathode temperature ( $kT_C$ ), meV	10	10
Electron temperature ( $kT_{\perp}/kT_{\parallel}$ ), meV	0.5/0.03	0.5/0.045 (162 eV) 0.5/0.03 (11 eV)
Thermocathode temperature ( $kT_C$ ), meV	—	100
Thermocathode electron temperature ( $kT_{\perp}/kT_{\parallel}$ ), meV	—	4 / 0.5
Gas jet target		
Helium jet target density, cm <sup>-3</sup>	—	$5 \cdot 10^{11}$
Target diameter, mm	—	1
Beta function at target (hor./vert.), m	—	0.1–0.5
Dispersion at target, m	—	$D = D' = 0$
Cross section of He atoms ionization, cm <sup>2</sup>	—	$5 \cdot 10^{-17}$
Integral of ionization events, counts	—	$\sim 10^7$

We plot «snap-shots» of circulating beam just after the injection into the ring but before to be cooled down. The initial beam emittance is  $\varepsilon_{x,y}^{\text{in}} = 1\pi \text{ mm} \cdot \text{mrad}$  (r.m.s.), see Fig. 25. The beam profile and beam cross section in the middle of the dispersion free straight section of the ring were reproduced, see Fig. 25, *a* and *b*. The r.m.s. widths of the beam are equal to  $\sigma_x^{\text{rms}} = 2.2 \text{ mm}$  in horizontal and  $\sigma_y^{\text{rms}} = 2.8 \text{ mm}$  in vertical planes (Fig. 25, *a*). Simulated beam spot before electron cooling corresponds to full beam dimensions  $12 \times 20 \text{ mm}$ , which is well agreed with experimentally measured beam size before electron cooling, see Fig. 24. Also image of  $\text{CF}^+$  injected beam in the  $x$ - $x'$  phase plane is shown in Fig. 25, *c*. The area occupied by  $\sim 95\%$  of presentation points corresponds to full emittance  $\varepsilon_{x,y}^{\text{in}} \approx 6\pi \text{ mm} \cdot \text{mrad}$ .

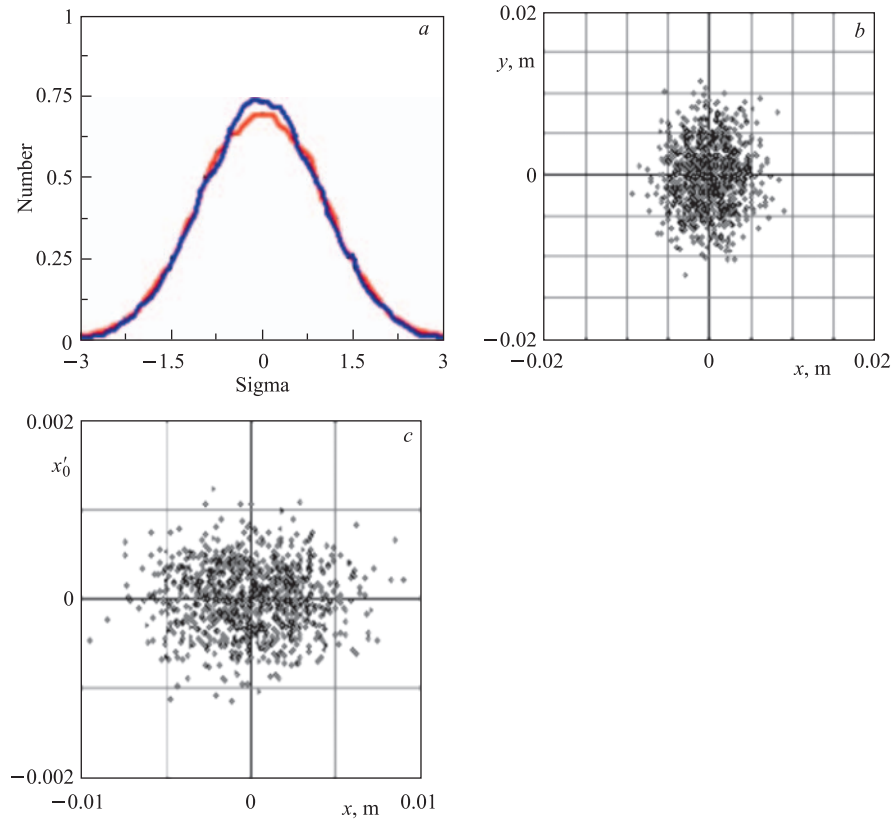


Fig. 25. Snap-shots of  $\text{CF}^+$  beam injected in the TSR ring. Initial beam emittance is  $\varepsilon_{x,y}^{\text{in}} = 1\pi \text{ mm} \cdot \text{mrad}$  (r.m.s.): *a*) simulated beam profile where  $\sigma_x^{\text{rms}} = 2.2 \text{ mm}$  and  $\sigma_y^{\text{rms}} = 2.8 \text{ mm}$ ; *b*) beam spot in the  $x$ - $y$  cross section corresponds to full beam dimensions  $12 \times 20 \text{ mm}$ , see Fig. 24; *c*) beam image in  $x$ - $x'$  phase space: area occupied by 95% of presentation points corresponds to emittance  $\varepsilon_{x,y}^{\text{in}} \approx 6\pi \text{ mm} \cdot \text{mrad}$

Combined effect of heating and cooling processes was reproduced by BETACOOOL, and r.m.s. parameters of the evolution of the ion distribution function have been derived. After few seconds of cooling time the beam emittance is reduced from initial  $\varepsilon_{x,y}^{\text{in}} = 1\pi \text{ mm} \cdot \text{mrad}$  (r.m.s.) to an equilibrium at  $\varepsilon_{x,y}^{\text{eq}} = 10^{-3}\pi \text{ mm} \cdot \text{mrad}$  (r.m.s.) (Fig. 26, *a*). Emittance of low intensity beam is collapsed in 1000 times. The estimated cooling time is  $\tau_{\text{cool}} \approx 0.4 \text{ s}$ .

The cooling by low energy spread electrons emitted by photocathode reduces transverse phase space of low intensity beam at least 10 times more efficient than cooling by conventional thermocathode. Momentum spread of ions cooled by photocathode is reduced in 10 times and equilibrium is reached at  $(\Delta P/P)_{\text{eq}} = 1.8 \cdot 10^{-5}$  (r.m.s.) (Fig. 26, *b*).

Equilibrium dimensions of cooled  $\text{CF}^+$  beam are presented in Fig. 27. The beam density profile is of a Gaussian shape (Fig. 27, *a*). Beam envelope might be approximated by ellipse with  $0.2 \times 0.25 \text{ mm}$  semi-axis (Fig. 27, *b*). Snap-shot of cooled beam in  $x - x'$  phase space is shown in Fig. 27, *c*, where  $x_{\text{max}} = 0.2 \text{ mm}$  and  $x'_{\text{max}} = 0.025 \text{ mrad}$ . Area in  $x-x'$  phase plane occupied by presentation points is equal to  $5 \cdot 10^{-3}\pi \text{ mm} \cdot \text{mrad}$ , see Fig. 27, *c*. For estimation purposes one may derive the standard deviations of beam in coordinate-angle variables as  $\sigma_x^{\text{rms}} = 0.07 \text{ mm}$  and  $\sigma_{x'}^{\text{rms}} = 0.009 \text{ mrad}$ . Thus, simulated value of equilibrium r.m.s. emittance equal to  $\varepsilon_{x,y}^{\text{eq}} = 6 \cdot 10^{-4}\pi \text{ mm} \cdot \text{mrad}$  is close to experimentally measured data.

The low intensity ( $N_0 = 2 \cdot 10^4$ ) beam of 97 keV/A  $\text{CF}^+$  ions with Gaussian distribution was tracked almost one million turns in the ring using the Model Beam algorithm in order to see the evolution of the distribution function. The equilibrium area in the  $(x, \Delta P/P)$  phase space occupied by beam after electron cooling is marked by well localized black spot in Fig. 28. Here the space charge parabola of electron beam (red) shows the energy distribution of the electron beam across the cooler cross section. The horizontal line (red) is a shift of e-beam energy with respect to mean energy of ion beam and tilted line (red) is related to the dispersion  $D = 2 \text{ m}$  in the straight section of the TSR ring where the photocathode electron target is installed. The red curve here represents evolution of r.m.s. beam emittance versus r.m.s. momentum spread.

The behaviour of  $\text{CF}^+$  beam in 3D phase space  $(\Delta P/P, \varepsilon_x)$  is shown in Fig. 29. The centre of gravity of model beam presentation points corresponds to the equilibrium emittance of  $\varepsilon_x^{\text{eq}} = 10^{-3}\pi \text{ mm} \cdot \text{mrad}$  and equilibrium momentum spread of  $(\Delta P/P)^{\text{eq}} = 5 \cdot 10^{-5}$ . So far, the agreement with experiment is good despite some differences in numbers which we would refer to the simplifications of the model, to the uncertainties of beam initial parameters as well as to the margins in estimations of longitudinal and transverse temperature of the photocathode electron target cooler.

We have checked the maximum allowable energy spread of the beam to be possibly cooled by the photocathode electron target. The modelling of electron

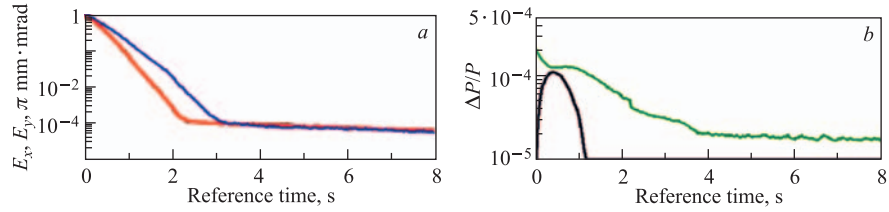


Fig. 26. Kinetics of 93 keV/A  $\text{CF}^+$  ions in the TSR ring: *a*) shrinking of beam emittance in  $\sim 1000$  times, from initial  $\varepsilon_{x,y}^{\text{eq}} = 1 \pi \text{ mm} \cdot \text{mrad}$  to approximately  $\varepsilon_{x,y}^{\text{eq}} = 6 \cdot 10^{-4} \pi \text{ mm} \cdot \text{mrad}$  after 8 s of cooling; *b*) decrease of momentum spread to an equilibrium at  $(\Delta P/P)_{\text{eq}} = 1.8 \cdot 10^{-5}$  (r.m.s.) after 8 s of cooling

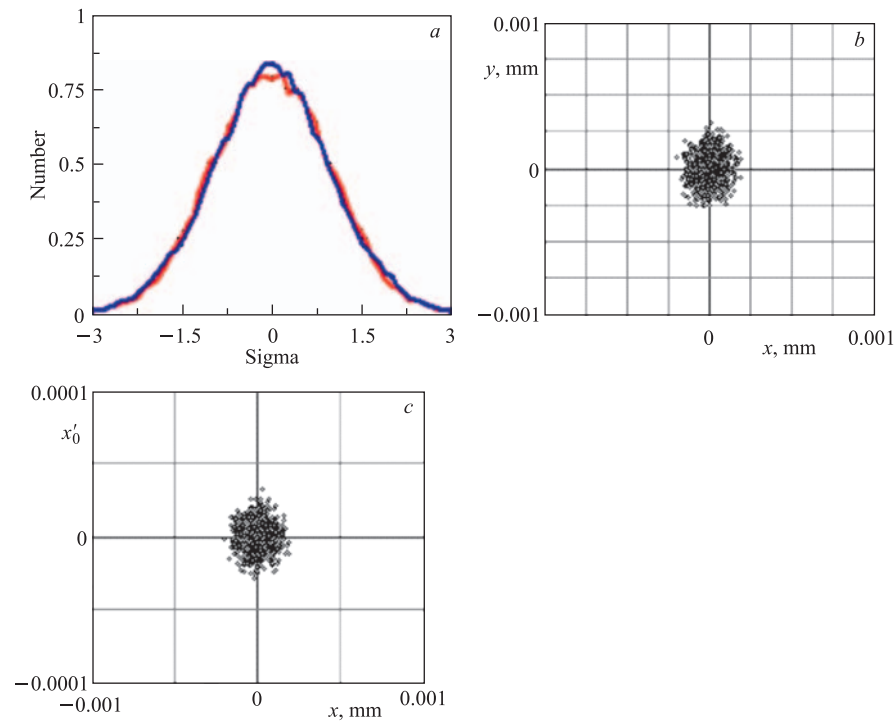


Fig. 27. Profiles of cooled  $\text{CF}^+$  beam in equilibrium simulated by BETACOOOL code: *a*) beam distribution of Gaussian shape where  $\sigma_x^{\text{rms}} = 0.06 \text{ mm}$  and  $\sigma_y^{\text{rms}} = 0.07 \text{ mm}$ ; *b*) beam spot might be approximated by envelope of elliptical shape with  $0.2 \times 0.25 \text{ mm}$  semi-axis; *c*) snap-shot of cooled beam in phase space where  $x_{\text{max}} = 0.2 \text{ mm}$  and  $x'_{\text{max}} = 0.02 \text{ mrad}$ . Area in  $x-x'$  phase plane occupied by presentation points (particle invariants) is equal to  $5 \cdot 10^{-3} \pi \text{ mm} \cdot \text{mrad}$ . This value corresponds to equilibrium r.m.s. beam emittance  $\varepsilon_{x,y}^{\text{eq}} = 6 \cdot 10^{-4} \pi \text{ mm} \cdot \text{mrad}$

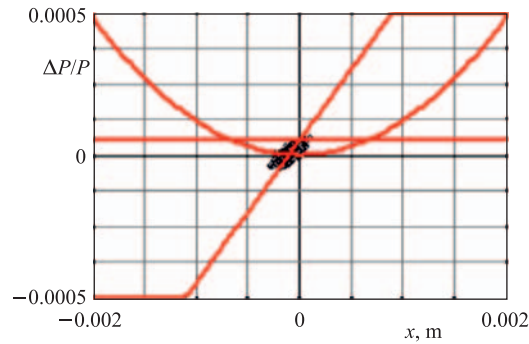


Fig. 28 (color online). The electron cooling of  $\text{CF}^+$  ions in the TSR ring by low temperature cryogenic photocathode. Equilibrium area in the  $(x, \Delta P/P)$  phase space occupied by beam after e-cooling is shown by well-localized black spot. Space charge parabola (red) represents energy distribution of electrons across cooler cross section, horizontal line is a shift of e-beam energy with respect to mean energy of ion beam and tilted line is related to the dispersion in the cooling section  $D = 2$  m

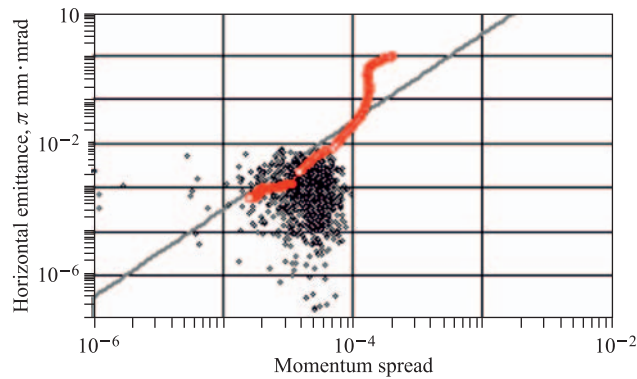


Fig. 29. Evolution of  $\text{CF}^+$  beam distribution in 3D phase space  $(\Delta P/P, \epsilon_x)$ . The centre of gravity of model beam presentation points corresponds to the equilibrium emittance of  $\epsilon_x^{\text{eq}} = 10^{-3} \pi \text{ mm} \cdot \text{mrad}$  and equilibrium momentum spread of  $(\Delta P/P)_{\text{eq}} = 5 \cdot 10^{-5}$

cooling of  $\text{CF}^+$  ions was performed for initial momentum spread  $(\Delta P/P)_{\text{in}} = 10^{-3}$  (r.m.s.) of low intensity 97 keV/A  $\text{CF}^+$  ions and it was shown that this beam should be efficiently cooled by photocathode electron gun.

Also we have checked performance of cooler assuming that standard thermoelectron gun is used for electron cooling. For the same beam and cooler parameters except that the transverse and longitudinal cathode temperatures are equal to  $kT_{\perp} = 4$  meV and  $kT_{\parallel} = 0.5$  meV, the friction force is much smaller and cooling rate is low. We simplified the problem and neglect recombination

of  $\text{CF}^+$  ions. The  $\text{CF}^+$  beam lifetime was artificially assigned to be  $4 \cdot 10^6$  s, i.e., infinitely long for our studies. On these conditions, the beam will be cooled by thermocathode to the equilibrium emittance of  $\varepsilon_{x,y}^{\text{eq}} = 6 \cdot 10^{-3} \pi \text{ mm} \cdot \text{mrad}$  (r.m.s.) and equilibrium r.m.s. momentum spread of  $(\Delta P/P)_{\text{eq}} = 7 \cdot 10^{-5}$ . Cooling time might exceed  $\tau_{\text{cool}} > 1.5$  s and total time to reach an equilibrium conditions is more than 8 s. Thus, cooling by thermocathode is much slower than by photocathode. Because the measured lifetime of  $\text{CF}^+$  ions is 4 s, the beam will be lost before to be cooled down by thermocathode to equilibrium conditions.

## 6. COMPENSATION OF IBS AND INTERNAL TARGET EFFECTS BY ELECTRON COOLING IN THE USR RING

The transition processes and equilibrium conditions of stored ions under combined action of electron cooling and multiple scattering of the beam on residual gas, IBS and scattering on internal gas jet target have been investigated by using BETACOOOL code. The feasibility studies of ion kinetics and long-term beam dynamics of ultralow energy ions were performed on example of the Ultra-Low Energy Storage Ring (USR) designed to operate with antiprotons as well as with negative and positive charged ions [38, 54, 72–74]. Low-energy antiprotons are the ideal and perhaps the only tool to study in detail correlated quantum dynamics of few-electron systems in the femto- and sub-femtosecond time regime [2]. In the future Facility for Low-Energy Antiproton and Ion Research (FLAIR) at FAIR-GSI (Darmstadt, Germany) the USR, which is comprised of electrostatic ion optics elements, operates in the variable energy range from  $300 \cdot q$  keV down to  $20 \cdot q$  keV and possibly to even lower energies [62, 72]. The USR will enable, for the first time, access to kinematically complete antiproton-induced rearrangement and fragmentation measurements [3].

**6.1. The USR Lattice.** The USR design, presently being elaborated by QUASAR group [54], was completely reconsidered since 2005 [61, 62]. In order to match different requirements from large variety of proposed experiments, few modes of operation are foreseen in the ring: deceleration and electron cooling at different energy levels, fast and slow extraction of beam for external experiments, «low- $\beta$ » mode for in-ring experiments with the internal gas jet, ultrashort bunches operation mode with achromatic lattice and optimization of the beam shape, size, and dispersion with respect to the respective internal or external experiment [73, 74]. Modified geometry of the USR ring is based on a fourfold symmetry split-achromat lattice which gives the necessary flexibility to satisfy multiple boundary conditions, see Fig. 30. The linear machine lattice was developed with the computer codes MAD-X and Trace3D [72].

Parameters of the ring lattice, electron cooling system, target and beam are listed in Table 4. The ring circumference is increased to 42.6 m in order to

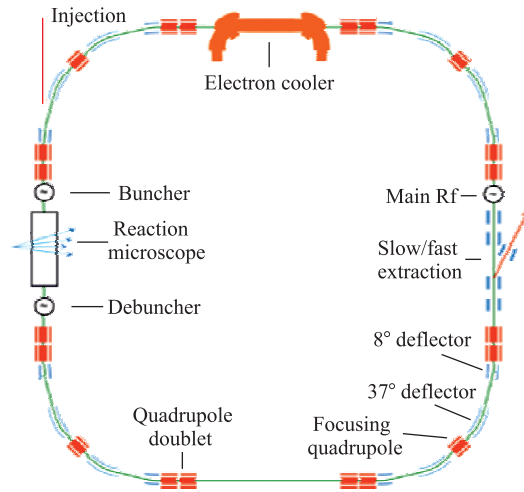


Fig. 30. Layout of the ultralow energy storage ring with split achromatic lattice. Shown are electron cooler, reaction microscope and elements of ultrashort bunch operation setup, electrostatic deflectors, quadrupoles and elements of extraction section

accommodate four 4 m long achromatic straight sections. The gas jet target and other components of the reaction microscope, the different rf systems for the short bunch operation mode [75, 76], the electron cooler, the decelerating drift tube and the elements for fast/slow extraction [77] are located in these straight sections. One of the straight sections is kept free for a possible inclusion of a merged positron ring [78, 79]. Five electrostatic quadrupoles, two  $8^\circ$  and two  $37^\circ$  electrostatic deflectors form split achromatic  $90^\circ$  bend. A drift space of 1 m between the  $8^\circ$  and  $37^\circ$  deflectors is left to allow for the counting of neutral particles during operation with charged ions. Neutrals leaving the ring straight section after the reaction microscope might be detected under an opening angle of up to  $\Omega = \pm 0.7^\circ$ .

The quads in the middle of each  $90^\circ$  bending section (Fig. 30) are used to modify the beam characteristics to achieve achromatic conditions, where both the dispersion function and its first derivative are zero in all four long straight sections  $D = D' = 0$ , as depicted in Fig. 31, *a*. By adjusting settings of main quadrupoles one can provide a «round beam» mode, see Fig. 31, *b*. Dispersion function in the straight sections can be smoothly varied in a wide range. The machine can be operated in various regimes in the tune diagram [54, 72, 74]. The four fold symmetry «round beam» and achromatic modes will be used for injection as well as during electron cooling, storage and deceleration. In addition, the USR lattice can also be set up for a slow extraction mode with betatron tune shift needed for exciting of third order resonance and controlled dispersion in straight

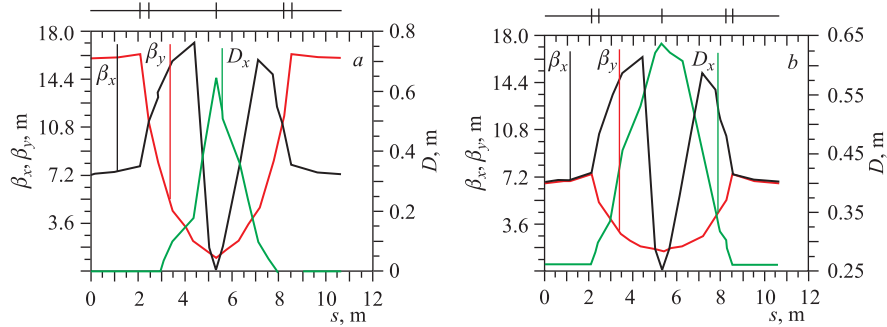


Fig. 31. Horizontal and vertical beta functions and dispersion of one ring quarter starting in the middle of long straight section: *a*) fourfold symmetry achromatic lattice; *b*) fourfold symmetry round beam mode. MAD-X simulations

sections [77]. The machine chromaticity is reasonably small when operating with fourfold symmetry lattice and negative tune shift does not exceed  $\Delta\nu = -0.009$  for particles with a momentum offset of up to  $\Delta P/P = 0.1\%$ .

For ring operation with reaction microscope where small beam size is required at target position we consider the «low- $\beta$ » lattice combined with achromatic conditions in straight sections [74, 80]. In this mode the ring lattice has a superperiodicity of two rather than four. An example of betatron and dispersion functions for one superperiod of the «low- $\beta$ » lattice is shown in Fig.32. Two low- $\beta$  inserts are located in the center of the experimental and opposite straight sections. Each focusing unit is comprised of two sets of electrostatic quadrupole triplets. These are located around target as close as possible to each other in order to provide a sharp focus in the middle of the straight section where the reaction

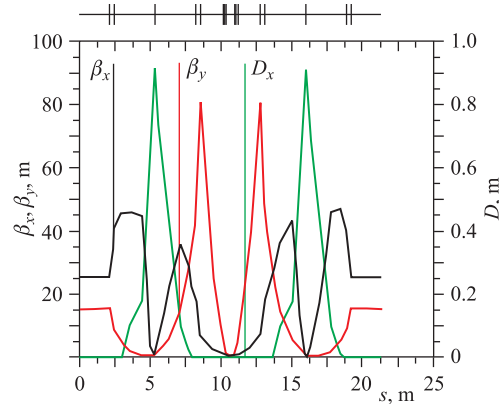


Fig. 32. An example of twofold symmetry achromatic lattice with low- $\beta$  functions at the ReMi location. One superperiod is shown. MAD-X simulations

microscope is located. In combination with asymmetric voltage applied to main quads on opposite sides of  $90^\circ$  bend one can vary beta functions in a wide range and reduce it to less than 0.5 m ( $\beta_{x,y}^{\text{targ}} < 0.5$  m) in the interaction region.

The side effect of proposed solution is a growth of maximum value of beta functions inside electrostatic quadrupoles. As a consequence, the acceptance of the USR ring estimated as  $A_{x,y} = 100 \pi$  mm · mrad will be limited during in-ring experiment with reaction microscope to  $A_{x,y} = 30 \pi$  mm · mrad, see Table 4. Also the ring chromaticity in the «low- $\beta$ » mode grows in few times with respect to the standard operation. The betatron tune shift due to high chromaticity might reach  $\Delta\nu_{x,z} = -0.024$  for particles with a momentum offset of  $\Delta P/P = 0.1\%$  and, therefore, sextupole corrections will be required. Another possible side effect of low- $\beta$  lattice is an increase of the intrabeam scattering heating rate in a few times up to the level which might essentially exceed the heating rate from the target itself.

Transition between 4-fold and 2-fold symmetry lattice modes require crossing of structure resonances and might be not feasible in real experiment. In this section, we will compare ring and cooler performance as well as beam parameters at different operation modes providing USR independently tuned to round beam lattice either to low- $\beta$  lattice.

**6.2. Electron Cooling of 300 keV Antiprotons.** The BETACOOOL code was used to find and optimize parameters of the USR lattice and electron cooling system for main modes of operation including cooling at 300 and 20 keV as well as operation with internal gas jet target at 20 keV. Parameters of antiproton beam are predefined by previous chain of accelerators as well as by efficiency of pbar production target [61]. The energy of antiprotons injected into the USR is fixed to 300 keV. It is anticipated that the emittance of injected beam will be about  $\varepsilon_{x,y}^{\text{in}} = 5 \pi$  mm · mrad (r.m.s.) and initial momentum spread — about  $(\Delta P/P)_{\text{in}} = 10^{-3}$  (r.m.s.). The intensity of ions circulating in the USR ring might be varied in a wide range between  $N_0 = 10^4$  and  $2 \cdot 10^7$  ions. The space charge limit on maximum allowed intensity of antiprotons is imposed by negative betatron tune shift of up to  $\Delta\nu \leq -0.1$  at the lowest beam energy of 20 keV [62].

We have checked cooler performance for different initial conditions — at high and low ion beam current, at different ring settings, etc. The ring, cooler and target parameters are listed in Table 4.

The operation mode with fourfold symmetry lattice is applied during injection, cooling and deceleration (Fig.31). In this operation mode the high intensity ( $N_0 = 2 \cdot 10^7$  ions) beam of 300 keV ions could be cooled down by thermoelectron gun to equilibrium conditions corresponding to the emittance value of  $\varepsilon_{x,y}^{\text{eq}} = 0.055\pi$  mm · mrad (r.m.s.) and momentum spread of  $(\Delta P/P)_{\text{eq}} = 2.5 \cdot 10^{-4}$  (r.m.s.), see Fig. 33, where the evolution of the r.m.s. emittance is shown in Fig. 33, *a* and evolution of r.m.s. momentum spread is presented in Fig. 33, *b*. From BETACOOOL simulations one may come to the con-

clusion that at 300 keV the high intensity beam of antiprotons might be cooled down to equilibrium conditions approximately in one second.

Equilibrium distribution of 300 keV antiprotons after electron cooling in 3D phase space coordinates  $(\Delta P/P, \varepsilon_x)$  is presented in Fig. 34, *a* by scattered points

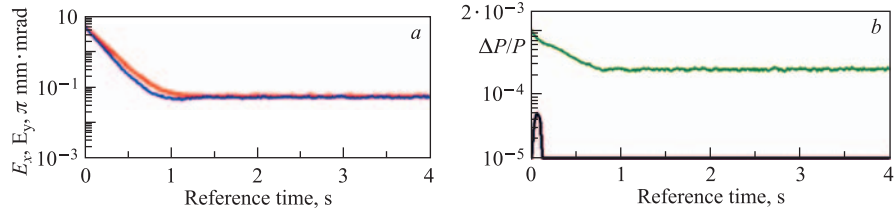


Fig. 33. Evolution of the r.m.s. emittance (*a*) and r.m.s. momentum spread (*b*) of 300 keV antiprotons during electron cooling in the USSR ring. High intensity ( $N_0 = 2 \cdot 10^7$  ions) beam with initial emittance  $\varepsilon_x^{\text{in}} = 5 \pi \text{ mm} \cdot \text{mrad}$  (r.m.s.) and initial momentum spread  $(\Delta P/P)^{\text{in}} = 10^{-3}$  (r.m.s.) is cooled down to equilibrium at  $\varepsilon_x^{\text{eq}} = 0.055 \pi \text{ mm} \cdot \text{mrad}$  (r.m.s.) and  $(\Delta P/P)^{\text{eq}} = 2.5 \cdot 10^{-4}$  in  $\sim 1$  s

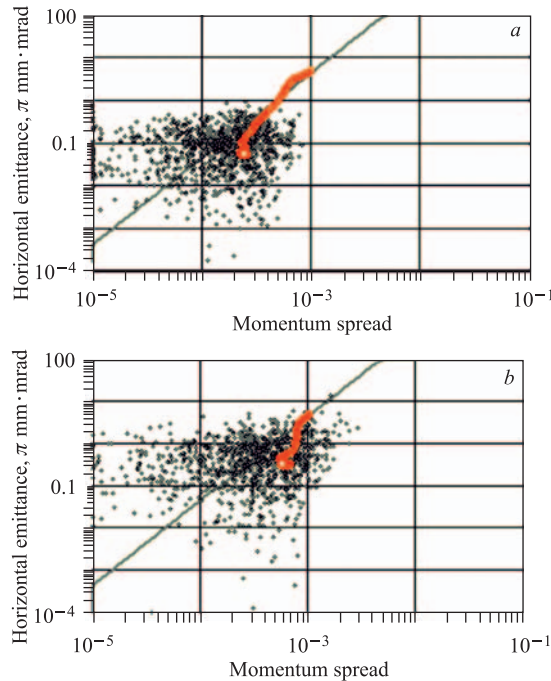


Fig. 34 (color online). Equilibrium distribution of 300 keV (*a*) and 20 keV (*b*) antiprotons in 3D phase space  $(\Delta P/P, \varepsilon_x)$  after electron cooling. Scattered points were simulated in the frame of the model beam algorithm [25]. Evolution of r.m.s. parameters during electron cooling is shown by red curve for 300 keV (*a*) and 20 keV (*b*) antiprotons

simulated in the frame of model beam algorithm [25]. Evolution of r.m.s. parameters during electron cooling by thermocathode gun is shown by red curve in this figure. The effect of intrabeam scattering for 300 keV ions is relatively small at beam intensity of  $N_0 = 2 \cdot 10^7$  ions, and r.m.s. kinetic parameters are almost in equilibrium at each step of cooling process, as shown in 3D phase space diagram of Fig. 34, *a*. Here the evolution curve of 300 keV antiprotons is overlapped almost everywhere with tilted line presenting equilibrium between cooling and heating processes.

### 6.3. Merit of the Photocathode Gun for the USR Electron Cooling System.

Second, we compare cooling rates and equilibrium conditions of the USR beam cooled down by electron gun with thermocathode and those cooled down by gun with cryogenic photocathode. Fourfold symmetry ring lattice used in standard operation mode was chosen for these studies (Fig. 31, *a*). The main limitation of electron cooler with photocathode gun is small extracted current, as was described in the previous section of this paper related to beam shrinking in the TSR ring.

At low voltages applied to the cathode of any type the electron current becomes limited by gun perveance  $P$  to about 1–2 mA at 100 V [64]. Practical limit of the electron beam current might be estimated from the expression

$$I_{\text{cath}} \leq PU^{3/2} = (1 - 2 \text{ mA}) \left( \frac{U}{100} \right)^{3/2}, \quad (56)$$

where voltage  $U$  applied to the cathode is measured in volts. The maximum current of electrons available from the cathode at energy level of  $W_e = 162$  eV is  $I_e = 2-4$  mA and it is  $I_e = 40-80$   $\mu\text{A}$  at  $W_e = 11$  eV. These energy levels of electron beam correspond to the ion energies of 300 keV and 20 keV, respectively.

We estimate that optimum value of electron current to cool down the 300 keV antiprotons is  $I_e = 1$  mA, i.e., well below the limit imposed by e-gun perveance. The 1 mA current of electron beam is exactly the working parameter of existing atomically clean  $p^+$ -GaAs photocathode with a thin layer of cesium and oxygen [64]. The optimum current of electron beam to cool down 20 keV ions is 50  $\mu\text{A}$ . Regardless of the cathode type, the best performance of electron gun is required at the lowest energies in order to reach optimum parameters.

The temperature of cryogenically cooled photocathode is  $kT_{\text{cath}} = 7-10$  meV which is at least 10 times less than the thermocathode temperature  $kT_{\text{cath}} = 100$  meV. The energy spread of electron beam in transverse direction is defined by cathode temperature and it is reduced by adiabatic expansion of guiding magnetic field between gun and electron cooler solenoid to

$$kT_{\perp} = \frac{kT_{\text{cath}}}{\alpha}, \quad (57)$$

where expansion factor  $\alpha$  may vary from 10 to 20 times. In our studies, the transverse electron temperature of thermo- and photocathode is  $kT_{\perp} = 4$  meV and  $kT_{\perp} = 0.5$  meV, respectively.

The longitudinal electron temperature depends on kinematic factor and density term of electrons

$$kT_{\parallel} = C_1 \frac{(kT_{\text{cath}})^2}{W_e} + C_2 \frac{e^2 n_e^{1/3}}{4\pi\epsilon_0}, \quad (58)$$

where factor  $C_1$  varies between 1 and 2 and takes into account that the part of the transverse electron energy is transferred to the longitudinal degree of freedom during adiabatic expansion of magnetic field. The density term is related to the relaxation energy of accelerated electron beam [81], and «constant»  $C_2$  is not a fixed value in the ultralow energy range when kinematic term dominates but rather should be varied between approximately 1 and 2 [64].

The kinematic term dominates for the thermocathode in the ultralow energy range because of the high temperature of cathode and low intensity of electron beam. The longitudinal temperature of the thermocathode is  $kT_{\parallel} = 0.5$  meV in our studies [38]. The longitudinal temperature of the ultralow energy electron gun with photocathode is a trade-off between kinematic factor and density term. We estimate it should slightly grow from  $kT_{\parallel} = 30$   $\mu\text{eV}$  for electron beam of  $W_e = 11$  eV energy to  $kT_{\parallel} = 50$  eV for  $W_e = 162$  eV electrons because of the increased current of electrons and growth of density term in formula (58). In the ultralow energy range the energy spread of electron gun with photocathode is approximately 10 times smaller with respect to the energy spread of the thermocathode.

The evolution of r.m.s. emittance of high intensity beam of antiprotons ( $N_0 = 2 \cdot 10^7$  ions) cooled down at 300 and 20 keV is shown in Fig. 35. Antiprotons cooled down at 20 keV are marked with labels 1 for thermocathode gun and label 2 for photocathode gun. Antiprotons cooled down by thermo- either by photocathode at injection energy 300 keV are marked with labels 3 and 4, respectively.

In the considered energy range between 300 and 20 keV, for low ( $N_0 = 10^4$  ions) and high ( $2 \cdot 10^7$  ions) beam intensities, the cooling rates and equilibrium parameters of beam cooled by the photocathode are much better than those available with the thermocathode. At injection energy of 300 keV antiprotons should be cooled down by e-cooler with photocathode to equilibrium emittance  $\epsilon_x^{\text{eq}} = 0.04\pi$  mm·mrad (r.m.s.) while cooler with thermocathode — to equilibrium at  $\epsilon_x^{\text{eq}} = 0.055\pi$  mm·mrad (r.m.s.). At 20 keV energy the equilibrium emittance of beam cooled by photocathode is  $\epsilon_x^{\text{eq}} = 0.35\pi$  mm·mrad which is two times less than the emittance of the beam cooled by thermocathode to equilibrium at  $\epsilon_x^{\text{eq}} = 0.73\pi$  mm·mrad. The negative betatron tune shift due to space charge of high intensity beam ( $N_0 = 10^7$  ions) of 20 keV antiprotons should not be more than  $\Delta\nu_{x,y} \leq -0.06$ .

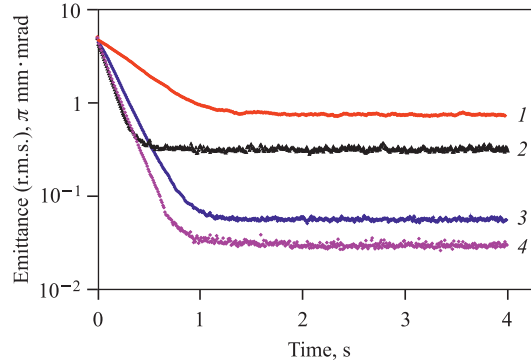


Fig. 35. Ion kinetics of high-intensity antiproton beam ( $N_0 = 2 \cdot 10^7$ ): *a*) evolution of 20 keV antiprotons cooled down by thermocathode e-gun to equilibrium emittance  $\varepsilon_x^{\text{eq}} = 0.73 \pi \text{ mm} \cdot \text{mrad}$  (r.m.s.) (1) and cooled down by photocathode to equilibrium at  $\varepsilon_x^{\text{eq}} = 0.35 \pi \text{ mm} \cdot \text{mrad}$  (r.m.s.) (2). Ions at 300 keV cooled down by thermocathode to equilibrium emittance  $\varepsilon_x^{\text{eq}} = 0.055 \pi \text{ mm} \cdot \text{mrad}$  (r.m.s.) (3) and cooled down by photocathode to equilibrium at  $\varepsilon_x^{\text{eq}} = 0.04 \pi \text{ mm} \cdot \text{mrad}$  (r.m.s.) (4)

The equilibrium momentum spread of the 20 keV beam cooled by photocathode is  $(\Delta P/P)^{\text{eq}} = 6.5 \cdot 10^{-4}$  (r.m.s.) while it is  $(\Delta P/P)^{\text{eq}} = 9.8 \cdot 10^{-4}$  (r.m.s.) in case of cooling by thermocathode.

Scattered points in Fig. 34, *b* simulated in the frame of Model Beam algorithm present the equilibrium distribution of 20 keV antiprotons in 3D phase space  $(\Delta P/P, \varepsilon_x)$  after cooling by electron gun with photocathode. Evolution of r.m.s. parameters during electron cooling by photocathode gun is shown by red curve in this figure. The effect of intrabeam scattering for 20 keV ions is strong at beam intensity of  $N_0 = 2 \cdot 10^7$  ions and ion kinetic parameters are shifted from tilted line presenting equilibrium between cooling and heating processes.

Comparison of equilibrium distribution of 20 keV antiprotons in the  $(x, \Delta P/P)$  phase space after electron cooling by photo- and thermocathode is presented in Fig. 36. Black spot comprises scattered points and represents ions distribution in phase space. The beam occupies compact area in  $(x, \Delta P/P)$  phase space after e-cooling by low temperature cryogenic photocathode (Fig. 36, *a*). The smashed area with solid beam core is a result of electron cooling by thermocathode gun (Fig. 36, *b*).

Because of better performance, we choose parameters of the photocathode e-gun for further consideration. Also we take into account that the technical realization of simulated electron cooler with photocathode is possible and might be done in experiment.

In the Hamiltonian consideration of the ion motion some specific effects like multiple scattering, IBS, space charge are not taken into account, and reducing of

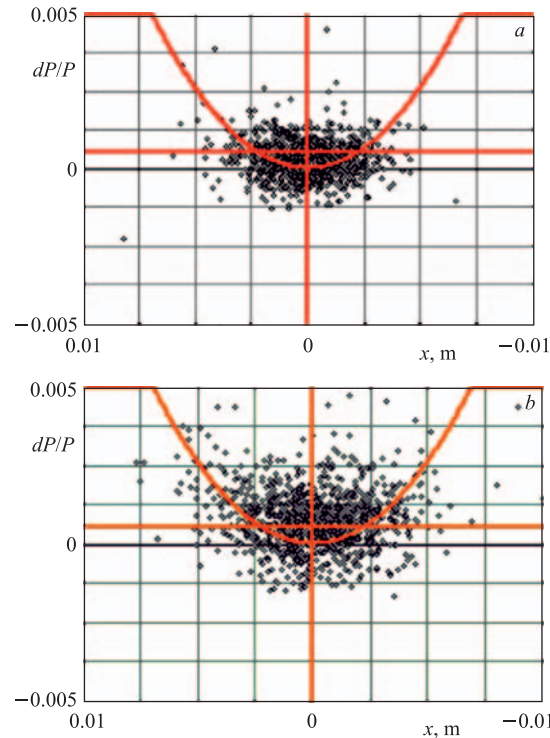


Fig. 36 (color online). Equilibrium distribution of 20 keV high-intensity antiprotons ( $N = 2 \cdot 10^7$  particles). Black spot composed of scattered points represents the beam in the  $(x, \Delta P/P)$  phase space. Space charge parabola (red) of electron beam is shown, horizontal line (red) is a shift of e-beam energy with respect to mean energy of ion beam: *a*) compact area presents particle distribution in phase space occupied by beam cooled down by low temperature cryogenic photocathode; *b*) smeared area with solid core is a result of electron cooling by thermocathode gun

ion energy leads to the adiabatic growth of area occupied by beam in coordinate-angle  $(x, x')$  phase space variables. The emittance is inversely proportional to the ion velocity  $1/\beta$ . One might expect that the beam emittance should adiabatically grow from equilibrium value  $\epsilon_x^{\text{eq}} = 0.04 \pi \text{ mm} \cdot \text{mrad}$  (r.m.s.) at 300 keV to equilibrium value  $\epsilon_x^{\text{eq}} \approx 0.16 \pi \text{ mm} \cdot \text{mrad}$  (r.m.s.) at the lowest beam energy, i.e., at 20 keV.

The BETACOOOL simulation at 20 keV provides different value of equilibrium emittance  $\epsilon_x^{\text{eq}} = 0.35 \pi \text{ mm} \cdot \text{mrad}$  (r.m.s.), see curve 2 in Fig. 35. In these studies we do not take into account any beam mismatching during RF capture or rebunching, during deceleration, etc. Thus, one may assume that the in-

creased rate of intrabeam scattering at the lowest energy is a reason of excessive value of equilibrium emittance  $\epsilon_x^{\text{eq}} = 0.35 \pi$  with respect to equilibrium emittance  $\epsilon_x^{\text{eq}} \approx 0.16 \pi \text{ mm} \cdot \text{mrad}$  (r.m.s.) anticipated at 20 keV due to only adiabatic growth of beam motion invariant.

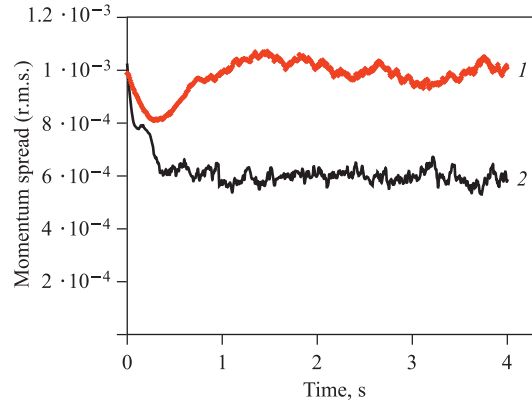


Fig. 37. Evolution of momentum spread (r.m.s.) of high intensity beam of 20 keV antiprotons cooled down by electron gun with thermocathode (1) and with photocathode (2). Equilibrium momentum spread is  $(\Delta P/P)_{\text{rms}}^{\text{eq}} = 10^{-3}$  and  $(\Delta P/P)_{\text{rms}}^{\text{eq}} = 6 \cdot 10^{-4}$ , respectively

Evolution of momentum spread (r.m.s.) of high intensity beam ( $N_0 = 2 \cdot 10^7$  ions) of 20 keV antiprotons cooled down to equilibrium is presented in Fig. 37. Cooling by electron gun with thermocathode would lead to equilibrium momentum spread of  $(\Delta P/P)_{\text{rms}}^{\text{eq}} = 10^{-3}$  while during cooling by photocathode e-gun the equilibrium is reached at  $(\Delta P/P)_{\text{rms}}^{\text{eq}} = 6 \cdot 10^{-4}$ .

**6.4. Optimization of Lattice Parameters in the Cooler Section.** Influence of different ring settings on the electron cooling performance was studied. We compare how features of ring lattice might affect ion kinetics as well as beam parameters at equilibrium. Namely, we investigate how the values of horizontal and vertical betatron functions in straight section, where the cooler is located, as well as betatron functions in the middle of straight section, where the target is located, will affect the r.m.s. emittance and r.m.s. momentum spread of the beam. We split the task and consider the ring operation at different conditions: in standard fourfold symmetry mode and compare to low- $\beta$  twofold symmetry mode, with low intensity beam ( $N = 2 \cdot 10^4$  ions) and compare to operation with high intensity beam ( $N = 2 \cdot 10^7$  ions).

In main operation mode of the ring when the internal gas jet target is switched off, the fourfold symmetry lattice is applied (Fig. 31) and contribution of the intrabeam scattering to the growth of beam size is mainly determined by high

density beam spots in the middle of each split achromat cell, see Fig. 30. Sharp beam focus is formed inside of the central electrostatic lens which is used for the dispersion tuning, and horizontal betatron function is reduced here to the value of  $\beta_x \sim 5$  cm, see Fig. 31, *a, b*.

In fourfold symmetry operation mode, the electron cooler suppresses multiple scattering of ions on residual gas and IBS for any reasonable large betatron functions in long straight sections of ring lattice. Nevertheless, even at low beam intensities ( $N = 2 \cdot 10^4$  ions) large value of betatron function in the cooler section would lead to the cooling of ions to equilibrium conditions ranging from  $\varepsilon_{x,y}^{\text{eq}} = 0.03 \pi \text{ mm} \cdot \text{mrad}$  (r.m.s.) for  $\beta_{x,y} = 2$  m up to  $\varepsilon_{x,y}^{\text{eq}} = 0.33 \pi \text{ mm} \cdot \text{mrad}$  (r.m.s.) for  $\beta_{x,y} = 25$  m. Thus, amplitude of betatron functions in the cooler section less than  $\beta_{x,y} < 10$  m is preferable.

At 20 keV energy and high beam intensities ( $N = 2 \cdot 10^7$  ions) the intrabeam scattering dominates and influence of lattice parameters is more pronouncing. If the ring is tuned to large values of betatron functions in the cooler section, namely to  $\beta_{x,y} = 25$  m, the diameter of injected beam with initial emittance of  $\varepsilon_x^{\text{in}} = 5 \pi \text{ mm} \cdot \text{mrad}$  (r.m.s.) will be about 50 mm while electron beam diameter is 20 mm, see Table 4. Even at these conditions, the photogun electron cooler will reduce beam size slightly and ions will be cooled down to an equilibrium at  $\varepsilon_{x,y}^{\text{eq}} \approx 2 \pi \text{ mm} \cdot \text{mrad}$  (r.m.s.). This value is approximately 6 times more than one should expect from the electron cooling at optimum configuration of the ring lattice in straight sections, see curve 2 in Fig. 35. The r.m.s. momentum spread might even grow from initial  $(\Delta P/P)_{x,y}^{\text{in}} = 10^{-3}$  after injection to equilibrium at  $(\Delta P/P)_{x,y}^{\text{eq}} \approx 1.5 \cdot 10^{-3}$  if lattice parameters are not optimized in cooler section and betatron functions amplitude exceeds 20–25 m. The process of beam cooling is much slower at these conditions. From 3 to 5 s might be required to bring beam to equilibrium if the ring is tuned to excessively large betatron functions in the cooler section. Extended cooling time over few seconds is not acceptable in USR experiments within FLAIR facility because the short operation cycle between subsequent pulses of 300 keV antiprotons is foreseen in the previous chain of decelerating storage rings [61, 62].

The efficiency of electron cooling might be estimated by relative change of particle angular divergence as a result of cooler action on ion motion  $\Delta\theta_{\text{cool}}/\sigma'_{x,y}$ , where  $\Delta\theta_{\text{cool}}$  is a transverse angle variation due to electron friction force defined by expression (52) and  $\sigma'_{x,y}$  is a standard angular deviation of ions in the cooler section of the ring. Thus, smooth and relatively large betatron functions are required in the cooler section in order to minimize standard angular deviation  $\sigma'_{x,y} = \sqrt{\varepsilon_{\text{rms}}^{\text{in}}/\beta_{x,y}^{\text{cool}}}$  and produce maximum cooling effect. Nevertheless, excessively large amplitude of betatron oscillations in the cooler section of the USR ring harms cooler performance. We expect that the negative effect of excessively large betatron functions on cooling performance is a result of low efficiency of

electron cooling when transverse dimensions of injected ion beam are few times larger than diameter of electron beam and ions are not overlapped by electrons.

The radius of electron beam in the guiding solenoid  $r_e = 10$  mm is a practical limit of ultralow energy e-cooler with photocathode gun and we choose this value in our studies. Regardless of initial beam intensity, the maximum cooling rate and best cooler performance could be realized if the ion beam will be overlapped by electrons completely. It is reasonable to assume — at least in approximation of be-Gaussian distribution of ions both in position and angle — that the radius of equivalent ion beam is equal to two standard deviations  $r_{\text{beam}} = 2\sigma_{x,y}^{\text{in}}$ . Almost 86.5% of total beam intensity are included into the phase space area equal to  $4\varepsilon_{\text{rms}}^{\text{in}}$ . The condition of ion beam being overlapped by electrons might be satisfied if, according to the expression

$$\beta_{\text{cool}} \approx \frac{r_e^2}{4\varepsilon_{\text{rms}}^{\text{in}}}, \quad (59)$$

the beta functions in cooling section of the USR ring are flat and  $\beta_{x,y} \approx 5$  m. The «round beam» lattice was used in our MAD-X simulations where horizontal and vertical betatron functions in straight sections are equal both to  $\beta_{x,y} = 7$  m. We choose these values as an optimum for the electron cooling section, see Fig. 31, *b*.

**6.5. Requirements to the Target Section of the Ring.** In the presence of internal gas jet, the increment of emittance growth per one target traversal is proportional to the value of the betatron function in the target location as well as to the dispersion and derivative of dispersion at this position, see formula (23). The growth of emittance during target crossing will be minimized if ring is tuned to achromatic conditions  $D = D' = 0$  and value of betatron function  $\beta_{x,y}^{\text{targ}}$  is low in this point. In other words, suppression of multiple scattering of ions on atoms and molecule of supersonic gas jet by electron cooling is more efficient if beam is sharply focused on the target. Thus, one should provide as small as possible betatron functions in the middle of ring straight section where target is located. The reasonable solution in our particular case would be tune lattice to the low- $\beta$  mode, see Fig. 32. In contrary to smooth lattice in the ring section for electron cooling, the strongly focused beam crosses target in the reaction microscope section at large angles of betatron oscillations (up to  $\theta_\beta = 20$  mrad). As a consequence, the standard r.m.s. angular deviation  $\sigma'_{\text{targ}}$  is large at this particular location, and relative increment of scattering angle per one target traversal  $\delta\theta_{\text{sc}}/\sigma'_{\text{targ}}$  estimated by the expression

$$\frac{\delta\theta_{\text{sc}}}{\sigma'_{\text{targ}}} = \frac{\sqrt{\theta_{\text{sc}}^2}}{\sqrt{\varepsilon_{\text{rms}}^{\text{eq}}/\beta_{x,y}^{\text{targ}}}} \quad (60)$$

is less than in case of flat but large beta functions.

Also there is strong requirement of experiment with reaction microscope to keep beam size at target to about the diameter of gas jet. Thus, full beam width should be approximately equal to 1 mm in the middle of target section of the ring. Like in case with electron cooler, we apply criteria of 4 r.m.s. equilibrium emittance in order to estimate lattice parameters at target location. It was assumed that transverse dimensions of equivalent beam in equilibrium should not exceed the target diameter. To satisfy these conditions and collect maximum integral of ionization events one may estimate margins to the betatron functions at target location using the following expression

$$\beta_{x,y}^{\text{targ}} \leq \frac{\sigma_{\text{targ}}^2}{\varepsilon_{\text{rms}}^{\text{eq}}}. \quad (61)$$

Dependence of equilibrium beam emittance on beam intensity at different operation modes of the ring is shown in Fig. 38, *a*. The curve 1 in this figure summarizes results of BETACOOOL simulations for standard operation mode with «round beam» lattice. The trend-line marked as 2 in this figure is a fit by power series  $\varepsilon_{\text{rms}}^{\text{eq}} = 3 \cdot 10^{-4} \cdot N^{0.42}$  which is close to predicted ratio  $\varepsilon_{\text{rms}}^{\text{eq}} \sim N^{0.6}$  described in [77]. Equilibrium emittance of the beam when target is switched ON and ring lattice is tuned to low- $\beta$  mode will be in 3 to 5 times higher than corresponding value in the main operation mode, see curve 3 in Fig. 38, *a*.

The equilibrium momentum spread versus beam intensity is shown in Fig. 38, *b* where results of BETACOOOL simulations for standard ring operation with «round beam» lattice are marked by label 1 and trend-line fit by power series  $(\Delta P/P)_{\text{rms}}^{\text{eq}} = 7 \cdot 10^{-6} \cdot N^{0.26}$  is marked by label 2. The fit is close to predicted ratio  $(\Delta P/P)_{\text{rms}}^{\text{eq}} \sim N^{0.3}$  [82]. Equilibrium momentum spread of the beam when

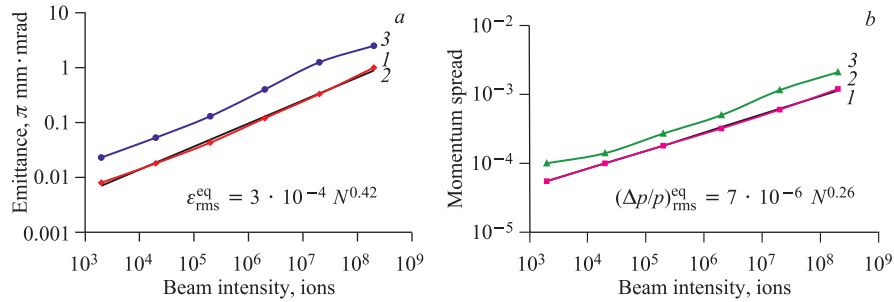


Fig. 38. Dependence of equilibrium beam parameters on injected beam current: *a*) equilibrium emittance at different beam intensities: 1 — standard ring operation with «round beam» lattice; 2 — trend-line fit by power series  $\varepsilon_{\text{rms}}^{\text{eq}} = 3 \cdot 10^{-4} N^{0.42}$ ; 3 — low- $\beta$  mode operation with internal target; *b*) equilibrium momentum spread at different beam intensities: 1 — standard ring operation with «round beam» lattice; 2 — trend-line fit by power series  $(\Delta P/P)_{\text{rms}}^{\text{eq}} = 7 \cdot 10^{-6} N^{0.26}$ ; 3 — low- $\beta$  mode operation with internal target [82]

target is switched ON and ring lattice is tuned to low- $\beta$  mode will be at least by 50 to 100% larger than corresponding value in the main operation mode, see curve 3 in Fig. 38, *b*.

In our studies we do not simulate crystalline beam by applying special option in the BETACOOOL code but mostly were interested how electron cooling, residual gas, IBS and internal gas jet target in combination with different ring parameters may affect beam behaviour. The r.m.s. dynamics and model beam algorithm were used to study transition processes and equilibrium conditions in a wide range of initial beam intensities ranging from  $N_0 = 2 \cdot 10^3$  ions and up to  $N_0 = 2 \cdot 10^8$  ions.

When ring is tuned to 2-fold symmetry lattice with sharp focus in the middle of target section the low intensity beam ( $N_0 = 2 \cdot 10^4$  ions) might be cooled down to equilibrium emittance of  $\varepsilon_{x,y}^{\text{eq}} \approx 0.06 \pi \text{ mm} \cdot \text{mrad}$  (r.m.s.). Thus, at low ion intensities requirement to the minimum value of betatron functions at target location  $\beta_{x,y}^{\text{targ}} \leq 100 \text{ cm}$  estimated by expression (61) is relaxing.

If beam intensity is high ( $N_0 = 2 \cdot 10^7$  ions) and ring is tuned to low- $\beta$  mode, the equilibrium between friction (cooling) and heating processes is reached at much higher level of beam emittance  $\varepsilon_{x,y}^{\text{eq}} \approx 1.2 \pi \text{ mm} \cdot \text{mrad}$  (r.m.s.), see curve 3 in Fig. 38, *a*. One should compare this number with the equilibrium parameters of the USSR ring in standard operation mode (curve 2 in Fig. 35).

Because of large value of equilibrium beam parameters at high beam intensities, the requirements to the low- $\beta$  ring lattice are very strict and betatron functions should be reduced in the middle of straight section where the reaction microscope is located to  $\beta_{x,y}^{\text{targ}} \leq 10 \text{ cm}$  in order to satisfy experiment conditions and keep beam size at gas jet target as small as possible, see Fig. 32.

Providing the ring is tuned to low- $\beta$  mode and minimum values of betatron functions in the middle of straight section where the reaction microscope is located are equal to  $\beta_{x,y} = 10 \text{ cm}$ , the high intensity beam ( $N = 2 \cdot 10^7$  ions) of 20 keV antiprotons might be focused at target to the spot of  $\approx 1.2 \text{ mm}$  diameter, see Fig. 39, *a*. The equilibrium r.m.s. width of high-intensity beam is  $\sigma_{\text{eq}} = 0.3 \text{ mm}$  at this location. Also the beam image in  $x-x'$  phase space is shown in Fig. 39, *b*. One may estimate that about 86% of all representation points might be covered by phase space ellipse with area of  $A_{x,y}^{\text{eq}} \approx 5 \pi \text{ mm} \cdot \text{mrad}$ , which corresponds to the equilibrium r.m.s. emittance of  $\varepsilon_{x,y}^{\text{eq}} \approx 1.2 \pi \text{ mm} \cdot \text{mrad}$ .

Finally, we distinguish effects of the intrabeam scattering from the multiple scattering of ions on the gas jet target and simulate long term beam dynamics and ion kinetics at different lattice parameters in the reaction microscope section. For that, the values of the horizontal and vertical betatron functions were varied from 5 to 80 cm at the target location as well as in the symmetry point of the ring, and corresponding changes were made to the MAD-X output file which is used as input lattice parameters for the BETACOOOL code. Variation of betatron functions only in few points of the ring lattice is an artificial measure and might not be realized in experiment because the parameters of ring lattice will vary everywhere. But

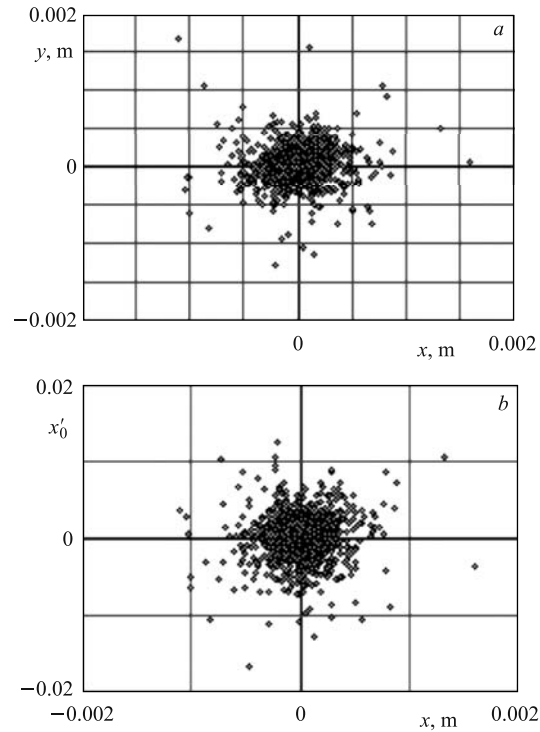


Fig. 39. Snap-shots of cooled 20 keV beam at target location. Beam intensity is  $N = 2 \cdot 10^7$  ions. Ring is tuned to low- $\beta$  mode where  $\beta_{x,y} = 10$  cm in the middle of straight section with reaction microscope: *a*)  $x - y$  cross section, equilibrium r.m.s. width is  $\sigma_{\text{eq}} = 0.3$  mm, beam spot of 1.2 mm diameter includes 86.5% of beam intensity; *b*) beam image in  $x - x'$  phase space corresponds to equilibrium emittance of  $\varepsilon_{\text{rms}}^{\text{eq}} \approx 1.2 \pi$  mm · mrad (r.m.s.)

this method provides important information on processes involved into ultralow energy rings operation.

Dependence of the equilibrium emittance (r.m.s.) of 20 keV cooled beam on the value of the ring betatron functions in the target focal plane is shown in Fig.40. Smaller beam size means higher ion current density for the same intensity of the beam. The IBS growth rate is proportional to the ion current density which is reduced when beam size at target is increased. In contrary to IBS, the growth rate due to multiple scattering on target is increased for large values of betatron functions, see formula (23).

The effect of emittance grows in proportion to the increase of betatron function at target is visible but only at very low beam intensities of  $N = 2 \cdot 10^3$  ions.

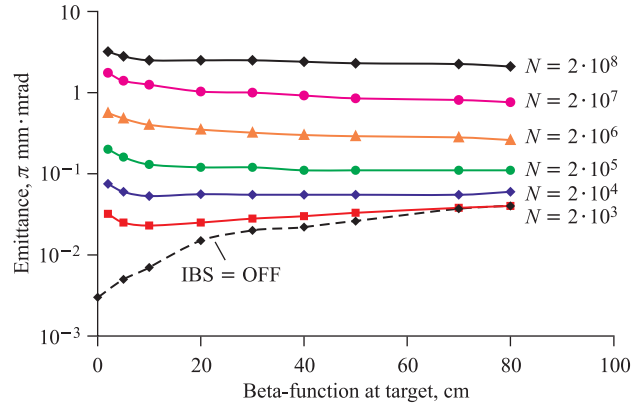


Fig. 40 (color online). Dependence of the equilibrium emittance (r.m.s.) of 20 keV antiprotons on value of the ring betatron function at target location. The r.m.s. emittance of high intensity beam ( $N = 2 \cdot 10^7$  ions) mostly defined by the IBS growth rate. The IBS growth rate is proportional to the ion current density which is reduced when beam size at target is increased. At very low beam intensity ( $N = 2 \cdot 10^3$  ions), the IBS contribution to the beam size growth is less especially for large betatron functions and beam size depends more on multiple scattering of ions on the target. Dashed curve represents equilibrium when IBS is artificially switched OFF in the BETACOOOL code

The helium gas jet target of  $n_{\text{targ}} = 5 \cdot 10^{11} \text{ cm}^{-3}$  density would be the main source of growth of equilibrium beam parameters but only if other processes like multiple scattering on residual gas and IBS will be less than multiple scattering on target. We exclude effect of the IBS and come to an agreement with theory described in Subsubsec.2.2.1 of this paper. Dashed curve in Fig.40 represents equilibrium conditions when IBS is artificially switched OFF in the BETACOOOL code. Two last points of red curve representing emittance growth of very low intensity beam and black dashed curve representing emittance growth in absence of IBS coincide in Fig.40. At very low beam intensities ( $N \approx 2 \cdot 10^3$  ions) the IBS contribution to the beam size growth is less especially for large values of betatron functions and beam size depends more on multiple scattering of ions on the target. Even at ultralow beam intensities, the growth rate of intrabeam scattering surpasses scattering on target if beam is focused and value of betatron function is less than  $\beta_{x,y} \leq 30 \text{ cm}$ .

Meanwhile, experiments with low current ions are of weak interest and circulation of high intensity beams and multiple crossing of ions with internal gas jet target is a main condition for future atomic physics experiments in the USR ring. At beam intensities over  $N \geq 2 \cdot 10^4$  ions, the rate of intrabeam scattering is much higher than those of multiple scattering on gas jet. Effect of strong growth of the IBS contribution is clearly seen in Fig.40 when betatron functions

are reduced to less than  $\beta_{x,y} \leq 10$  cm and local ion density at target position is high. Thus, attempts to decrease beam size of high intensity ions by reducing of betatron functions to ultralow beta values might lead to essential growth of equilibrium beam parameters.

We came to the conclusion that the intrabeam scattering at ultralow energies is a leading source of emittance growth and multiple scattering of ions on the target should not harm the experiment performance except for very low beam intensities. Only the reason to provide sharp focus at target position is a request to reduce beam size to a diameter of gas jet.

Besides, in-ring experiments with internal gas jet target, the best operation conditions and the highest beam intensity in the USR ring might be realized if the so-called smooth ring lattice will be applied and IBS rate will be reduced significantly.

### 6.6. Ionization Events and Adiabatic Dump of Equilibrium Parameters.

As was shown in the previous chapters of this paper, the electron cooling of ultralow energy antiprotons will compensate intrabeam scattering at high beam intensities up to  $N = 2 \cdot 10^8$  ions as well as multiple scattering of ions on internal target at high gas jet densities up to  $n_{\text{targ}} = 10^{12} \text{ cm}^{-3}$ . Also in the considered energy range between 20 and 300 keV, the maximum relative transferable energy during impact between incident antiprotons and electrons of helium atom will not exceed  $\delta E/E = 2 \cdot 10^{-3}$  of ion kinetic energy. Thus, the absolute value of energy lost in one ionization event should not exceed the longitudinal acceptance of the USR ring which is about  $\pm 2\%$  in energy spread.

Like in case of the BETACOOOL simulations for the recycler ring, we do not have reliable experimental data on the ratio between ionization and excitation cross sections during interactions of incident antiprotons with He atoms. Due to the lack of experimental data at the ultralow energy range we assumed that each ionization event should lead to the loss of an incident ion despite of relatively small energy drop. During operation with internal gas jet target the particle number in the USR will be reduced even though the electron cooling will compensate the beam lateral spread and energy loss together with energy straggling. In order to estimate number of ionization events, we have used experimental value of ionization cross section of He atoms by 20 keV antiprotons  $\sigma_{\text{He}} = 5 \cdot 10^{-17} \text{ cm}^2$ , see Fig. 22 taken from [59].

Results of simulations of beam intensity decay and integral of ionization events during multiple interaction of 20 keV antiprotons with helium atoms in the USR ring are shown in Fig. 41. Density of He gas jet target is  $n_{\text{targ}} = 5 \cdot 10^{11} \text{ cm}^{-3}$ , see Table 4. Under assumption, that ions are lost after each ionization event, the integral of the ionization events (red curve in Fig. 41) cannot exceed initial beam intensity. The black curve in this figure presents decay of particle number in time. The luminosity of experiment is  $L = 2 \cdot 10^{22} \text{ cm}^{-2} \cdot \text{s}^{-1}$  for gas jet target of 1 mm diameter and should be at least two times more for the

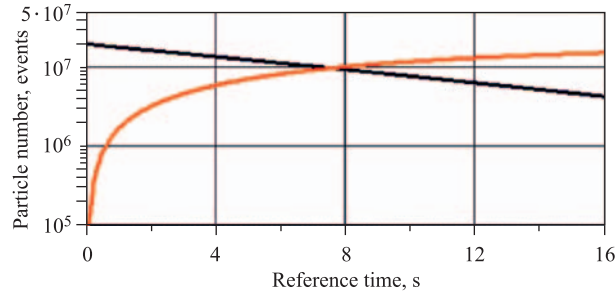


Fig. 41 (color online). Simulations of beam intensity decay (black) and integral of ionization events (red) in the USR ring during multiple interaction of 20 keV antiprotons with helium atoms. Density of He gas jet target is  $n_{\text{targ}} = 5 \cdot 10^{11} \text{ cm}^{-3}$ . It is assumed that ions are lost after each ionization event. Luminosity of experiment is  $L = 2 \cdot 10^{22} \text{ cm}^{-2} \cdot \text{s}^{-1}$  and cross section of reaction is  $\sigma_{\text{ion}} = 5 \cdot 10^{-17} \text{ cm}^2$ . Integral of useful events is  $1 \cdot 10^7$  after 8 s, beam lifetime is  $\tau_{\text{life}} = 12 \text{ s}$ . Count rate is  $\sim 20$  events per one turn

«curtain» jet (gas cell) of the same effective thickness. The luminosity will be adiabatically decreased in proportion with reduced particle number.

The integral of useful events might be as high as  $1.5 \cdot 10^7$  counts after 16 s of USR operation with gas jet target. Average count rate in proposed scenario is about  $\sim 20$  events per one ion revolution in the ring. We estimate that the beam lifetime at 20 keV should be about  $\tau_{\text{life}} \approx 12 \text{ s}$  and hope that direct measurements of beam lifetime and intensity decay in such an experiment will help to prove either reject assumptions made in our computing studies.

Because the beam intensity is slowly reduced during ionization events, the intrabeam scattering growth rate is going down. Long term adiabatic evolution of beam parameters associated with beam «burning» on the target is shown in Fig.42. The equilibrium beam emittance is adiabatically decreased in time from  $\varepsilon_{x,y}^{\text{eq}} = 0.32 \pi \text{ mm} \cdot \text{mrad}$  (r.m.s.) for  $N = 2 \cdot 10^7$  ions down to  $\varepsilon_{x,y}^{\text{eq}} =$

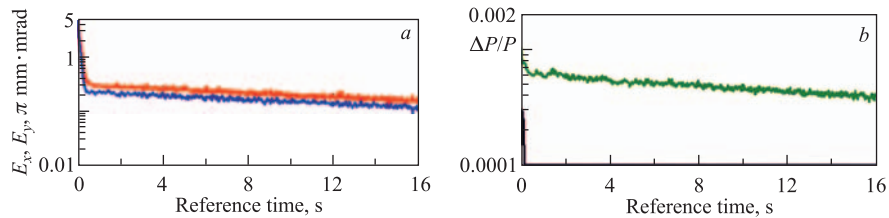


Fig. 42. Long term adiabatic evolution of beam parameters associated with beam «burning» on the target: *a*) equilibrium beam emittance (r.m.s.) and *b*) equilibrium beam momentum spread (r.m.s.) are slightly decreased in time because the beam intensity is adiabatically reduced during ionization events and rate of intrabeam scattering is going down

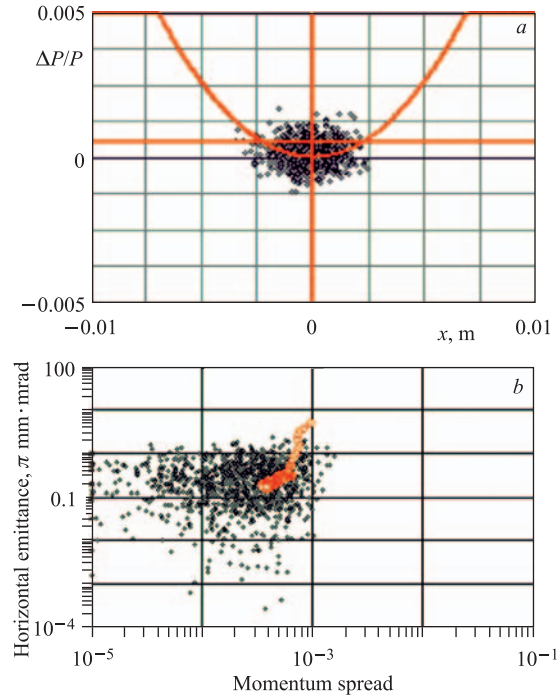


Fig. 43. Equilibrium beam distribution of 20 keV antiprotons after 16 s of cooling process and beam «burning» on the target: *a*) black spot composed of scattered points in the  $(x, \Delta P/P)$  phase space is more compact with respect to the cooled beam at the beginning of operation cycle, see. Fig. 36, *a*; *b*) distribution of ions in 3D phase space  $(\Delta P/P, \varepsilon_x)$  after 16 s, ions with relatively high momentum spread and emittance are cooled down because of the reduced IBS growth rate at decreased beam intensity (to be compared with Fig. 34, *b*)

$0.16 \pi \text{ mm} \cdot \text{mrad}$  (r.m.s.) for  $N = 4 \cdot 10^6$  ions (Fig. 42, *a*). Same, the equilibrium beam momentum spread is adiabatically decreased from  $(\Delta P/P)_{\text{rms}}^{\text{eq}} = 6 \cdot 10^{-4}$  (r.m.s.) for  $N = 2 \cdot 10^7$  ions down to  $(\Delta P/P)_{\text{rms}}^{\text{eq}} = 4 \cdot 10^{-4}$  (r.m.s.) for  $N = 4 \cdot 10^6$  ions (Fig. 42, *b*).

Distribution of cooled beam in phase space after beam «burning» on the target is presented in Fig. 43. Black spot shown in Fig. 43, *a* is composed of scattered points in the  $(x, \Delta P/P)$  phase space. After adiabatic reducing of beam intensity, the distribution is more compact with respect to the equilibrium beam distribution at the beginning of operation cycle, see Fig. 36, *a*. Distribution of ions in 3D phase space  $(\Delta P/P, \varepsilon_x)$  after 16 s of beam «burning» and reducing of ion current in five times with respect to the initial beam is presented in Fig. 43, *b*.

Scattered representation points with large emittance or momentum spread are absent towards the end of cycle. We assume that ions with relatively large momentum spread and emittance are cooled down because the IBS growth rate is reduced (to be compared with Fig. 34, *b*).

## 7. SUMMARY AND OUTLOOK

The beam behaviour in an ultralow energy storage rings is described. Nonlinear and long term beam dynamics and ion kinetics have been studied on example of ELISA, Recycler, TSR and USR rings. Consistent explanation of beam growth and associated ion losses based on benchmarking of ELISA experiments is proposed. Beam size in this ring is increased due to multiple scattering of ions on atoms and molecules of residual gas as well as due to intrabeam scattering at high beam intensities. The main reasons of ion losses at ultralow beam energies reduced ring acceptance of nonlinear nature and high growth rate of beam parameters.

In addition, the requirements and conditions of ring operation with internal gas jet target are formulated. Achromatic lattice and low- $\beta$  mode of operation should be applied in collision experiments with internal target in order to provide sufficient count rate of ionization events, high precision measurements, and reasonable lifetime. Operation with dense gas jet target is possible even at  $\sim$  keV energy range but in expense of increased rate of intrabeam scattering and reduced lifetime due to formation of high-density beam spot at target location. One may control beam size on target in low- $\beta$  mode of operation and reduce it to  $\sim$  2 mm. Providing the initial intensity of injected beam is about  $10^7$  antiprotons, one should be able to measure slightly more than one count of ionization events per one revolution in the recycler ring operating at the lowest energy of 3 keV and up to 7 events — at energy of 30 keV.

In addition, beam shrinking in the TSR experiment on electron cooling of low energy  $\text{CF}^+$  ions was reproduced with a good accuracy. Merit of photocathode gun for cooling down of ultralow ions is justified on example of the TSR and USR rings. Optimisations to the USR lattice parameters improving ring performance are formulated. We showed that in the low- $\beta$  operation mode the increase of intrabeam scattering growth rate is a main effect shifting equilibrium parameters of 20 keV antiproton beam to higher values. Even at the worst conditions, the equilibrium r.m.s. emittance of high intensity beam ( $N = 2 \cdot 10^7$  ions) should not exceed  $\varepsilon_{x,y}^{\text{eq}} = 1 \pi \text{ mm} \cdot \text{mrad}$  and the beam spot of 1.2 mm diameter could be formed at target location.

Almost 20 ionization events per one revolution might be available in the USR ring during multiple crossing of high intensity beam of antiprotons with He gas jet target of  $n_{\text{targ}} = 5 \cdot 10^{11} \text{ cm}^{-3}$  density of atoms.

Besides in-ring experiments with internal gas jet target, the best operation conditions and highest beam intensity in the USR ring might be realized if the so-called smooth ring lattice will be applied and IBS rate will be reduced significantly.

Future beam dynamics studies will investigate further into the effects of space charge on the stored beam, and, in particular, into the evolution of the beam under consideration of the effects from electron cooling and an in-ring gas jet target. In addition, a 3-dimensional study of the short pulse operation mode will be carried out with an objective to build up full model of ion behaviour during ultrashort bunch operation mode.

**Acknowledgements.** The generous support of the European Commission under contract PITN-GA-2008-215080, the Helmholtz Association of National Research Centers (HGF) under contract number VH-NG-328, and the GSI Helmholtz Center for Heavy Ion Research (GSI) is acknowledged.

#### REFERENCES

1. *Zajfman D. et al.* Physics with Electrostatic Rings and Traps // *J. Phys. B: At. Mol. Opt. Phys.* 2004. V. 37. P. 57–88.
2. *Ulrich J., Welsch C.* Exploring Subfemtosecond Correlated Dynamics with an Ultralow Energy Electrostatic Storage Ring // *Proc. of LEAP-2005*. Jülich, Germany, 2005. 6 p.
3. *Welsch C. P. et al.* Exploring Subfemtosecond Correlated Dynamics with an Ultralow Energy Electrostatic Storage Ring // *AIP Conf. Proc.* 2005. V. 796. P. 266–271.
4. *Moller S. P.* ELISA — an Electrostatic Storage Ring for Atomic Physics // *Nucl. Instr. Meth.* 1997. V. 394, No. 3. P. 281–286.
5. *Tanabe T. et al.* An Electrostatic Storage Ring for Atomic and Molecular Science // *Nucl. Instr. Meth. A.* 2002. V. 482. P. 595.
6. *Jinno S. et al.* TMU Electrostatic Ion Storage Ring Designed for Operation at Liquid Nitrogen Temperature // *Nucl. Instr. Meth. A.* 2004. V. 532. P. 477.
7. *Rensfelt K.-G. et al.* DESIREE — a Double Electrostatic Storage Ring // *Proc. of EPAC*. Lucerne, Switzerland, 2004. P. 1425–1427.
8. *Stiebing K. E. et al.* FLSR — The Frankfurt Low Energy Storage Ring // *Nucl. Instr. Meth. A.* 2010. V. 614, No. 1. P. 10–16.
9. *Zajfman D. et al.* Physics with Colder Molecular Ions: The Heidelberg Cryogenic Storage Ring CSR // *J. Phys. Conf. Ser.* 2005. V. 4. P. 296.
10. *El Ghazaly M. A. et al.* Layout of a Novel Electrostatic Storage Ring at KACST // *Appl. Math. Inform. Sci.* 2009. V. 3, No. 3. P. 309–319.
11. *Senichev Yu., Moller S. P.* Beam Dynamics in Electrostatic Rings // *Proc. of EPAC-2000*. P. 794–796.

12. *Senichev Yu.* The Features of Beam Dynamics in the Electrostatic Storage Rings. FZJ IKP Report. Juelich, 2000. 20 p.
13. *Moller S.* Design and First Operation of the Electrostatic Storage Ring, ELISA // Proc. of Eur. Part. Accel. Conf. «EPAC-1998». Stockholm, 1998. P. 73–77.
14. *Moller S.P.* Operational Experience with the Electrostatic Storage Ring, ELISA // Proc. of PAC-1999. P. 2295–2297.
15. *Moller S.P. et al.* Intensity Limitations of the Electrostatic Storage Ring ELISA // Proc. of EPAC-2000. Vienna, Austria. P. 788–790.
16. <http://cosyinfinity.org>
17. *Mane S.R.* Orbital Dynamics in a Storage Ring with Electrostatic Bending // Nucl. Instr. Meth. A. 2008. V. 596. P. 288–294.
18. *Hinterberger F.* Ion Optics with Electrostatic Lenses // CERN School on Small Accelerators. 2005. 24 p.
19. OPERA-3D (TOSC/SCALA). Computer code.
20. TRACE-3D. Computer code.
21. <http://mad.web.cern.ch/mad>
22. *Papash A.I., Welsch C.P.* Simulations of Space Charge Effects in Low Energy Electrostatic Storage Rings // Proc. of IPAC-2010, Kyoto, Japan, 2010. P. 1952–1954.
23. *Gorda A., Papash A.* Nonlinear Fields of Cylindrical and Spherical Deflector and Their Effect on Beam Dynamics in the ELISA Ring. QUASAR Group Design Note. 2010. 5 p.
24. *Sidorin A. et al.* BETACOOOL Program for Simulation of Beam Dynamics in Storage Rings // Nucl. Instr. Meth. A. 2006. V. 558, No. 1. P. 325–328.
25. BETACOOOL Physics Guide. <http://betacool.jinr.ru>.
26. *Ben-Zvi I. et al.* Electron Cooling of RHIC // Proc. of PAC-2005, Knoxville, USA, 2005. P. 2741–2743.
27. *Fedotov A.V. et al.* Cooling Dynamics Studies and Scenarios for the RHIC Cooler // Ibid. P. 4236–4238.
28. *Fedotov A.V. et al.* Experimental Studies of the Magnetized Friction Force // Phys. Rev. E. 2006. V. 73, No. 6.
29. *Katayama T. et al.* MD Simulation of Beam Ordering // Nucl. Instr. Meth. A. 2004. V. 532. P. 371–375.
30. *Meshkov I. et al.* Numerical Simulation of Crystalline Ion Beams in Storage Ring // Ibid. P. 376–381.
31. *Dietrich J. et al.* Studies of Beam Dynamics in Cooler Rings // Proc. of COOL-2005, FNAL, Galena, USA, 2005. P. 154–158; Proc. of AIP Conf. 2005. V. 821.
32. *Dietrich J. et al.* Electron Cooling of Intense Ion Beam // Proc. of COOL-2005, FNAL, Galena, USA, 2005. P. 270–279; Proc. of AIP Conf. 2005. V. 821.

33. *Dolinskii A. et al.* Simulation Results on Cooling Times and Equilibrium Parameters for Antiproton Beams at the HESR // Proc. of EPAC-2004, Lucerne, Switzerland, 2004. P. 1972–1974.
34. *Smirnov A. V. et al.* Particle Accumulation with a Barrier Bucket RF System // Proc. of COOL-2009, IMP, Lanzhou, China, 2009. P. 67–70.
35. *Galnander B. et al.* Cooling Force Measurements at CELSIUS // Proc. of COOL-2005, FNAL, Galena, USA, 2005. P. 259–264; Proc. of AIP Conf. 2005. V. 821.
36. *Noda A. et al.* Crystalline Beam Simulations // Proc. of EPAC-2008, Genoa, Italy, 2008. P. 1747–1749.
37. *Papash A., Smirnov A., Welsch C.* Long Term Beam Dynamics in Ultralow Energy Storage Rings // Proc. of IPAC-2011, San-Sebastian, Spain, 2011. P. 2166–2168.
38. *Smirnov A. V., Papash A. I., Welsch C. P.* BETACOOOL Simulations of Ion Kinetics in the Ultralow Energy Electrostatic Storage Ring (USR) // Proc. of COOL-2011, Alushta, Ukraine, 2011. 3 p.
39. *Risken H.* The Fokker–Planck Equation. Methods of Solution and Applications. Springer Ser. Ed., 1996. 472 p.
40. *Avilov V.* Calculation of Electrostatic Energy of Planar Lattices // Solid State Commun. 1982. V. 44, No. 4. P. 555–558.
41. *Hinterberger F., Prasuhn D.* Analysis of Internal Target Effects in Light Ion Storage Rings // Nucl. Instr. Meth. A. 1989. V. 279. P. 413–422.
42. *Rutherford E.* The Scattering of  $\alpha$  and  $\beta$  Particles by Matter and the Structure of the Atom // Phil. Mag. 1911. V. 6. P. 21.
43. *Moliere G.* // Z. Naturforsch. 1947. V. 2a. P. 133.
44. *Thomas L. H.* The Calculation of Atomic Fields // Proc. of Cambridge Phil. Soc. 1927. V. 23, No. 5. P. 542–548.
45. *Fano U.* // Phys. Rev. 1954. V. 93. P. 117.
46. *Moliere G.* // Z. Naturforsch. 1948. V. 3a. P. 78.
47. *Fano U.* // Ann. Rev. Nucl. Sci. 1963. V. 13. P. 1.
48. *Bethe H. A.* // Phys. Rev. 1953. V. 89. P. 1256.
49. *Piwinski A.* // Proc. of the 9th Intern. Conf. on High Energy Accelerators. 1974. P. 105.
50. *Martini M.* Intrabeam Scattering in the ACOOL-AA Machines. CERN PS/84-9 AA. Geneva, 1984.
51. *Bjorken J. D., Mtingwa S. K.* Intrabeam Scattering // Part. Accel. 1983. V. 13. P. 115.
52. *Jie Wei.* Evolution of Hadron Beams under Intrabeam Scattering // Proc. of PAC-1993. P. 3651.
53. *Piwinski A.* // Proc. of the 9th Intern. Conf. on High Energy Accelerators. 1974. P. 105.
54. *Papash A., Welsch C. P.* An Update of the USR Lattice: Towards a True Multiuser Experimental Facility // Proc. of PAC-2009, Vancouver, BC, Canada, 2009. P. 4335–4337.

55. *Siggel-King M. et al.* Electrostatic Ultralow-Energy Antiproton Recycling Ring // *Hyp. Int.* 2011. V. 199, No. 1. P. 311–319.
56. *Ullrich J. et al.* Kinematically Complete Experiments Using Cold Target Recoil Ion Momentum Spectroscopy // *Nucl. Instr. Meth. B.* 1997. V. 124, Nos. 2–3. P. 225–231.
57. *Welsch C., Papash A. et al.* Design of an Antiproton Recycler Ring // *Proc. of PAC-2011, New York, USA, 2011.* P. 1879–1881.
58. *Siggel-King M. et al.* Design of a Low-Energy Ion-Beam Facility // *Proc. of IPAC-2011, San-Sebastian, Spain, 2011.* P. 2019–2021.
59. *Knudsen H.* Private communication. 2009.
60. *Wolf A. et al.* // *Proc. of COOL-2005, 2005.* P. 473–477.
61. *Welsch C.P. et al.* FLAIR – A Facility for Low-Energy Antiproton and Ion Research at GSI // *Hyp. Int.* 2007. V. 172, Nos. 1–3. P. 71–80.
62. *Welsch C.P. et al.* An Ultralow-Energy Storage Ring at FLAIR // *Nucl. Instr. Meth. A.* 2005. V. 546. P. 405–417.
63. *Jaeschke E. et al.* The Heidelberg Test Storage Ring for Heavy Ions TSR // *Proc. of EPAC-1988, Rome, Italy, 1988.* P. 365–367.
64. *Orlov D.A. et al.* Electron Cooling with Photocathode Electron Beams Applied to Slow Ions at TSR and CSR // *Proc. of COOL-2007, Bad Kreuznach, Germany, 2007.* P. 230–233.
65. *Orlov D.A. et al.* // *J. Phys.: Conf. Ser.* 2005. V. 4. P. 290.
66. *Orlov D.A. et al.* // *Appl. Phys. Lett.* 2001. V. 78. P. 272.
67. *Budker G.* // *Proc. of Intern. Symp. on Electron and Positron Storage Rings. Saclay, France, 1966.*
68. *Meshkov I.* Electron Cooling: Status and Perspectives // *Phys. Part. Nucl.* 1994. V. 25, No. 6. P. 631.
69. *Parkhomchuk V.* New Insights in the Theory of Electron Cooling // *Nucl. Instr. Meth. A.* 2000. V. 441. P. 9–17.
70. *Bisoffi G. et al.* The Heidelberg Heavy Ion Cooler Storage Ring TSR // *Proc. of PAC-1989.* P. 49–53.
71. *Steck M. et al.* The Electron Cooling Device for the Heavy Ion Storage Ring TSR // *Proc. of EPAC-1988.* P. 1172–1174.
72. *Papash A., Welsch C.P.* An Update of the USR Lattice: Towards a True Multiuser Experimental Facility // *Proc. of PAC-2009, Vancouver, BC, Canada, 2009.* P. 4335–4337.
73. *Welsch C.P. et al.* Present Status of the USR Project // *Hyp. Int. Proc. of LEAP-2008, Vienne, 2009.* P. 1–7.
74. *Welsch C.P. et al.* Ultralow-Energy Storage Ring at FLAIR // *Hyp. Int.* DOI: 10.1007/s10751-011-0460-z. 2011. 11 p.

75. *Papash A. I., Welsch C. P.* On the Possibility of Realizing Shortest Bunches in Low-Energy Storage Rings // *Phys. Part. Nucl. Lett.* 2009. V. 6, No. 3. P. 216–226.
76. *Papash A. I., Welsch C. P.* Realization of Nanosecond Antiproton Pulses in the Ultralow-Energy Storage Ring // *Nucl. Instr. Meth. A.* 2010. V. 620, Nos. 2–3. P. 128–141.
77. *Karamisheva G. A., Papash A. I., Welsch C. P.* Study of Slow and Fast Extraction for the Ultralow-Energy Storage Ring (USR) // *Phys. Part. Nucl. Lett.* 2011. V. 8, No. 1. P. 50–60.
78. <http://www.oeaw.ac.at/smi/flair/LOI.html>
79. *Meshkov I. et al.* Status of the LEPTA Project // *Proc. of RuPAC-2008, Zvenigorod, Russia, 2008.*
80. *Gorda A., Papash A.* Lattice Considerations for the USR and the AD-REC Electrostatic Storage Rings. QUASAR Group Design Note. 2011. 10 p.
81. *Meshkov I. et al.* Ultimate Possibilities of Electron Cooling. Preprint 88-61. *Inst. of Nucl. Phys. Novosibirsk, 1988.*
82. *Shirai T. et al.* One-Dimensional Beam Ordering of Protons in a Storage Ring // *Phys. Rev. Lett.* 2007. V. 98, No. 20. P. 204801.